High pressure study of the electronic structure of self-assembled InAs/GaAs and InP/GaP quantum dots

vorgelegt von
Diplom-Physiker
Christian Kristukat
aus Berlin

von der Fakultät II - Mathematik und Naturwissenschaften
der Technischen Universität Berlin
zur Erlangung des akademischen Grades

Doktor der Naturwissenschaften – Dr. rer. nat. –

genehmigte Dissertation.

Promotionsausschuss:

Vorsitzender: Prof. Dr. rer. nat. T. Möller
Berichter: Prof. Dr. rer. nat. C. Thomsen
Berichter: Priv. Doz. A. R. Goñi

Tag der wissenschaftlichen Aussprache: 10. Februar 2006

Berlin 2006
D 83

Hiermit versichere ich an Eides statt, dass ich die vorliegende Dissertation selbständig verfasst habe.

Berlin, 12. 2. 2006

Zusammenfassung

Gegenstand der vorliegenden Arbeit ist die Untersuchung der optischen Eigenschaften von selbstorganisierten InAs/GaAs und InP/GaP Quantenpunkten unter externem, hydrostatischem Druck. Zu diesem Zweck wurden druckabhängige Photolumineszenzexperimente mittels einer Diamantstempel-Zelle durchgeführt.

Die Emission der hier untersuchten InAs/GaAs Probe weist eine multimodale spektrale Verteilung auf. Dies ist auf die Existenz von Quantenpunktsubensembles zurückzuführen, deren mittlere Größe sich um vollständige Monolagen InAs unterscheidet. Neun einzelne Emissionspeaks können, basierend auf strukturellen Untersuchungen, der Emission von Quantenpunktensembles mit ein bis neun Monolagen Höhe zugeordnet werden. Die Druckkoeffizienten der Emissionspeaks liegen im Bereich von 65 für die kleinsten, bis 110 meV/GPa für die größten Quantenpunkte. Berechnungen der Druckabhängigkeit des Verzerrungsfeldes von Quantenpunkten mittels einer atomistischen Methode ergeben, dass der Druckkoeffizient der InAs Bandkante stark reduziert wird, wenn InAs in GaAs eingebettet ist. Unter Berücksichtigung von *confinement* Effekten im Rahmen der *envelope function approximation* ergeben sich theoretische Druckkoeffizienten in guter qualitativer Übereinstimmung mit dem Experiment. Weitere Details der Bandstruktur werden gewonnen aus der Analyse der Energien, bei denen die gebundenen Elektronenzustände die X-Punkt Zustände in der Barriere kreuzen, was von einer starken Abnahme der Emissionsintensität begleitet wird. Auf diese Weise kann die Energie der Löcher der verschieden großen Quantenpunkte bestimmt und durch Anpassung an gerechnete *confinement*-Energien ein Valenzbandoffset von 290 ± 10 meV ermittelt werden.

Im InP/GaP Materialsystem konnte erst kürzlich selbstorganisiertes Quantenpunktwachstum realisiert werden. Bedingt durch die große Gitterfehlanpassung der beiden Materialien verschiebt die hohe, interne Verzerrung die Γ-Punkt Bandlücke in die Nähe der indirekten Bandlücke von GaP. Ungeklärt blieb bislang die Frage, ob die Emission bei 1.92 eV direkt im reziproken und realen Raum erfolgt. Mittels der Druckexperimente konnte in dieser Arbeit aber der direkte Charakter der Rekombination nachgewiesen werden. Bei Umgebungsdruck liegt die Γ-Punkt Leitungsbandzustandsenergie in den Quantenpunkten nur 10 meV unterhalb der des X-Punkt Zustandes von InP. Begleitet von einer Blauverschiebung der Emission erfolgt daher schon bei einem geringen Druck von etwa 0.2 GPa ein Γ–X crossover, welches sich in einer abrupten Abnahme der Lumineszenzintensität niederschlägt. Bei weiterer Erhöhung des Drucks sinkt die Emissionsenergie leicht ab, wie es typischerweise für eine indirekte X–Γ Rekombination zu erwarten ist, und bei einem Druck von 1.2 GPa kreuzt der X-Zustand in den Quantenpunkten den des *wetting layer*, wodurch die Lumineszenz zum Erliegen kommt. Die Emission aus den gebundenen Quantenpunktzuständen weist maximale Intensität bei einer Temperatur von 70 K auf. Das Maximum verschiebt sich zu tieferen Temperaturen mit steigendem Druck. Dieses Verhalten kann mit Hilfe eines Systems von Ratengleichungen erklärt werden unter der Annahme, dass die photogenerierten Ladungsträger aufgrund der geringen Quantenpunktdichte über den *wetting layer* in die Quantenpunkte gelangen. Bei tiefen Temperaturen lokalisieren die Ladungsträger an Fluktuationen im *wetting layer* und erlangen erst durch steigende Temperatur wieder ausreichende Mobilität. Zeitaufgelöste Messungen belegen, dass die Emission aus dem *wetting layer* von nicht-radiativen Prozessen dominiert ist, welche bei steigendem Druck durch den Wegfall des Rekombinationskanals durch die Quantenpunkte an Gewicht verlieren.

Abstract

In this work the optical properties of self-assembled InAs/GaAs and InP/GaP quantum dots under high hydrostatic pressure have been invesigated by means of pholuminescence experiments in a diamond anvil pressure cell.

The particular growth conditions used for the fabrication of the InAs/GaAs sample lead to a multimodal distribution of the quantum dot sizes, which in turn, gives rise to a characteristic emission profile, displaying up to nine clearly separable peaks attributed to the ground-state emission from each quantum dot subensemble of different size. Structural analysis revealed that their size differs in entire monolayer steps. The measured pressure coefficients for each subensemble show a linear dependence on their zero pressure emission energy ranging from 65 meV/GPa for the largest dots to 110 meV/GPa for the smallest ones. Pressure dependent strain simulations based on an atomistic valence force field yield that the pressure coefficient of the InAs band-gap is strongly reduced when InAs is embedded in a GaAs matrix. Taking into account confinement effects within the envelope function approximation, the caclulated pressure coefficients are in good agreement with the experimental findings. Further information about the electronic structure of the quantum dots is found by analyzing the energy at which the confined electron states cross the X-conduction band states of the barrier, which is identified by a sudden quenching of the emission intensity. In this way, it is possible to determine the valence band offsets for the heavy holes corresponding to different dot sizes. By fitting these energies using the calculated confinement energies of the heavy holes, a valence band offset of 290 ± 10 meV for the strained InAs/GaAs quantum dot heterointerface was be obtained.

In the InP/GaP material system self assembled growth of quantum dots has been demonstrated only recently bringing up the question whether the observed emission has direct character in both real and reciprocal space. The large lattice mismatch of about 7.7 % is responsible for the shift of the Γ-point conduction band energy of InP close to the indirect band gap of GaP, which could possibly lead to a type-II confinement resulting in a poor luminescence intensity. The measured pressure dependence of the emission energies and intensities yield, that the main emission peaked at 1.92 eV at ambient pressure is indeed due to a direct optical recombination processes in real and reciprocal space. At low pressures of about 0.2 GPa, the crossover in the quantum dot with the X_{xy} state of InP occurs, leading to a sudden decrease of the luminescence intensity. This is confirmed by the long decay times of the QD emission obtained from time-resolved PL measurements. The QD emission quenches when the X_{xy} state in the dots crosses the X-level confined to the wetting layer at a pressure of about 1.2 GPa and the transition is becoming indirect in both reciprocal and real space. The emission from the quantum dot bound states displays maximal intensity at a temperature of 70 K. This maximum, however, shifts to lower temperatures with increasing pressure. This behavior could be explained by setting up a system of rate equations representing the most important carrier transfer processes. The model implies that due to the low quantum dot density in the InP/GaP system, most of the photoexcited carriers reach the quantum dots through the wetting layer. At low temperatures the carriers localize due to monolayer-size fluctuations in the wetting layer, regaining mobility as the temperature rises. This carrier transfer model is further confirmed by the results of time-resolved photoluminescence, which demonstrate that the decay of the wetting layer emission is governed by non-radiative processes at ambient pressure, which are continuously decreasing in weight as a consequence of the loss of the escape channel through the quantum dots induced by the rising pressure.

List of publications

F. Hatami, L. Schrottke, J.W. Tomm, V. Talalaev, C. Kristukat, A.R. Goñi, W.T. Masselink, Optical properties and carrier dynamics of InP quantum dots embedded in GaP, *Proceedings of the SPIE - The International Society for Optical Engineering* **5352**, 77-89 (2004)

C. Kristukat, M. Dworzak, AR. Goni, P. Zimmer, F. Hatami, S. Dressler, A. Hoffmann, WT. Masselink, C. Thomsen, Recombination Dynamics in Self-assembled InP/GaP Quantum Dots Under High Pressure, *Physica Status Solidi B-basic Research* **241**, 3263 (2004)

C. Kristukat, A.R. Goñi, F. Hatami, S. Dressler, W.T. Masselink, C. Thomsen, High-pressure photoluminescence study of the electronic structure of InP/GaP quantum dots, *Physica Status Solidi B-basic Research* **235**, 412 (2003)

F. Hatami, W. T. Masselink, L. Schrottke, J. W. Tomm, V. Talalaev, C. Kristukat, and A. R. Goñi, InP quantum dots embedded in GaP: Optical properties and carrier dynamics, *Physical Review B* **67**, 85306 (2003)

AR. Goni, C. Kristukat, F. Hatami, S. Dressler, WT. Masselink, C. Thomsen, Electronic Structure of Self-assembled InP/GaP Quantum Dots from High-pressure Photoluminescence, *Physical Review B* **67**, 075306 (2003)

Contents

1. Introduction

Systematic studies of changes in the physical properties of semiconductors under high hydrostatic pressure have contributed significantly to the understanding of these materials at atmospheric pressure. The early pressure devices used in the 1950s were limited to considerably low pressures (< 3 GPa), but due to their design, every experiment formerly carried out at atmospheric pressure could be repeated at high pressures. The separation of the pressure chamber from the pressure generating stage, connected by a strong tube system, allowed for the placement of the sample chamber in a cryostat or between the poles of a magnet and electric contacting could easily be realized. The main interests of the earliest experiments was to determine the change of the fundamental band gap with pressure. By means of electric conductivity measurements under high pressure it was first observed, for example, that silicon and germanium had a different band structure. The intrinsic carrier density is directly related to the band gap and the observation was that in Ge the band gap was increasing with pressure, whereas in Si it was decreasing [1]. Experiments under uniaxial stress have been also very useful in establishing the details of the band structure because state degeneracy is lifted due to the symmetry reduction occurring in the semiconductor crystals stressed under non-hydrostatic conditions. For instance, the two-fold degeneracy of the topmost valence band at the Γ-point can be lifted and the properties of the light- and heavy holes may be studied separately.

From these early measurements of the pressure dependence of the three principal conduction band minima, first on Ge and Si and later on many III-V compounds, an empirical rule emerged [2]: The pressure coefficient of the direct gap at the Γ-point is in the range of 100-150 meV/GPa, that of the $L--\Gamma$ indirect gap is nearly 50 meV/GPa and that of the $X--\Gamma$ indirect gap is between -10 and -20 meV/GPa. This rule is still useful nowadays but the amount and quality of experimental data [3] and ab-initio calculations [4] allow for a refinement of the empirical rule concerning the impact of lattice constant, atomic number and ionicity on the pressure dependence of the gaps.

The development of the the diamond anvil cell was a major breakthrough in the area of high pressure physics, expanding the available pressure range to some 100 GPa, though its application is mostly limited to optical experiments. The extension of the available pressure range made the observation of certain effects possible, which are not sufficiently nonlinear to be observable at

low pressures, like the coupling to higher band extrema in the zinc-blende system.

Applied to semiconductor heterostructures, high pressure photoluminescence experiments can be used to obtain the band offset across the heterointerface, which is an important parameter for device applications, and which is not or only indirect accessible with other methods. However, this technique is limited to some special systems, where the X-band of the barrier drops below the confined state when applying pressure, resulting in a transfer of the photogenerated electrons to the barrier and, thus, producing a significant drop in the luminescence intensity. The photon energy at which the intensity decreases is just the indirect gap of the barrier at that pressure minus the valence band offset (VBO), corrected by the quantum confinement of the holes. In this way, the VBO may be determined directly with meV precision from the experiment without the need of a fit to some model. Another application is the study of Γ-X band mixing effects which are expected to be larger in nanostructures because of the sharp potential discontinuities and confinement effects. The coupling depends on the interaction potential and the energy separation between the states. The latter can be tuned knowing the effect of pressure on the bands, thus, allowing for a convenient test of the theory. In a similar way, pressure can be a significant parameter for resonant tunnelling experiments of electrons in superlattices.

Quantum dots have become a field of intense study in semiconductor physics in the last decade due to their peculiar optical and electrical properties which are very promising for potential applications in optoelectronics. Among the different fabrication methods, the self-assembled growth which is based on the driving force of the built-in strain induced by a lattice mismatch of the constituent materials, is the most commonly used. As a general strain pattern can be decomposed into hydrostatic and uniaxial components, the effects of the internal strain on the confined states in a quantum dot can be analyzed, if previous knowledge of the effects of hydrostatic and uniaxial pressure on the bands is available from pressure experiments. Due to its three-dimensional nature, the strain field of a quantum dot is a complex matter compared to that of strained quantum wells. The determination of the strain distribution by means of atomistic valence-force field models or continuum mechanics is therefore crucial in order to calculate the energy levels and wave functions.

In this work, high pressure photoluminescence experiments on self-assembled quantum dots have been carried out. In addition, strain simulations as a function of external pressure have been performed in order to interpret the experimental results. The work is structured as follows:

- In chapter 2 I will describe the pressure techniques utilizing the diamond anvil cell for experiments at liquid He temperatures and I will sketch the experimental setups used.

- Chapter 3 will describe the formation and properties of self-assembled quantum dots and

address the necessary theoretical background to describe the band structure of semiconductors and understand the effects of quantum confinement and strain.

- In chapter 4 I will present the results from photoluminescence experiments on InAs/GaAs and InP/GaP quantum dots under high pressure. For the former system the experimental findings will be discussed in comparison with pressure-dependent strain-field modelling. For the InP/GaP system I will demonstrate the power of high pressure experiments to unravel the band lineups and for the discussion of the carrier dynamics exploiting the temperature dependence of the emission and the results from time-resolved photoluminescence under high hydrostatic pressure.

2. Experimental

In this chapter I will describe the techniques to create high hydrostatic pressure up to 10 GPa and how to measure the applied pressure *in-situ* and I will sketch the setups used for photoluminescence (PL) and time resolved photoluminescence (TRPL) measurements.

2.1. Pressure techniques

One of the pioneers in high pressure technique was P.W.Bridgman who was awarded the nobel prize in 1946. He introduced the concept of the anvil cell which is widely used nowadays. Hydrostatic pressure is created through the deformation of some sealing material with a hole in it serving as pressure chamber which is placed between two pistons. Bridgman used tungsten carbid which is very hard but opaque and thus does not allow optical measurements. Important milestones on the way to the diamond anvil cell were the introduction of diamonds as anvil material[5], the use of a sealing material between the diamonds[6] and the application of the ruby fluoresence method for pressure determination[7].

2.1.1. The diamond anvil cell

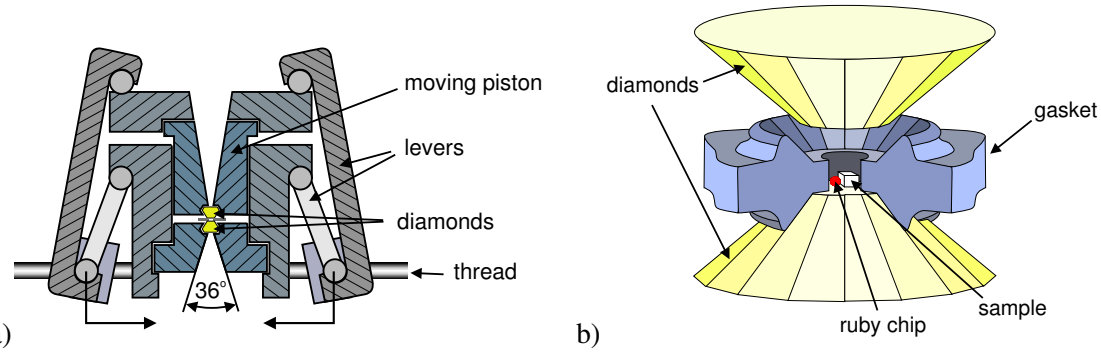

Figure 2.1: Sketch of the diamond anvil cell. On the left side the lever mechanism which moves the upper piston is shown. The end points of the levers are driven by two threads. When using the cell in a cryostat two long rods connect the threads with a gear outside the cryostat. The right hand side shows an illustration of the two diamonds and the gasket.

The diamond anvil cell (DAC) is a device particularly suited to perform optical measurement under high hydrostatic pressure. The basic principle of a DAC is quite simple. The sample volume is defined inside a 200-300 μm hole drilled into a metal gasket which will closed on top and bottom by the flat parallel faces of two diamond anvils (2.1b). The sample is subjected to pressure when the two diamonds are pushed together decreasing the chamber volume while slightly deforming the gasket. Depending on the needed pressure range and sample volume different cells have been built and most of them comprise a movable piston which holds one of the diamonds and some kind of lever mechanism to apply the pressing force. The cell used in the experiments (see fig.2.1a) presented here was designed by *Syassen* and *Holzapfel*[8] and allows for measurements up to 16 GPa. Due to the large aperture angle of 36 ^{o} it is suitable even for Raman experiments.

The gasket is made out of a nickel-chromium alloy referred to as Inconel X-750[1] which is chosen for its mechanical strength and hardness. The fabrication process of the raw gaskets - small discs of 8 mm in diameter and 250 μm in thickness - induces strain in the material which has to be released to regain its natural hardness. Therefore they have to run through a tempering procedure which is described in (ANHANG). The discs are then pressed with the diamonds creating a faceted indention of about 100 μm thickness and 400 μm diameter. This cold forming step represents an additional hardening. Finally, a hole of 200-300 μm in diameter is drilled into its center. This hole is the actual sample chamber which will be loaded with the sample whose dimensions must not exceed 100x100x50 μm^3 and a small ruby chip for the pressure determination.

Various organic liquids and condensed gases have been used as pressure medium to assure hydrostatic conditions in the sample chamber. ^{4}He is often chosen for low temperature measurements due to its nearly hydrostatic behaviour up to 60 GPa[9] and its suprafluid state below 2.2 K which simplifies the filling of the cell. For room temperature applications a 16:3:1 mixture of methanol, ethanol and water is used.

A review of common high pressure techniques can be found in [10].

2.1.2. in-situ pressure determination

The pressure in the anvil cell is determined in situ via the pressure dependent shift of the ruby fluorescence. For that purpose a small chip of ruby is placed besides the sample inside the pressure chamber. Ruby is Cr^{3+}-doped Al_2O_3 (Sapphire) and shows a well known strong red fluorescence. The crystal symmetry of Ruby is rhombohedral, the Cr^{3+} ions and their six first neighbours form a distorted oactahedron whose symmetry is C_3[11]. The resulting crystal field

[1] http://www.magellanmetals.com/inconel_X750.htm

leads to a splitting of the degenerated energy levels of the 3d electrons of Cr^{3+} giving rise to the two strong fluorescent transitions denoted R1 and R2 with energies $E_{R1} = 14418\,\mathrm{cm}^{-1}$ and $E_{R2} = 14447\,\mathrm{cm}^{-1}$. Applying external pressure decreases the interatomic length and therefor rises the crystal field. The level splitting increases resulting in in net reduction of the R1 and R2 transitions. The dependence of the ruby fluorescence on hydrostatic pressure has been determined up to 80 GPa[9] and follows

$$p = \frac{A}{B}\left[\left[1 + \left(\frac{\lambda - \lambda_0}{\lambda_0}\right)\right]^B - 1\right], \tag{2.1}$$

where $A = 1904\,\mathrm{GPa}$ and $B = 7.665\,\mathrm{GPa}$, λ_0 and λ are the wavelength of the R1 at ambient and applied pressure respectively. As small chips of ruby might be strained internally the values for λ_0 may differ for each chip representing an error source for the pressure determination.

For a precise determination the dependence on temperature has to been taken into account. The pressure coefficients A and B are independent of temperature in good approximation[12][13] whereas the energy of the R1 and R2 lines shift with temperature. At low temperatures only the low energy R1 line is visible. The temperature dependence of the R1 line is best described by a two-phonon Raman-process model[14], which yields:

$$\nu_R(T) - \nu_R(0) = \alpha\left(\frac{T}{\Theta}\right)^4 \int_0^{\Theta/T} dx \frac{x^3}{e^x - 1} \quad , \tag{2.2}$$

where $\nu(T)$ is the energy of the R_1 band at temperature T and ambient pressure and $\nu(0)$ that at 0 K. The parameters Θ and α have been determined by fitting equation (2.2) to a comprehensive set of experimental data as $\Theta = 760\,\mathrm{K}$ and $\alpha = 419\,\mathrm{cm}^{-1}$[15].

All pressure readings in this work have been calculated using equations (2.1) and (2.2). The energies of the ruby lines were determined by fitting the calibrated spectra with two voigt profiles which accounts for the convolution of the lorentian line shape with the spectrometer response. The 692.47 nm neon line has been used for calibration.

2.1.3. Low temperature pressure techniques

When using the DAC at low temperatures with ^{4}He as pressure medium it cannot be sealed outside the cryostat, fact that complicates the loading of the cell. Thus, the DAC has to be loaded with the sample and a ruby chip, the diamonds however must not close the sample chamber comletely. The cell is placed into the cryostat and is immersed in fluid ^{4}He which is being pumped to keep it in the superfluid state below 2.19 K. Under this condition ^{4}He easily enters into the cell, filling it comletely and the DAC can be sealed by carefully aproaching the diamonds. As ^{4}He instantly crytallises when subjected to pressure at 2 K the cell has to be heated well

above the melting point to relax non-hydrostatic strain. When cooling down again into the solid phase it is assumed that the pressure on the sample is mostly hydrostatic. The same applies if the pressure is about to be changed. It is crucial to reach a point in phase space well above the melting line such that He is liquid during the pressure change (see section C for the ^{4}He melting curve). Allowing the cell to relax for some minutes usually alters the pressure until it reaches its final value.

2.2. Spectroscopic techniques

2.2.1. Photoluminescence spectroscopy

All photoluminescence spectra in this work have been recorded using a single 0.85 m Czerny-Turner spectrometer with a grating of 600 lines/mm. The grating is blazed for a wavelength of 1.6 μm so that, depending on the sample, measurements were performed in first to third order. Detection of the dispersed signal occurred with a liquid-nitrogen cooled germanium diode for the near infrared region and a gallium arsenide photomultiplier for the visible range. For excitation the 514 nm line of an argon laser and the 441 nm line of an helium-cadmium laser were used.

The ruby spectra for the pressure determination were taken in 2nd order with a slit width of 70 μm at both slits which gives a spectral resolution of about 0.3 Å.

2.2.2. Time-resolved photoluminescence (TRPL)

To study the temporal evolution of photoluminescence processes both excitation and detection has to occur faster than the typical decay times involved, i.e. with a temporal resolution in the sub-nanosecond range.

Excitation system The creation of ps laser pulses is achieved using a Nd:YAG pumped dye laser. The Nd:YAG laser creates 100 ps long pulses through active mode locking at λ=1064 nm with a repetition rate of 76 MHz. The light passes a frequency doubling crystal and is mixed again with the 0th harmonic to obtain the triple frequency at 355 nm which is used to pump the dye (Coumarin102, 462-497 nm). The resonator length of both lasers are equal so that the excitation in the dye occurs synchronous with the total resonator circulation time of one dye laser pulse. Without further action taken the minimal length of the dye laser pulse is about 5 ps. A so called pulse picker allows for throttling the pulse repetition rate. It consists of a acoustical-optical modulator which dumps a selectable number of pulses before letting one pulse to pass through the output mirror. This is necessary to allow the photoluminescence to decay completely before the next excitation pulse reaches the sample.

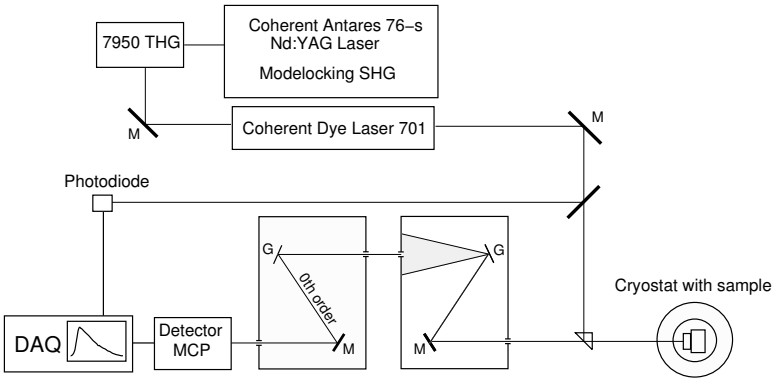

Figure 2.2: Setup for time resolved photoluminescence measurements. G: grating, M: mirror, MCP: multichannel plate, SHG: second harmonic generation, THG: third harmonic generation

Detection system In addition to an ordinary photoluminescence setup, a fast detector, in this case, a multichannel plate (MCP) has to be used. It permits single photon counting in conjunction with a suitable data acquisition stage. As shown in figure 2.2, a second monochromator has been installed in reverse sense to account for the different optical paths depending on wavelength. This configuration corresponds to a double monochromator in subtractive mode but with the intermediate slit used as output slit and the output slit open. A beam splitter directs part of the excitation pulses to a photodiode which is needed to trigger the measurement, i.e. for temporal resolution. The excitation intensity is set such that per pulse only one single photon emitted from the sample reaches the detector and a single event is registered. The time difference to the trigger event is the actual measurement. A *time-to-amplitude* converter (TAC) prepares the time difference information to be processed by a multichannel analyser (MCA) which sorts all events into different channels according to their amplitudes. Thus, to be able to record a single decay process a large number of excitations have to occur. The measured decay corresponds to the overall response of the setup convoluted with the actual signal of the sample:

$$s(t) = \int_{-\infty}^{+\infty} e(t-\tau)r(\tau)d\tau, \tag{2.3}$$

being $s(t)$ the measured signal, $r(t)$ the system response function and $e(t)$ the emission dynamics. To be able to extract the information about the decay, the system response has to be measured first by recording directly the laser diffusely reflected at some object near the sample. The time constants of the decay processes are determined by fitting a model with a variable number of decaying and rising components to the data. Instead of deconvoluting the measured signal by the system response, the model itself is convoluted with the system response before fitting it to the data.

3. Theory

3.1. Formation and properties of self-assembled quantum dots

A semiconductor structure is thought to be low-dimensional, if the motion of the carriers is confined in at least one direction within a spatial extent comparable to the carrier de-Broglie wavelength. In that direction the carrier momentum is quantized with an energy spectrum determined by the discrete solutions of the Schrödinger equation, the eigenenergies. This can be achieved, e.g. by growing a sequence of different materials which differ in the band-gap energy. These so called semiconductor heterostructures are classified according to the dimensionality of the confinement into quantum wells (QW, 2D), quantum wires (QWR, 1D) and quantum dots (QD, 0D). As a consequence of the reduced dimensionality the density of states of the confined carriers changes accordingly, being quasi-continuous for bulk semiconductors and δ-function like for quantum dots. Thus, thermal broadening of the carrier distribution can be avoided in QDs, if the level splitting is larger than the thermal energy $k_B T$. In fact, cathodoluminescence measurements on single quantum dots reveal linewidths in the μeV range independent of temperature [16].

The fabrication of nanometer-sized quantum dots using electron beam lithography and wet chemical etching of quantum wells has been demonstrated down to a size of 20 nm [17]. A completely different growth method is the so called self-organized growth which can be observed upon epitaxial deposition of highly strained semiconductors one on top of the other. The first reports on the strain-driven formation of islands dealt with InAs/GaAs superlattices Goldstein et al. [18]. After this discovery, this growth technique has been applied to many different systems of elemental semiconductors and III-V and II-VI compounds using both metalorganic chemical vapor deposition (MOCVD) and molecular beam epitaxy (MBE) [19–26]. Depending on the growth conditions and materials several growth modes have been observed. The samples studied in this work are grown in the Stranski-Krastanov mode [27], which starts with the two-dimensional growth of a compressively strained epitaxial layer, the wetting layer, up to a critical thickness. It then proceeds three dimensional by forming isolated islands on the thin wetting layer, since in that way the system lowers its energy by relaxing strain. According to Shchukin et al. [28] a stable configuration of an ensemble of strained islands for a given total volume with

an optimum equilibrium size does exists. The energy of such an array is given by

$$E = \Delta E_{vol} + \Delta E_{facets} + \Delta E_{edges} + E_{edges} + E_{inter}, \tag{3.1}$$

where the first three terms correspond to elastic relaxation energy related to the volume ($E < 0$), the facets ($E <> 0, \sim L^{-1}$) and the edges ($E < 0, \sim -L^{-2} \ln L$) of the islands and the latter two terms are a short-range edge energy ($E > 0, \sim L^{-2}$) and an island-island interaction energy ($E > 0, \sim L^{-\frac{2}{3}}$). Negative energies represent the energy gain due to island formation, whereas positive ones correspond to the energy cost of surface and edge formation and repulsive island-island interactions. All terms but the volume elastic relaxation energy depend on a normalized island size L and the interplay of the concurrent terms finally leads to a size for which the total energy is minimized. The energetically favored shape of an island was found to be that of pyramid with $\{110\}$ facets.

In real quantum dots, the shape, size and composition depend on many parameters of the growth process, like temperature, growth rates, growth interruption times before capping, etc. In fact, structural analysis methods reveal that the shape of the quantum dots in the samples studied in this work is that of a truncated pyramid [29, 30], being much larger in the $\{001\}$ plane than in the [001] direction. Besides, usually a broad distribution of the structural parameters exists. This results in an inhomogeneous broadening of the fundamental emission line, which depends heavily on size, composition and shape of the quantum dots. So the intrinsic very small linewidth of a single quantum dot cannot be observed in standard photoluminescence experiments, which usually probe a huge number of quantum dots at the same time. Typically, the PL spectrum of quantum dot samples exhibits a width (FWHM) of 20 to 100 meV. If the average size is rather large, monolayer size fluctuations have a smaller impact on the confinement energy resulting in a considerably narrower energy spectrum [31]. Thus we can expect that for one material system the lowest spectral widths can be found in those samples, which have in average large dots thus emitting at lower energies.

3.2. Band structure of semiconductors

In order to calculate the band structure or dispersion curve for electrons in a crystal, i.e. the function $E(\mathbf{k})$, where $\mathbf{k}$ is the electron wave vector, several simplifications are necessary. The first approximation is to separate the electrons into core and valence electrons. The former are those in the completely filled shells, whereas the latter form the orbitals of the outmost incompletely filled shells, e.g. the $3s^2$ and $3p^2$ electrons for silicon. They are responsible for the chemical bond. The four valence electrons are arranged in four equally hybridized sp^3 orbitals

directed towards the corners of a regular tetrahedron. As the core electrons are strongly bound and localized around the nuclei they can be treated as one unit together with the nuclei forming an ion core. The next approximation is the *Born-Oppenheimer* or adiabatic approximation which takes into account the fact that the ions are much heavier than the electrons and therefore they move much slower. Electrons can respond to ionic motion almost instantaneously so that the ions are stationary from the electron point of view. The remaining Hamiltonian for crystal electrons is

$$\boldsymbol{H_e} = \sum_i \frac{\boldsymbol{p}_i^2}{2m_i} + \frac{1}{2}\sum_{i,i'} \frac{e^2}{|\boldsymbol{r_i} - \boldsymbol{r_{i'}}|} - \sum_{i,j} \frac{Z_j e^2}{|\boldsymbol{r_i} - \boldsymbol{R_{oj}}|}. \tag{3.2}$$

The three terms are the kinetic energy of the electrons, the electron-electron and electron-ion interaction between electrons at $\boldsymbol{r_i}$ and ions at their frozen lattice positions $\boldsymbol{R_{oj}}$ with indices i and j, respectively. The letters Z, e and m denote the atomic number, electron charge and mass, respectively, and $\boldsymbol{p}$ is the electron momentum operator. This Hamiltonian is still far from being solvable for a crystal which typically contains about 10^{23} valence electrons/cm^3. The next step is to use the *Hartree* or mean-field approximation which assumes that each electron moves in the average field created by all other electrons and ions. Thus the one electron Schrödinger equations are identical for each electron and given by

$$\boldsymbol{H_e}\psi(\boldsymbol{r}) = \left(\frac{\boldsymbol{p^2}}{2m} + V(\boldsymbol{r})\right)\psi(\boldsymbol{r}) = E\psi_j(\boldsymbol{r}), \tag{3.3}$$

where $V(\boldsymbol{r})$ is a periodic potential for a crystal, which incorporates all electronic interactions. The solutions of this one-electron Hamiltonian are plane waves times an envelope function, a so called *Bloch* function, which has the periodicity of the lattice:

$$\psi_{n\boldsymbol{k}}(\boldsymbol{r}) = e^{i\boldsymbol{k}\cdot\boldsymbol{r}} u_{n\boldsymbol{k}}(\boldsymbol{r}) \qquad E = E_{n\boldsymbol{k}} \tag{3.4}$$

The index n is the band index which distinguishes among the many independent eigenfunctions existing for a given $\boldsymbol{k}$. The allowed $\boldsymbol{k}$ vectors are determined by the boundary conditions of macroscopic periodicity. It can be shown that the volume that each state occupies in reciprocal space is inversely proportional to the total crystal volume considered and, thus, the number of possible $\boldsymbol{k}$-points grows with the size of the crystal. In a macroscopic size crystal the allowed values of $\boldsymbol{k}$ form a quasi continuum. The corresponding eigenvalues $E_n(\boldsymbol{k})$ represent the actual band structure. Only at high symmetry points of the Brillouin zone, particularly the Γ-point, the Bloch functions are known explicitly because their symmetry can be easily analyzed by applying the symmetry operations of the crystal point group. Four Γ-point Bloch functions are of special interest since their linear combinations form the wavefunctions of the topmost valence band and lowest conduction band. The functions are labelled $|S\rangle, |X\rangle, |Y\rangle$ and $|Z\rangle$, and they transform in

the same way as the atomic s, p_x, p_y, p_z functions under the symmetry operations of the crystal point group.

The projection of $E_n(\boldsymbol{k})$ onto the first Brillouin zone, i.e. subtracting integer multiples of the reciprocal lattice vector $\boldsymbol{K}$ such that $\boldsymbol{k}$ is within the first zone, is called the reduced zone scheme. It is commonly used to display band structures along high symmetry directions. This kind of illustration is not only chosen due to its compactness, it also accounts for the fact that $\boldsymbol{k}$ is conserved for transitions between two states $\boldsymbol{k}$ and $\boldsymbol{k} - n\boldsymbol{K}$, where n is an integer, is represented by a vertical transition in the reduced zone scheme. The Brillouin zone for the cubic face-centered diamond or zinc-blende lattice is shown in Fig. 3.1. The center of the Brillouin zone

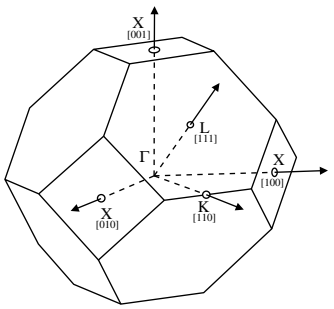

Figure 3.1: The Brillouin zone of the fcc diamond lattice

is denoted by Γ. The high-symmetry directions [100],[110] and [111] of the fcc lattice and the group of points on the line between them and the zone center Γ are denoted by X, K and L and Δ, Σ and Λ, respectively. We see from Fig. 3.1 that there are six equivalent X and eight equivalent L and K points, respectively, thus, degeneracy is to be expected.

The main problem when calculating the band structure is to find a suitable potential $V(\boldsymbol{r})$ for which the solution of the Schrödinger equation (3.3) is feasible. The wavefunction strongly depends on its position and will have an atomiclike oscillatory character near the atom core and a plane-wave like between two atoms. Hence, one idea is to divide the wavefunction spatially into a smooth part (the pseudo-wave function) and an oscillatory part, as it is hopeless to approximate the wave function by a few plane waves everywhere in space. These oscillations are a manifestation of the high electronic kinetic energy within the core, which provides an effective repulsion for the electrons. Accordingly, the strong ionic potential is replaced by a weaker effective potential, the pseudopotential. There are several methods to compute the wavefunctions using pseudopotentials. Among them self-consistent ab-initio methods are the most elaborated and nowadays widely used. In contrast to empirical methods, the ab-initio calculations do not depend on experimental input, i.e the pseudopotential is constructed by calculating the complete atom shell including the core levels.

Many features of the band structure depend upon the symmetry of the electron orbitals which, in turn, depend themselves on the crystal symmetry. Symmetry is usually discussed using the

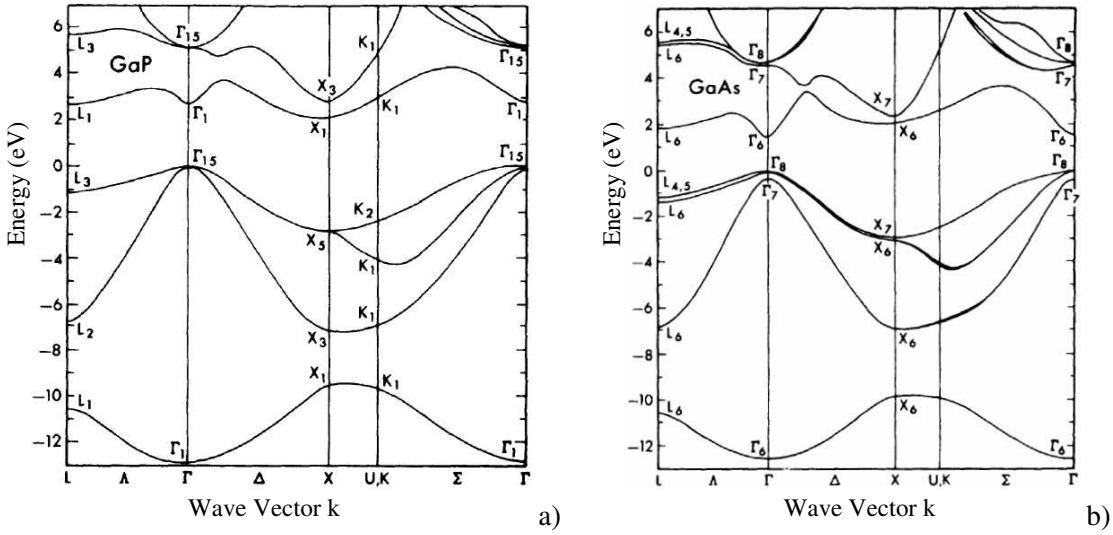

Figure 3.2: The band structure of a) GaP and b) GaAs calculated by using nonlocal pseudopotentials [32]. The spin-orbit interaction is considered to be very small in GaP and was therefore neglected.

methods of group theory. The point group of the diamond and zinc-blende lattice are denoted O_h and T_d, respectively. Figure 3.2a) shows the band structure of GaP calculated with nonlocal empirical pseudopotentials. The irreducible representations of the band structure are indicated at the extrema. The orbital character of Γ_1 and Γ_{15} are pure $|s\rangle$ and $|p\rangle$, respectively. Thus at the top of the valence band there are three degenerate $|p\rangle$ bands and the lowest conduction band is a pure $|s\rangle$ state. Away from the Γ points the bands have mixed character. The wavefunctions are denoted *p-like* ($|\psi|^2 \sim \sin^2 r$) and *s-like* ($|\psi|^2 \sim \cos^2 r$) according to their position in relation to the lattice points. An s-like type wavefunction does not vanish at the ion whereas the probability density of the p-like type is zero at the lattice points. That will be of importance for the consideration of the effects of pressure on the band structure.

The degeneracy of the valence band is partly lifted by the spin-orbit (SO) interaction. The Hamiltonian for the spin-orbit interaction is given by

$$H_{SO} = \frac{\hbar}{4c^2m^2}(\nabla V \times \boldsymbol{p}) \cdot \boldsymbol{\sigma} \tag{3.5}$$

where the components of $\boldsymbol{\sigma}$ are the Pauli spin matrices. If one considers for simplicity a spherical potential V the Hamiltonian can be written as

$$H_{SO} = \frac{\hbar}{4c^2m^2}\frac{1}{r}\frac{dV}{dr}(\mathbf{r} \times \boldsymbol{p}) \cdot \boldsymbol{\sigma} = \lambda \boldsymbol{L} \cdot \boldsymbol{S}, \tag{3.6}$$

where $\boldsymbol{L}$ is the orbital angular momentum operator, $\boldsymbol{S}$ is the spin angular momentum operator and $\lambda = (dV/dr)/2m^2c^2r$. Expressed in terms of the total angular moment $\boldsymbol{J}$, the expectation

value of $\boldsymbol{L}\cdot\boldsymbol{S}$ is

$$\begin{aligned}\langle \boldsymbol{L}\cdot\boldsymbol{S}\rangle &= \frac{1}{2}\langle \boldsymbol{J}^2-\boldsymbol{L}^2-\boldsymbol{S}^2\rangle \\ &= \frac{\hbar^2}{2}(j(j+1)-l(l+1)-s(s+1)),\end{aligned} \tag{3.7}$$

using $\boldsymbol{J}^2=\boldsymbol{L}^2+\boldsymbol{S}^2+2\boldsymbol{L}\cdot\boldsymbol{S}$. The $|p\rangle$ bands at the top of the valence bands have $l=1$ and thus $j=\frac{3}{2}$ or $\frac{1}{2}$, resulting in $\boldsymbol{L}\cdot\boldsymbol{S}=-\hbar^2$ or $\boldsymbol{L}\cdot\boldsymbol{S}=+\frac{\hbar^2}{2}$, respectively. This means that the states are split by an amount Δ_0 proportional to $\frac{3}{2}\hbar^2$, the double degenerate $j=\frac{3}{2}$ state moving up by $\Delta_0/3$ and the single $j=\frac{1}{2}$ state moving down by $2\Delta_0/3$. The $j=\frac{3}{2}$ state remains degenerated at $\boldsymbol{k}=0$ but splits when leaving the Γ-point except when going along the cube axis. The magnitude of the splitting is comparable to that of the constituent atoms. The effect scales with the atomic number and therefore cannot be ignored for heavy elements. In binary compounds the anion contribution to the split-off energy is weighted more, reflecting its larger influence on the $|p\rangle$ valence bands. In GaAs $\Delta_0\approx 0.34\,\mathrm{eV}$ and thus the spin-orbit interaction has to be included in the unperturbed Hamiltonian, whereas e.g. in GaP ($\Delta_0\approx 0.08\,\mathrm{eV}$) and it is commonly ignored.

The inclusion of the spin in the Hamiltonian requires that the symmetry group of the crystal is expanded by symmetry operations of spin wavefunctions. These expanded groups are known as double groups. Figure 3.2b) shows the calculated band structure of GaAs where, in contrast to GaP, the spin-orbit coupling has been considered and the band extrema are denoted by the irreducible representation of the double group. Their relation to the point group is given in table 3.1.

$\mathbf{T_d}$	Γ_1	Γ_{15}	X_5	X_1+X_3	L_1	L_3
$\mathbf{T_d}\times\mathbf{D}$	Γ_6	$\Gamma_7+\Gamma_8$	X_6+X_7	X_6+X_7	$L_6+L_4+L_5$	L_6

Table 3.1: Decomposition of the irreducible representations of the T_d point group into their double group representations.

3.2.1. The $k\cdot p$ theory and the effective mass

The methods for the global description of the band dispersion, like e.g. the pseudopotential method, rarely provide explicit expressions for common quantities such as effective masses and wavefunctions. Often is also sufficient to have knowledge about the band structure over a small range of $\boldsymbol{k}$ around the band extrema. The $\boldsymbol{k}\cdot\boldsymbol{p}$ method [33] is a local description of the band structure which provides simple analytical expressions for high symmetry points of the Brillouin zone. However, the band structure over the entire Brillouin zone can be extrapolated from the

zone center energies and optical matrix elements. These inputs can be obtained from the transition energies and oscillator strengths measured by optical experiments. The $\boldsymbol{k}\cdot\boldsymbol{p}$ method is derived from the one-electron Schrödinger equation (3.3) by assuming that the solutions are the Bloch waves of Eq. (3.4). The resulting Schrödinger equation reads

$$\left(\frac{p^2}{2m}+\frac{\hbar\boldsymbol{k}\cdot\boldsymbol{p}}{m}+\frac{\hbar^2k^2}{2m}+V\right)u_{n\boldsymbol{k}}=E_{n\boldsymbol{k}}u_{n\boldsymbol{k}}, \tag{3.8}$$

neglecting for the moment the spin-orbit coupling. Obviously at $k=0$ (3.8) reduces to

$$\left(\frac{p^2}{2m}+V\right)u_{n\mathbf{0}}=E_{n\mathbf{0}}u_{n\mathbf{0}}. \tag{3.9}$$

The solutions of (3.9) form a complete and orthonormal set of basis functions. If once $E_{n\mathbf{0}}$ and $u_{n\mathbf{0}}$ are known then the terms including k in (3.8) can be treated as perturbations using degenerate or nondegenerate perturbation theory. This of course works best for small values of k. To extrapolate over the complete Brillouin zone more energy gaps and matrix elements will be needed. The simplest application of the $\boldsymbol{k}\cdot\boldsymbol{p}$ theory is the calculation of band structure of the lowest non-degenerate conduction band, when the spin-orbit interaction is neglected. The eigenvalues $E_{n\boldsymbol{k}}$ can be expanded to second order in k in terms of the unperturbed energies $E_{n\mathbf{0}}$ by treating the terms involving k as perturbations. Assuming that the band structure has an extremum at $\boldsymbol{k}=\mathbf{0}$ the linear terms in k vanishes.

$$E_{n\boldsymbol{k}}=E_{n\mathbf{o}}+\frac{\hbar^2+k^2}{2m_0}+\frac{\hbar^2}{m_0^2}\sum_{m\neq n}\frac{|\langle u_{n\mathbf{0}}|\boldsymbol{k}\cdot\boldsymbol{p}|u_{m\mathbf{0}}\rangle|^2}{E_{n\mathbf{o}}-E_{m\mathbf{0}}}. \tag{3.10}$$

It is conventional to express the energy for small $\boldsymbol{k}$ in terms of the so called effective mass $m^\star$ of the band:

$$E_{n\boldsymbol{k}}=E_{n\mathbf{o}}+\frac{\hbar^2k^2}{2m^\star}, \tag{3.11}$$

where

$$\frac{1}{m^\star}=\frac{1}{m_0}+\frac{2}{m_0^2k^2}\sum_{m\neq n}\frac{|\langle u_{n\mathbf{0}}|\boldsymbol{k}\cdot\boldsymbol{p}|u_{m\mathbf{0}}\rangle|^2}{E_{n\mathbf{o}}-E_{m\mathbf{0}}}. \tag{3.12}$$

This shows that the effective mass is governed by two factors: The squared strength of the matrix element between the Bloch functions of the band of interest and those at all other $k=0$ gaps and the sign and the magnitude of the Γ-point band gaps. It can be shown by symmetry considerations that the conduction band wavefunction of a zinc-blende semiconductor, which has Γ_1 (Γ_6 with spin-orbit coupling) symmetry can couple only to wavefunctions with Γ_{15} (Γ_8) symmetry via the $\boldsymbol{k}\cdot\boldsymbol{p}$ term. That means that the effective mass of the conduction band will mostly be determined by the coupling to the next nearest band with Γ_{15} (Γ_8) symmetry, which is the top valence band. Thus for the conduction band Eq. (3.12) simplifies to

$$\frac{1}{m_c}=\frac{1}{m_0}+\frac{|\langle\Gamma_{1_C}|\boldsymbol{k}\cdot\boldsymbol{p}|\Gamma_{15_V}\rangle|^2}{E_0m_0^2k^2}\approx\frac{1}{m_0}+\frac{2P^2}{m_0^2E_0}. \tag{3.13}$$

electrons	$\|J,m_j\rangle$	Ψ	$E(\boldsymbol{k}=0)$
$\|\frac{1}{2},\pm\frac{1}{2}\rangle$	$i\|S\uparrow\downarrow\rangle$	0	
light holes	$\|\frac{3}{2},\pm\frac{1}{2}\rangle$	$-\sqrt{\frac{2}{3}}\|Z\uparrow\rangle \pm \frac{1}{\sqrt{6}}\|(X\pm iY)\downarrow\uparrow\rangle$	$-E_0$
heavy holes	$\|\frac{3}{2},\pm\frac{3}{2}\rangle$	$\frac{1}{\sqrt{2}}\|(X\pm iY)\uparrow\downarrow\rangle$	$-E_0$
split-off holes	$\|\frac{1}{2},\pm\frac{1}{2}\rangle$	$\sqrt{\frac{1}{\sqrt{3}}}\|Z\uparrow\rangle \pm \frac{1}{\sqrt{3}}\|(X\pm iY)\downarrow\uparrow\rangle$	$-E_0-\Delta_0$

Table 3.2: The eight wavefunctions used in the Kane model.

The matrix element P is constant for most group-IV, III-V and II-VI semiconductors, with $2P^2/m_0 \approx 20\,\mathrm{eV}$ and the results obtained from Eq. (3.13) are in very good agreement with experimental data.

This simple solution has several shortcomings which are not negligible when calculating the valence band structure. And improved method to solve the $\boldsymbol{k}\cdot\boldsymbol{p}$ Schrödinger equation including spin-orbit coupling was proposed by *Kane* [34]. Within the Kane model, the terms involving $\boldsymbol{k}$ are treated exactly for a limited set of bands which are energetically close ($\Gamma_6,\Gamma_7,\Gamma_8$), while the coupling to the other bands is treated within second order perturbation theory. It is desirable to have a basis in which the spin-orbit coupling term is already diagonal which means that $\boldsymbol{J}$ and its projection J_z are good quantum numbers. In that basis, the eight band edge wavefunctions are linear combinations of the elementary Bloch functions $|S\uparrow\downarrow\rangle, |X\uparrow\downarrow\rangle, |Y\uparrow\downarrow\rangle$, $|Z\uparrow\downarrow\rangle$ (see table 3.2). The solution are the eigenvalues of an 8×8 matrix [35]. The eigenenergies depend on three parameters: The bandgap E_0, the spin-orbit coupling energy Δ_0 and the interband matrix element P. If $\lambda(\boldsymbol{k})$ denotes the energy deviation from the parabolic dispersion

$$\lambda(\boldsymbol{k}) = E(\boldsymbol{k}) - \frac{\hbar^2 k^2}{2m_0}, \tag{3.14}$$

the eigenvalues read as

$$\lambda(\boldsymbol{k}) = -E_0 \tag{3.15}$$

$$\lambda(\boldsymbol{k})(\lambda(\boldsymbol{k})+E_0)(\lambda(\boldsymbol{k})+E_0+\Delta_0) = \hbar^2 k^2 P^2\left(\lambda(\boldsymbol{k})+E_0+\frac{2\Delta_0}{3}\right). \tag{3.16}$$

If we take $\boldsymbol{k} \parallel \boldsymbol{J} \parallel z$ the solutions can be classified according to m_j: Eqs. (3.15) and (3.16) correspond to $m_j=\pm 3/2$,$m_j=\pm 1/2$ states, respectively. We notice that the dispersion relations are isotropic as $\lambda(\boldsymbol{k})$ depends only on k^2. The effective mass of the $m_j=\pm\frac{3}{2}$ state coincides with the free electron mass therefore denoted heavy. This is due to the lack of $k_z p_z$ coupling between $\Gamma_8^{\pm 3/2}$ and Γ_6 $\langle S|p_z|X+iY\rangle = 0$ in the unperturbed Hamiltonian. The $m_j=\pm\frac{1}{2}$ states, however, are associated with light particles (Γ_6 electrons, Γ_8 light holes, Γ_7 holes) since their mass is considerably lighter than m_0. It is common to treat a filled valence band with one

electron missing as an empty band containing one *hole*. Like this, the curvature of the valence bands and thus their effective masses are positive too. The Γ_7 band is commonly called split-off band due to its energetic separation from light and heavy holes.

At the band edges ($k = 0$) the resulting effective masses are

$$\frac{m_0}{m_{\Gamma_6}} = 1 + \frac{2P^2}{3m_0}\left(\frac{2}{E_0} + \frac{1}{E_0 + \Delta_0}\right) \tag{3.17}$$

$$\frac{m_0}{m_{\Gamma_8^{\pm 3/2}}} = 1 \tag{3.18}$$

$$\frac{m_0}{m_{\Gamma_8^{\pm 1/2}}} = 1 - \frac{4P^2}{3m_0 E_0} \tag{3.19}$$

$$\frac{m_0}{m_{\Gamma_7}} = 1 - \frac{2P^2}{3m_0\,(E_0 + \Delta_0)}. \tag{3.20}$$

This model yields for the light particles effective masses which agree very well with experiments and it reflects the band nonparabolicity of these bands, i.e. the effective mass becomes larger when the energy increases. The nonparabolicity is pronounced for semiconductors where the band gap and the spin-orbit coupling is small. Instead of using Eq. (3.16) we can write the dispersion relation in the more explanatory form as a function of the energy-dependent effective mass:

$$\lambda = \frac{\hbar^2 k^2}{2m(\lambda)}, \tag{3.21}$$

where $m(\lambda)$ has to be obtained from Eqs. (3.15-3.17) like demonstrated in Ref. [35]. Figure 3.3

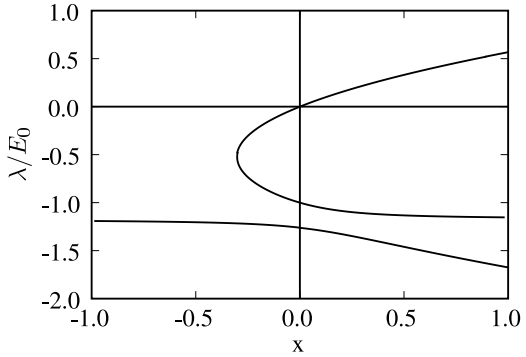

Figure 3.3: The light particle energy $\lambda(\boldsymbol{k})$ as a function of $x = \frac{\hbar^2 k^2}{2m^{k=0}_{\Gamma_6} E_0}$ for GaAs. A negative x corresponds to an evanescent state.

shows the dispersion of the light particles calculated for GaAs from eq. (3.16). Due to the approximations made the dispersion relations for all states considered are isotropic. Actually a noticeably band warping does exist in the valence band of typical semiconductors. This results from $\boldsymbol{k}\cdot\boldsymbol{p}$ interactions with remote bands. When considering the next higher conduction band within second order perturbation theory one obtains an exact expression for the two Γ_8 degenerate valence band states which have the form of warped spheres[36] and which reveal a reduced

mass even at the band edge:

$$E_{\Gamma_8}(\boldsymbol{k}) = Ak^2 \pm [B^2k^4 + C^2(k_x^2k_y^2 + k_y^2k_z^2 + k_z^2k_x^2)]^{\frac{1}{2}} \tag{3.22}$$

The parameters A, B and C are related to the momentum matrix element P and the energy gaps and are given in [36].

3.2.2. Envelope function description for heterostructures

Up to now we have only discussed the band-structure properties of bulk crystals. However to describe semiconductor heterostructures which are matter of this work, it is necessary to consider the effects of a varying potential which occurs when the crystal is made of a sequence of dissimilar materials but which crystallize in the same structure. Despite the fact that due to the power of modern computers band structure calculations using microscopic methods like the pseudopotential one are feasible even for unit cells containing up to millions of atoms, the so called envelope function approximation (EFA) still has some advantages due to its simplicity and versatility. Like the $\boldsymbol{k}\cdot\boldsymbol{p}$ theory for bulk semiconductors the envelope function description is a way to obtain analytical results for the electronic states in a heterostructure and provides an insight to the physical origin of the numerical results. Its validity is restricted to the vicinity of the high-symmetry points in the host Brillouin zone.

Heterostructures are classified according to the sign of the band offsets at the interfaces. A type-I heterostructure is given if the potential is confining in the same material for both electrons and holes, whereas in type-II only one type of carrier is spatially constricted (see Fig. 3.4). In

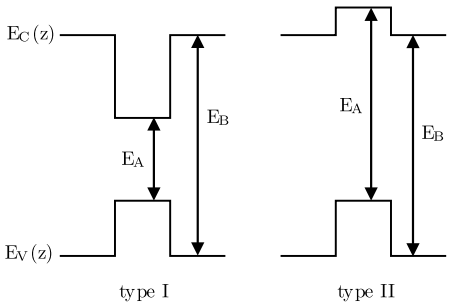

Figure 3.4: Conduction and valence band profiles motivating the classification of heterostructures made of two materials A and B with dissimilar band gaps.

the EFA the interfaces are considered to be ideally abrupt. This assumption is not unrealistic since modern technology allows for the fabrication of atomically flat interfaces which represent the physical limit. However, in some material systems an inevitable and uncontrolled interdiffusion between both materials might occur, which smoothes the interfaces. These effects are not covered by the standard EFA. In fact the EFA results resemble the solutions of the finite square quantum well, where the different effective masses in both materials and their energy

dependence is taken into account. The resulting heterostructure wavefunction $\Psi(\boldsymbol{r})$ is a sum of the products of rapidly varying functions $u(\boldsymbol{r})$ which are periodic with the crystal periodicity of each material and a slowly varying envelope function $\chi(\boldsymbol{r})$. At the interface the envelope function is required to change continuously differentiable. As the relevant electronic states involved in the construction of the heterostructure one are close to the band extrema of the respective material, it is sufficient to take into consideration only the Γ_6, Γ_7, Γ_8 edge states. In the following, we consider the case of heterointerfaces perpendicular to the crystal z direction which typically corresponds to the [001] growth direction of the semiconductor quantum well or superlattice. In addition to the empirical parameters in the bulk band structure calculation ($E_0^{A,B}$, $P^{A,B}$, $\Delta_0^{A,B}$), we need to know the band lineups of the A and B materials at the interfaces. Since the band gaps are known, a single band offset remains undetermined, say the valence band offset V_p. It is possible using microscopic *ab-initio* theories to predict V_p or to directly measure V_p with suitable experiments, like high pressure absorption or deep level transient spectroscopy. However, the uncertainty of both methods is large and this issue has been subject of many publications in the last two decades. I will not go into details of the solution procedure of the heterostructure Hamiltonian but briefly describe solutions for the heterostructure states parallel to the confinement direction. The heavy hole levels are the solutions of a Daniel-Duke Hamiltonian, whereas the light particles are obtained by solving a Kane-type Hamiltonian. The latter reduces to the former in the limit of large band gaps and spin-orbit coupling energies, i.e. when the band nonparabolicity vanishes.

Heavy hole states The Daniel-Duke model of a heterostructure is the simplest one and works well for the heavy hole levels at $\boldsymbol{k}_\perp = 0$. It assumes that the heterostructure envelope function is built from host quantum states which belong to a single parabolic band. This is true if the coupling to remote bands is neglected which also implies that the effective mass does not depend on energy. The eigenenergies ε_n result from the numerical solution of two implicit equations:

$$\tan\frac{k_A L}{2} = \xi^{-1}, \qquad \operatorname{cotan}\frac{k_A L}{2} = -\xi^{-1} \tag{3.23}$$

where

$$\xi = \frac{k_B}{\kappa_A}\frac{m_B^\star}{m_A^\star}, \qquad k_A^2 = \frac{2m_A^\star \varepsilon_n}{\hbar^2}, \qquad \kappa_B^2 = \frac{2m_B^\star(-V-\varepsilon_n)}{\hbar^2}, \tag{3.24}$$

Here L is the width of the quantum well, V the valence band offset, k_A and κ_B are the wave vectors in material A and B, respectively, and $\kappa_B = ik_B$ reflects the evanescent part of the envelope function. Eqs. (3.23-3.24) are identical to the solution of a one dimensional finite square well except that the masses are taken to be different in both materials. The symmetric and antisymmetric envelope functions $f^{\pm}(z)$ are defined piecewise and differentiable continuously at

the interfaces

	B	A	B
$f^+(z)$	$\exp(\kappa_B z)$	$\frac{\exp(-\kappa_A L/2)}{\cos k_A L/2}\cos k_A z$	$\exp(-\kappa_B z)$
$f^-(z)$	$\exp(\kappa_B z)$	$\frac{-\exp(-\kappa_A L/2)}{\sin k_A L/2}\sin k_A z$	$-\exp(-\kappa_B z)$

(3.25)

Light particle states The heterostructure eigenstates of the light particles are obtained like those of the heavy holes (3.23) but taking the nonparabolicity of the effective mass into account [37]:

$$\frac{m_0}{m_{\Gamma_6}} = 1+\frac{2P^2}{3m_0}\left[\frac{2}{\varepsilon_n+E_A}+\frac{1}{\varepsilon_n+E_A+\Delta_0^A}\right] \tag{3.26}$$

$$\frac{m_0}{m_{\Gamma_8^l}} = 1+\frac{4P^2}{3m_0}\frac{1}{\varepsilon_n+E_A}\left[1-\frac{\varepsilon_n}{2(\Delta_0^A-\varepsilon_n)}\right]. \tag{3.27}$$

Since the masses depend on energy as expected, numerical results for the eigenstates have to be calculated by iteration. We see from the denominator of the second term in Eq. (3.27) that the light hole mass will increase considerably if confinement pushes the states close to the spin-orbit coupling energy of the well material.

3.2.3. Effects of strain on the band structure

The displacement of atoms from their initial position induced by internal or external forces is described in terms of a displacement vector $\boldsymbol{u}(\boldsymbol{r}) = \boldsymbol{r}' - \boldsymbol{r}$, where the primed vector denotes the shifted position. The linking vector between two atoms is

$$\boldsymbol{d} = \boldsymbol{r}_a - \boldsymbol{r}_b \tag{3.28}$$

thus, it transforms under deformation as

$$\boldsymbol{d}' = \boldsymbol{r}_a' - \boldsymbol{r}_b' = (\boldsymbol{r}_a + \boldsymbol{u}(\boldsymbol{r}_a)) - (\boldsymbol{r}_b + \boldsymbol{u}(\boldsymbol{r}_b)) = \boldsymbol{d} + (\boldsymbol{u}(\boldsymbol{r}_a + \boldsymbol{d}) - \boldsymbol{u}(\boldsymbol{r}_a)). \tag{3.29}$$

If the deformations are considered to be infinitesimal $\boldsymbol{u}(\boldsymbol{r}_a + \boldsymbol{r})$ can be replaced by its first order Taylor expansion:

$$u_i(\boldsymbol{r}_a + \boldsymbol{r}) \approx \boldsymbol{u}(\boldsymbol{r}) + d_j \frac{\partial u_i}{r_j} \tag{3.30}$$

using the sum rule for repeated indices. Now Eq. (3.29) can be rewritten as

$$d_i' = d_i + d_j \frac{\partial u_i}{r_j}. \tag{3.31}$$

The second-rank tensor

$$d_{ij} = \frac{\partial u_i}{r_j} \tag{3.32}$$

is called the deformation tensor and can be decomposed into the sum of a symmetric tensor ε_{ij} and an antisymmetric one ω_{ij}.

$$\varepsilon_{ij} = \frac{1}{2}\left(\frac{\partial u_i}{r_j} + \frac{\partial u_j}{r_i}\right) \tag{3.33}$$

$$\omega_{ij} = \frac{1}{2}\left(\frac{\partial u_i}{r_j} - \frac{\partial u_j}{r_i}\right) \tag{3.34}$$

The latter describes a pure rotation of the crystal and therefore does not change the electronic properties, whereas the symmetric tensor ε_{ij} describes a strain induced in the crystal by the atomic displacements and is known as the strain tensor. It can be shown using group theory that in zinc-blende crystals ε_{ij} can be further decomposed into the sum of three linearly independent matrices $\mathbf{M}$ which represent the basis for every possible deformation

$$\mathbf{M}^{hyd.} = \frac{1}{3}\begin{bmatrix} \varepsilon_{11}+\varepsilon_{22}+\varepsilon_{33} & 0 & 0 \\ 0 & \varepsilon_{11}+\varepsilon_{22}+\varepsilon_{33} & 0 \\ 0 & 0 & \varepsilon_{11}+\varepsilon_{22}+\varepsilon_{33} \end{bmatrix}, \tag{3.35a}$$

$$\mathbf{M}^{[001]} = \frac{1}{3}\begin{bmatrix} 2\varepsilon_{11}-(\varepsilon_{22}+\varepsilon_{33}) & 0 & 0 \\ 0 & 2\varepsilon_{22}-(\varepsilon_{33}+\varepsilon_{11}) & 0 \\ 0 & 0 & 2\varepsilon_{33}-(\varepsilon_{11}+\varepsilon_{22}) \end{bmatrix}, \tag{3.35b}$$

$$\mathbf{M}^{[111]} = \begin{bmatrix} 0 & \varepsilon_{12} & \varepsilon_{13} \\ \varepsilon_{12} & 0 & \varepsilon_{23} \\ \varepsilon_{13} & \varepsilon_{23} & 0 \end{bmatrix}. \tag{3.35c}$$

The matrix $\mathbf{M}^{hyd.}$ has a nonzero trace and from the definition of the strain tensor components in Eq. (3.33) follows that its trace is equal to the fractional volume change $\Delta V/V$ associated with a certain strain pattern. The traceless strain matrices $\mathbf{M}^{[001]}$ and $\mathbf{M}^{[111]}$ describe a shear of the crystal produced by uniaxial stress in [001] and [111] direction respectively. As a consequence, three deformation potentials are required to describe the effect of a general strain on a band extremum.

For the description of the effect of strain on the electronic properties of semiconductors Bardeen and Shockley introduced the concept of the deformation potential [38]. These deformation potentials were introduced in the context of the electron-phonon coupling between long-wavelength ($k = 0$) acoustic phonons and the valence electrons but their definition has general validity. A pure hydrostatic strain which is created e.g. in high pressure experiments with the DAC, which are subject of this work, shifts the electronic states but does not split them. The linear components of these shifts are represented by the volume deformation potential a_i in (eV) defined as

$$a_i = \frac{\mathrm{d}E_i}{\mathrm{d}\ln V} = \frac{\Delta E_i}{\mathrm{tr}\,\varepsilon}, \tag{3.36}$$

where E_i denotes the energy of state i and V the volume of the crystal. Instead of the hydrostatic deformation potential one often finds in the literature the corresponding pressure coefficient $\mathrm{d}E_i/\mathrm{dP}$ which is related to the deformation potential through the bulk modulus B

$$\frac{\mathrm{d}E_i}{\mathrm{d}p}B = a_i\,. \tag{3.37}$$

Absolute values for a_i are difficult to obtain experimentally as usually only the pressure de-

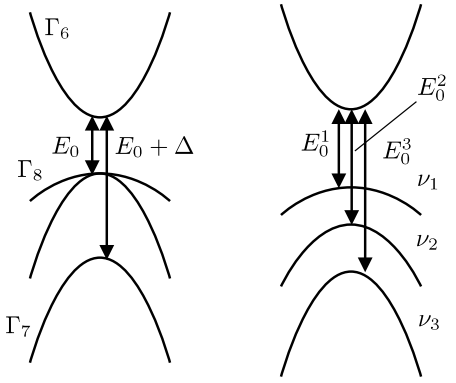

Figure 3.5: Schematic valence and conduction bands of a III-V semiconductor for unstrained (left) and strained (right) crystals.

pendence of gaps are measured, which yields only the relative deformation potential between the bands involved. The pressure coefficient of the direct band gap at the Γ point of III-V compounds is in the order of +100 meV/GPa. For the indirect band gap $X-\Gamma$ it is about an order of magnitude smaller and negative and about +50 meV/GPa for the indirect $L-\Gamma$ gap. Thus, at some pressure the X valley will become the lowest conduction band. This is called the *direct-to-indirect crossover*. For e.g. bulk GaAs it occurs at 4 GPa.

A strain that has a uniaxial component will split those states whose symmetry is reduced by the deformation. This is not the case for the lowest conduction band which has Γ_1 symmetry but holds for the valence bands and the X and L conduction band minima. For the $J = 3/2$ valence states Pikus and Bir have derived a hole-strain interaction Hamiltonian within the $\boldsymbol{k}\cdot\boldsymbol{p}$ framework [39] for a general strain

$$\begin{aligned} H_\varepsilon &= a\,\mathrm{tr}\,\varepsilon + 3b\left[(L_x^2 - L^2/3)\varepsilon_{xx} + c.p.\right] && (3.38)\\ &\quad + \frac{6d}{\sqrt{3}}\left[\frac{1}{2}(L_xL_y + L_yL_x)\varepsilon_{xy} + c.p.\right], && (3.39)\end{aligned}$$

where $\boldsymbol{L}$ is the angular momentum operator and $c.p.$ stands for cyclic permutations. The deformation potentials b and d determine the splitting of the four-fold degenerate valence bands at Γ under [100] and [111] uniaxial stress, respectively. Figure 3.5 shows schematically how the Γ_8 and Γ_7 valence bands evolve into three bands denoted ν_1, ν_2 and ν_3 under uniaxial stress in e.g. [001] direction. Solving the strain Hamiltonian yields the following shifts of the ν_i valence band

with respect to the weighted average for stress or strain in [001] direction [40]

$$\Delta E_{v_2} = -\frac{1}{3}\Delta_0 + \delta E_H + \frac{1}{2}\delta E_X \tag{3.40a}$$

$$\Delta E_{v_1} = \frac{1}{6}\Delta_0 + \delta E_H - \frac{1}{4}E_X - \frac{1}{2}\sqrt{\Delta_0^2 + \Delta_0\delta E_X + \frac{9}{4}(\delta E_X)^2} \tag{3.40b}$$

$$\Delta E_{v_3} = \frac{1}{6}\Delta_0 + \delta E_H - \frac{1}{4}E_X + \frac{1}{2}\sqrt{\Delta_0^2 + \Delta_0\delta E_X + \frac{9}{4}(\delta E_X)^2} \tag{3.40c}$$

$$\tag{3.40d}$$

The indices H and X denote the hydrostatic and shear (either [001] or [111]) component of the strain, respectively. The band v_2 corresponds to $|3/2,\pm 3/2\rangle$ (heavy holes), whereas v_1 and v_3 are strain-induced linear combinations of $|3/2,\pm 1/2\rangle$ and $|1/2,\pm 1/2\rangle$ [41]. However, they are commonly still called by theirs unstrained denotations as light and split-off bands. For a two-dimensional strain in the $\{001\}$ plane the energies are given by

$$\delta E_H = a\,\mathrm{tr}\,\varepsilon = 2a\frac{C_{11}-C_{12}}{C_{11}}\varepsilon_{xx} \tag{3.41a}$$

$$\delta E_X = b\varepsilon_{[001]} = -2b\frac{C_{11}+2C_{12}}{C_{11}}\varepsilon_{xx}. \tag{3.41b}$$

The components of the strain tensor ε are related through the elastic constants and the boundary conditions. This will be discussed further in section 3.3.1.

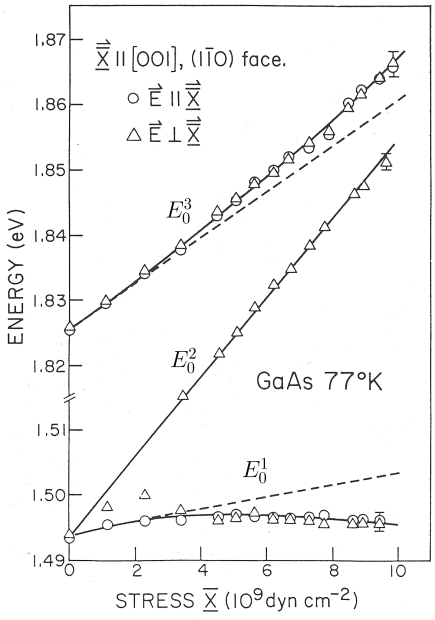

Figure 3.6: The energies of the E_0^1, E_0^2 and E_0^3 transitions in bulk GaAs at 77 K for uniaxial stress along the [001] direction (from ref[42]).

For most III-V semiconductors the shear deformation potentials b and d are negative. The valence band volume deformation potential a_v is small compared to that of the band gap, which

means that most of the pressure dependence of the band gap is due to the change in the conduction band. A theoretical study of the band gap pressure coefficients carried out for many different semiconductors yields that both a_v and a_c are mostly negative [4], however, there is no experimental data about the absolute deformation potentials available. Instead of considering the bands separately it is safer to use the band gap deformation potential $a = a_c + a_v$ in Eqs. (3.41a-3.41b) thus obtaining the shifts of the band gaps from Eqs. (3.40a-3.40c).

When evaluating Eqs. (3.40a-3.40c) we note that in the case of a biaxial tensile strain in the x-y–plane (ε_{xx}), which corresponds to uniaxial compressive stress in the [001] direction, the E_{v_1} band will be the top valence band. This is nicely confirmed by the experimental results of absorption experiments under [001] stress of bulk GaAs shown in Fig. 3.6. The solid lines are fits of the experimental data with Eqs. (3.40a-3.40c). The heterostructures studied in this work, however, contain embedded material which is mostly compressively strained in the x-y–plane, as this is the prerequisite for the self organized growth of quantum dots. We therefore expect that E_{v_2} band will become the highest valence band at the Γ point.

Similar expressions as those of Eqs.(3.35a-3.35c) for the pressure dependence of the valence bands can be obtained for the X-valley of the conduction band. A shear strain in [001] direction lifts the six-fold degeneracy and splits the X-states into a [001] doublet (X_Z) and a [100] and [010] quartet (X_{XY}). The hydrostatic component further shifts the weighted average [43, 44]

$$\Delta E_X^Z = \delta E_H + \frac{2}{3}\delta E_X \tag{3.42a}$$

$$\Delta E_X^{XY} = \delta E_H - \frac{1}{3}\delta E_X. \tag{3.42b}$$

The energy shifts are calculated from the strain using the deformation potentials for the conduction band X-valley Ξ_u and Ξ_d

$$\delta E_H = (\Xi_d + \frac{1}{3}\Xi_u)\mathrm{tr}\epsilon \tag{3.43a}$$

$$\delta E_X = \frac{1}{2}\Xi_u \varepsilon_{[001]}. \tag{3.43b}$$

3.2.4. Summary

From the previous sections we can summarize the different effects on the energy of a confined state induced by strain or external pressure. The largest contribution is that of the strain dependence of the band edges. Second order effects are the energy dependence of the effective mass, which can be described within the effective mass approximation and the pressure dependence of the conduction and valence band offsets, which is considered in the framework of the envelope function approximation. The reduction of the potential width as the interatomic distance decreases upon external pressure is only about 0.6 % at a pressure of 1 GPa, and can be neglected.

In undoped semiconductors the emission from transitions between confined states is strongly influenced by the effect of exciton formation, i.e. of a photoexcited electron-hole pair coupled by Coulomb interaction. The energy spectrum of an exciton resembles that of a hydrogen atom obtained by using a reduced mass μ which incorporates the effective electron and hole masses, and the static dielectric constant of the host material. The Rydberg energy has shown to vary in proportion to the reduced effective mass μ in III-V semiconductors, that is, to the band gap[45], but only by some meV in the pressure range up to 10 GPa. For phonon-assisted processes like the indirect Γ-X transition, the phonons' pressure dependence is modifiying the measured pressure coefficients of the electronic states. These corrections, however, are less than 1 meV/GPa[46].

3.3. Strain modelling in heterostructures

Heterostructures consisting of different materials exhibit strain if the lattice constants do not match. A thin film grown epitaxially on a thick substrate has to adjust its lattice constant parallel to the interface to that of the substrate. In the perpendicular direction the lattice is allowed to expand or shrink in order to minimize the strain energy. The situation is getting more complicated when looking at the three dimensional structure of a quantum dot and spatially resolved calculations have to be carried out to get information about the local strain fields.

3.3.1. Continuum model

The linear elastic theory is based on the assumption that the strain in a solid is proportional to the applied load. This is described by the generalized Hooke law of the proportionality of the stress and strain

$$\sigma_{kl} = C_{klmn}\varepsilon_{nm}, \tag{3.44}$$

where σ and ε are third rank tensors called stress and strain tensors. Due to its symmetry only 21 of the 81 components of the compliance matrix C_{klmn}, which link external stress to internal strain are non zero. In a cubic face-centered crystal structure like the zinc-blende one, this number further reduces to three nonzero components usually denoted (in matrix notation) as C_{11}, C_{12} and C_{44}. Like this, eq. (3.44) can be written in a contracted notation in which the strain

and stress tensors are represented by a six-component array:

$$\begin{pmatrix} \sigma_1 \\ \sigma_2 \\ \sigma_3 \\ \sigma_4 \\ \sigma_5 \\ \sigma_6 \end{pmatrix} \begin{pmatrix} C_{11} & C_{12} & C_{12} & 0 & 0 & 0 \\ C_{12} & C_{11} & C_{12} & 0 & 0 & 0 \\ C_{12} & C_{12} & C_{11} & 0 & 0 & 0 \\ 0 & 0 & 0 & C_{44} & 0 & 0 \\ 0 & 0 & 0 & 0 & C_{44} & 0 \\ 0 & 0 & 0 & 0 & 0 & C_{44} \end{pmatrix} \begin{pmatrix} \varepsilon_1 \\ \varepsilon_2 \\ \varepsilon_3 \\ \varepsilon_4 \\ \varepsilon_5 \\ \varepsilon_6 \end{pmatrix}, \tag{3.45}$$

where the stress and strain vectors are related to their tensorial form like:

$$\epsilon = \begin{pmatrix} \varepsilon_1 & \varepsilon_6/2 & \varepsilon_5/2 \\ \varepsilon_6/2 & \varepsilon_2 & \varepsilon_4/2 \\ \varepsilon_5/2 & \varepsilon_4/2 & \varepsilon_3 \end{pmatrix}. \tag{3.46}$$

The diagonal elements of the strain tensor are the strain components along the principal directions, whereas shear strain is determined by the off-diagonal elements. Its trace corresponds to the hydrostatic strain, i.e. the volume deformation:

$$\frac{\Delta V}{V} = \mathrm{tr}(\epsilon). \tag{3.47}$$

From Eq. (3.44) we can calculate the strain components in a material which is induced either by external forces, which is the case in high pressure experiments, or by the lattice constant mismatch when growing a heterostructure consisting of two different materials. A thin film which is grown epitaxially on a thick substrate will be stretched or compressed along the interface, while it is free to extend or contract along the perpendicular dimension. In that case, the stress is given by

$$\begin{aligned} \sigma_{xx} = \sigma_{yy} = \sigma, \qquad \sigma_{zz} = 0 \\ \sigma_{ij} = 0, \qquad i \neq j, \end{aligned} \tag{3.48}$$

implying the following relations for the strain components

$$\begin{aligned} \varepsilon_{xx} = \varepsilon_{yy}, \qquad \varepsilon_{zz} = -\lambda \varepsilon_{xx} \\ \varepsilon_{ij} = 0, \qquad i \neq j, \end{aligned} \tag{3.49}$$

where

$$\lambda = -\frac{\varepsilon_{zz}}{\varepsilon_{xx}} \tag{3.50}$$

depends on the crystallographic orientation of the strained layer. The in-plane strain is given by the lattice mismatch between film and substrate

$$\varepsilon_{xx} = \frac{a_s - a_{film}}{a_{film}}, \tag{3.51}$$

where a_{film} and a_s are the lattice constants of the substrate and the thin film, respectively. A negative value of (3.51) represents compressive strain, a positive value tensile strain. The coefficient λ can be calculated by applying the boundary conditions (3.48) on Hooke law (3.44). For the biaxial strain along [001] direction considered here it yields

$$\lambda_{001} = \frac{2C_{12}}{C_{11}}. \tag{3.52}$$

Like this we obtain the following expressions for the biaxial [001] and hydrostatic strain components existent in the strained layer

$$\begin{aligned} \varepsilon_{[001]} &= 2\varepsilon_{zz} - (\varepsilon_{xx} + \varepsilon_{yy}) = 2(-\lambda\varepsilon_{xx} - \varepsilon_{xx}) = -(1+\lambda)\varepsilon_{xx} \\ &= -2\frac{C_{11}+2C_{12}}{C_{11}}\varepsilon_{xx} \qquad (3.53a) \\ \varepsilon_{hyd} &= \varepsilon_{xx} + \varepsilon_{yy} + \varepsilon_{zz} = 2\varepsilon_{xx} - \lambda\varepsilon_{xx} = (2-\lambda)\varepsilon_{xx} \\ &= 2\frac{C_{11}-C_{12}}{C_{11}}\varepsilon_{xx} \qquad (3.53b) \end{aligned}$$

We notice that the strain in a biaxially strained layer always includes a hydrostatic component. As demonstrated in section 3.2.3 a general strain pattern can be decomposed into a purely axial and a purely volume component. Using the results from Eqs. (3.53a) and (3.53b) we get

$$3\epsilon = \varepsilon_{hyd} - \varepsilon_{[001]}. \tag{3.54}$$

In order to calculate the equilibrium positions of the atoms of a more complicated structure like the typical pyramidal quantum dot using continuum elasticity theory, one has to employ a discretization method based on finite elements or finite differences to minimize the total elastic energy

$$E_{tot} = \frac{1}{2}\sum_{ijkl} C_{ijkl}\varepsilon_{ij}\varepsilon_{kl} \tag{3.55}$$

3.3.2. Atomistic description

There has been much work describing the elastic properties by means of an atomistic model, among them, the first was proposed by Born [47]. A widely used description for diamond-type crystals is the valence force field (VFF) in the Keating [48] form, within which the atomic bonds are represented by bond-stretching and bond-bending interactions between next neighbor atoms (see Fig. 3.7). Martin [49] extended the model for the application to zinc-blende crystals by including a coulomb interaction term which accounts for the ionicity of the crystal. However, these corrections are small for III-V compounds and are usually neglected, though they might be important for II-VI semiconductors. The total elastic energy in the VFF model is calculated

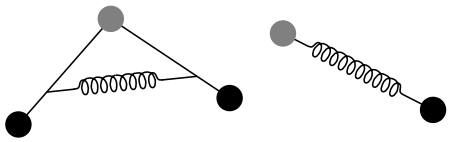

Figure 3.7: The two types of interactions used in the VFF. Left: bond bending, Right: bond stretching.

according to

$$\begin{aligned} E_{tot} &= \sum_i \sum_j^n \frac{3}{8}\alpha_{ij}\Delta d_{ij}^2 \\ &+ \sum_i \sum_{j,k<j}^{nm} \frac{3\beta_{ijk}}{8d_{ij}^0 d_{ik}^0}\left[(\mathbf{R}_i-\mathbf{R}_j)\times(\mathbf{R}_k-\mathbf{R}_i)-\cos\theta_0 d_{ij}^0 d_{ik}^0\right]^2, \end{aligned} \tag{3.56}$$

where $\Delta d_{ij} = \left[(\mathbf{R}_i-\mathbf{R}_j)^2-(d_{ij}^0)^2\right]/d_{ij}^0$, R_i are the coordinates of the atoms, d_{ij} the unrelaxed bond length, $\theta = \arccos(-1/3)$ the ideal tetrahedral angle, α_{ij} and β_{ijk} the force constants for bond-stretching and bond-bending interaction, respectively. The first term sums over all atoms i and its four first neighbors; the second term sums also over all atoms i and their distinct pairs of next neighbors j and k forming the bond angle. We note that only two force constants are necessary. Across a heterointerface the bond bending interaction parameter β is taken as the algebraic average of both materials. The force constants correspond to the elastic constants in a pure zinc-blende structure calculated in the following way

$$\begin{aligned} C_{11} &= \frac{\alpha+3\beta}{a} \\ C_{12} &= \frac{\alpha-\beta}{a} \\ C_{44} &= \frac{4\alpha\beta}{a(\alpha+\beta)}, \end{aligned} \tag{3.57}$$

where $a = 4r_0/\sqrt{3}$ is the lattice constant and r_0 is the interatomic bond length. It is not possible, though, to match the three elastic constants with only two free parameters and usually C_{44} is neglected. Thus, equations (3.57) imply a relation between the force constants

$$\frac{2C_{44}(C_{11}+C_{12})}{(C_{11}-C_{12})(C_{11}+3C_{12})} = 1, \tag{3.58}$$

which holds quite well for nonpolar crystals like silicon and germanium but deviates from unity for any ionic III-V or II-VI compound. Martin [49] has introduced a Coulomb term to account for the different atoms on either sublattice. However, using Matrin's own values, the contribution of this extension to C_{44} is only about 2 %, which is the same order as the experimental errors on C_{44}[50].

The equilibrium atomic positions are found by minimizing the total strain energy (3.56) using for example a conjugate gradient method. The local strain is determined by looking at the

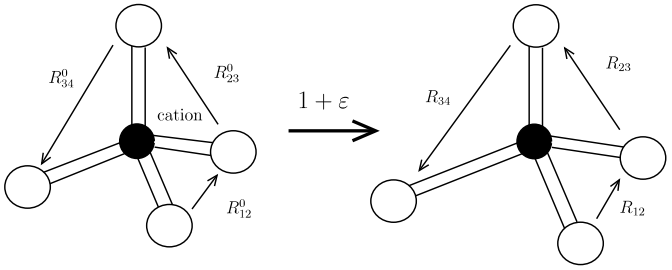

Figure 3.8: The local strain is determined from the distortion of an elementary tetrahedron.

distortion of an elementary atomic tetrahedron (see Fig. 3.8). The application of the strain tensor ϵ on the unrelaxed coordinates R_0 yields the distorted coordinates R

$$\mathbf{R} = \begin{pmatrix} 1+\varepsilon_{xx} & \varepsilon_{yx} & \varepsilon_{zx} \\ \varepsilon_{xy} & 1+\varepsilon_{yy} & \varepsilon_{zy} \\ \varepsilon_{xz} & \varepsilon_{yz} & 1+\varepsilon_{zz} \end{pmatrix} \mathbf{R_0}, \tag{3.59}$$

with

$$\mathbf{R} = \begin{pmatrix} R_{12,x} & R_{23,x} & R_{13,x} \\ R_{12,y} & R_{23,y} & R_{13,y} \\ R_{12,z} & R_{23,z} & R_{13,z} \end{pmatrix}$$

The application of this simple model for the calculation of the strain in lattice mismatched heterostructures has been demonstrated by many authors[51–53]. However, considering the large strain existent in e.g. InAs/GaAs superlattices ($\varepsilon_{xx} \approx 6.9\,\%$) we are almost certainly leaving the validity of linear elastic theory. For any stress which is not infinitesimal in the sense of elasticity theory the compressibility of a material depends on the pressure, i.e. a material gets stiffer the larger the compression. This can be taken into account by introducing pressure dependent elastic constants. Murnaghan proposed a linear dependence on pressure of the bulk modulus [54]

$$B(\mathrm{P}) = B_0 + B'\mathrm{P}. \tag{3.60}$$

For III-V semiconducors B' is about 5–10 % of B_0 and therefore cannot be neglected when considering the effects of high hydrostatic pressure nor internal pressures in strained heterostructures. In the VFF this dependence can be incorporated by modifying the bond stretching potential such that it fits the bulk modulus at any pressure. In Ref. [55] the harmonic stretching potential was extended by a cubic term which only makes sense for compression, of course. Thus, in Eq. (3.56) the first term is replaced by

$$\sum_i \sum_j^{nm} \frac{3}{8} \left[\alpha_{ij}^{(1)} \Delta d_{ij}^2 + \alpha_{ij}^{(2)} \Delta d_{ij}^3 \right]. \tag{3.61}$$

In that work the problem of the undetermined relationship between the atomic force constants and the elastic modulus has been addressed too. By adding a third term which is a combined

stretching-bending interaction to the elastic energy the authors claim to be able to correctly map both models onto each other. However, the correction is small compared to the large strain generated in pressure experiments and it will be ignored here.

4. Results and Discussion

In this chapter I will present the results from high-pressure experiments on InAs/GaAs and InP/GaP self-organized quantum dots. The former material system has attracted the most interest, being the first for which the formation of quantum dots was reported in [18]. After that discovery, the self-organized growth method has been applied to many other strained material systems, including element semiconductors and binary and ternary systems of the III-V and II-VI group. The InP/GaP system is one of the most recent and is especially interesting for opto electronical devices in the visible red range, whereas the InAs/GaAs system is aimed to operate in the wavelength range which is interesting for optical fiber-based communication around 1.3 μm.

In addition I will present the results from strain simulations using an atomistic valence force field, taken out to show, that the special character of the strain field plays an essential role in the pressure dependence of the quantum dot emission.

4.1. InAs/GaAs quantum dots

In this section I will present the results of PL experiments on self-organized InAs/GaAs quantum dots under high hydrostatic pressure. Low temperatures spectra exhibit a multimodal distribution of the ground-state transition energy. Calculations based on an eight band $\boldsymbol{k} \cdot \boldsymbol{p}$ model and a structural analysis demonstrate that this distribution originates from a discrete, stepwise variation of the size of the QDs [29]. The InAs QDs have the shape of a truncated pyramid, differing in height and base length in multiples of a monolayer. The observation of clearly separated peaks implies that the upper and lower interfaces of the QDs are well-defined and that indium segregation is small. Eight different sub-ensembles can be identified at low temperatures and ambient pressure each with a full width at half maximum of about 30 meV. Details of the growth procedure are described in Ref. [29]. This sample is especially interesting for high pressure experiments since it allows for a direct comparison of the pressure dependence of electronic states in quantum dots of different sizes but in exactly the same environment.

4.1.1. Low temperature photoluminescence

Figure 4.1 shows a low temperature photoluminescence spectrum recorded with a low excitation power of 10 W/cm^2 to ensure that emission from excited states is not activated. The emission band associated with ground state recombination in the QDs spans from 1.05 to 1.35 eV at ambient pressure. According to Ref. [29], the eight peaks relate to quantum dots of 2–8 monolayers height. They can be fitted well with Gaussians, yielding a FWHM of about 30 meV for each peak and an increasing peak separation with decreasing QD height. Centered at 1.49 eV a sharp feature is observed, which originates from the recombination of carriers confined in the wetting layer. In addition, there are two small peaks on each side of the WL one, the lower one separated by approximately one InAs LO-phonon energy (?? meV), therefore attributed to the LO-phonon replica. The weak peak on the high energy side at 1.512 eV is due to the free exciton recombination of bulk GaAs.

With rising pressure (see Fig. 4.2) all observed peaks shift to higher energies, which is a clear indication that the observed transitions are direct in $\boldsymbol{k}$-space. The sharp line at about 1.79 meV, appearing in all spectra corresponds to the ruby luminescence. At 3.1 GPa a ninth peak appears on the high energy side of the QD emission band. Its energy and shape suggest that it is due to recombination within the next smaller ensemble of dots, i.e a dot of only one monlayer height. As I will show in the next chapter, the conduction band offset (CBO) significantly increases with rising pressure. A confined state which is energetically very close to the top potential edge, will lower its energy with respect to the potential edge as the CBO increases. Thus, a state with a very

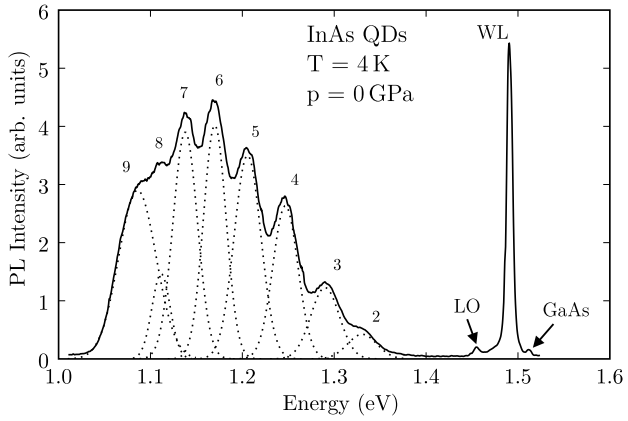

Figure 4.1: Photoluminescence spectrum of the InAs multimodal QD sample taken at 4 K. The numbers indicate the height of the QDs in monolayers.

small localization energy at ambient pressure would become confined, as the pressure increases. Therefore, with increasing pressure such electrons would be finally able to recombine with the holes. At 6.2 GPa the width of the whole QD emission band has reduced considerably. The

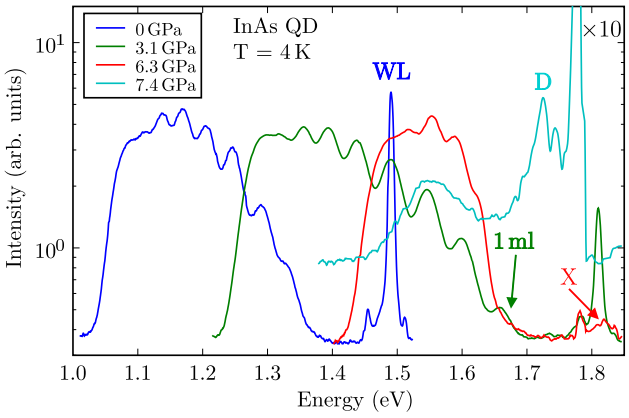

Figure 4.2: Photoluminescence spectra of the InAs multimodal QD sample taken at 4 K for four different pressures.

sharp wetting layer peak and the upper four of nine peaks related to the QDs have disappeared. A shoulder on the high energy tail of peak five corresponds to the onset of the sixth line. A new feature appears at about the WL energy, denoted as R, which is very weak and broader than the WL peak. These observations indicate, that a crossing of the Γ states with an X-valley related state (either in the QDs or in the GaAs matrix) occurs above 1.7 eV. I will discuss this in detail below. At 7.4 GPa the overall QD luminescence is almost completely quenched, the intensity dropped by a factor of 30 and a set of peaks, labelled D emerges, which is attributed to defects created by pressure induced dislocations. The remaining signal from the QDs is centered at about 1.55 eV and slowly shifts to lower energies with increasing pressure.

Figure 4.3 displays spectra recorded while releasing the pressure after having reached a final

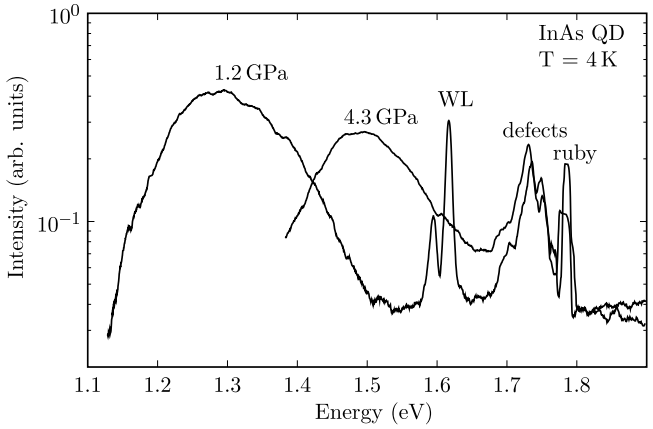

Figure 4.3: Photoluminescence spectra of the InAs multimodal QD sample taken at 4 K while releasing the pressure after having reached a maximum pressure of about 8 GPa.

pressure at 4 K of about 8 GPa. Obviously the sample does not completely recover from the applied pressure. The multimodal distribution of the QD ground state emission energy with its characteristic distinguishable subensembles has been smeared out. The overall intensity dropped by a factor of ten and the peaks, that were attributed to defect induced emission, are strong and remain visible even at ambient pressure.

The pressure dependence of all observed peaks is summarized in Fig. 4.4. The solid black lines depict the pressure dependence of the direct $\Gamma - \Gamma$ and indirect $X - \Gamma$ band gap of bulk GaAs taken from literature. All QD ground state transitions shift to higher energies with increasing pressure, slightly diverging, i.e. the peak separation increases with pressure. At 1.1 GPa the PL from the ninth subensemble of dots appears. The WL peak closely follows the band gap of GaAs, separated by 20 meV. At about 4 GPa the line from bulk GaAs is quenched abruptly, the fingerprint of the $\Gamma - X$ crossover. This is followed by the successive quenching of the higher energy QD lines, when the pressure is further increased. At some pressure steps it is possible to observe that while loosing its intensity due to the occurrence of crossover, the highest energy peak departs from the rising trend of the direct transition to follow that of a $X - \Gamma$ indirect one. Nevertheless, the weak signal is masked by that of its next lower-energy neighbor, so that it is not possible to further trace its pressure dependence. The peaks denoted R are attributed to the indirect transition in $\boldsymbol{k}$-space between the X conduction band and the valence band of GaAs in the nearest vicinity of the QD. Both bands are split due to the increasing tensile biaxial strain near the quantum dot, so that the effective band-gap is *locally* lowered with respect to that of bulk GaAs. This is further confirmed by the strain calculations, as will be shown in the next chapter. The existence of a bound X_Z state at the interface between the quantum dot and the barrier material has also been demonstrated for very small InP QDs embedded in GaP, GaP being an indirect semiconductor at ambient pressure [56]. The quenching of the quantum dot

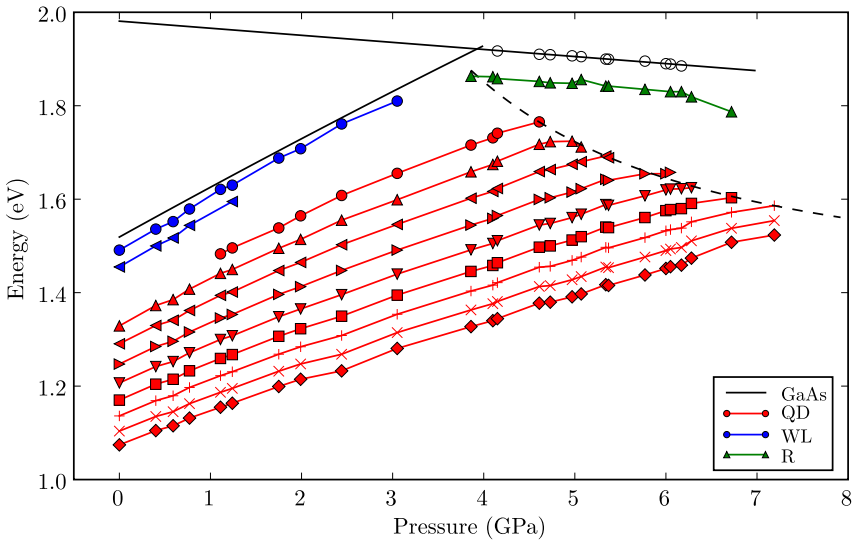

Figure 4.4: Pressure dependence of the energy position of the observed PL features. The red symbols correspond to recombination within the QDs, the blue symbols correspond to processes involving WL states. The line denoted R is due to recombination between the GaAs X-valley and the Γ valence band edge.

confined states occurs, when they cross the nearby X_Z conduction band state of GaAs, shown in figure 4.5. The situaation shown is that just after the crossover, when the emission from direct transition denoted 1 is quenched and the transition 2 if favoured, although it is very weak, as it occurs indirect in both real and reciprocal space. Additionally, in this sample, the transition is hardly seen, because it is masked by the emission from the next larger subensemble of dots. This crossover behavior has also been reported in Ref. [57] for InAs/GaAs quantum dots which

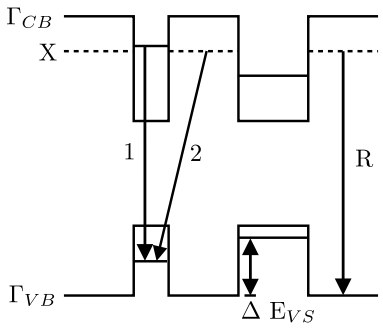

Figure 4.5: Schematic diagram of the conduction and valence band profile of the QD structure indicating the transitions which are relevant at the Γ=X crossover. (1) and (2) mark the QD related transitions before and after the crossover.

emit at 1.25 eV at ambient pressure. In that work, transitions above the crossover could be observed up to 7 GPa. A line shape and excitation power dependence analysis revealed that the

transitions beyond the crossover involve confined hole states of the dots and X-valley conduction band states. A crossing with the X-band of InAs is not expected at these energies since the Γ-X gap energy (2.28 eV) is much larger than that of GaAs (1.98 eV). Thus, from figure 4.5, we can see that the difference between the R energy and the QD energy at the crossover readily yields the valence *state* offset (E_{VS}), which is equal to the valence band offset reduced by the hole confinement energy.

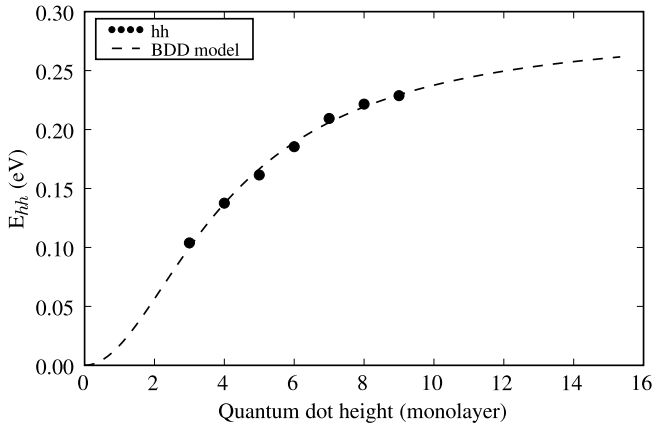

Figure 4.6: Energy of the InAs QD heavy hole states as a function of the dot height measured from the GaAs valence band edge.

Figure 4.6 shows the hole energies obtained by subtracting the crossover energies for each QD subensemble (indicated by the dashed line in Fig. 4.4) from the R-energies, as a function of the quantum dot height expressed in monolayers. The top valence band is a heavy hole state, therefore the effective mass is considered to be constant to first order and the confinement energy can be fitted using the Daniel-Duke model (Eq. (3.23)) with two free parameters: The valence band offset and an effective potential width. The latter accounts for the fact that we are treating the quantum potential as one-dimensional with a potential width equal to the height of the quantum dot in entire monolayers. Thus we are neglecting the confinement in the xy-plane and we are of course not able to include deviations from the square well shape of the potential. The fit yields a valence band offset of 290 meV and an effective width of 3.3 $\AA$, being significantly smaller than that of bulk InAs (6.05 $\AA$), which is very reasonable considering the above said. The agreement with the experimental data is very good. It shows nicely how the confinement energy for the holes saturates with increasing potential width, reaching the pure value of the valence band offset as limit.

Pressure coefficients The pressure coefficients of the direct QD transitions are obtained by fitting the data points using a quadratic function

$$E_\Gamma(p) = E_0 + a\mathrm{P} + b\mathrm{P}^2, \tag{4.1}$$

where a and b are the linear and quadratic pressure coefficients, respectively. The pressure coefficients of all QD related transitions are summarized in Fig. 4.7. The variation of the pressure coefficients with the emission energy is strikingly large. The values for the linear (quadratic) coefficient range from about 65 meV/GPa (-1 meV/GPa^2) for the largest dots to 110 meV/GPa (-5 meV/GPa^2) for the smallest ones. This spans the complete range of measured pressure coefficients for self-assembled InAs/GaAs quantum dots compiled and reported in Ref. [58]. Furthermore, the linear pressure coefficients measured here are mostly much smaller than those of bulk GaAs (117 meV/GPa) and InAs (≈100 meV/GPa) [3], whereas the sublinearity of the pressure dependence of all QDs emission given by the b coefficient is comparable to that of the bulk semiconductors. It has been shown that the sublinearity vanishes, if the energy of the $\Gamma - \Gamma$ transition is expressed in terms of the density and not the pressure [59]. Unfortunatelly, I have no access to the density of the embedded material, so this cannot be confirmed. For this purpose, a simultaneous measurement of the transition energy and the equation of state by X-ray diffraction would be necessary. Nevertheless, by using the results from the strain calculations in the next section together with band structure calculations within the EFA I will be able to explain this large spread of pressure coefficients observed for this special system of self-assembled dots, which differ from each other in size by single monolayers.

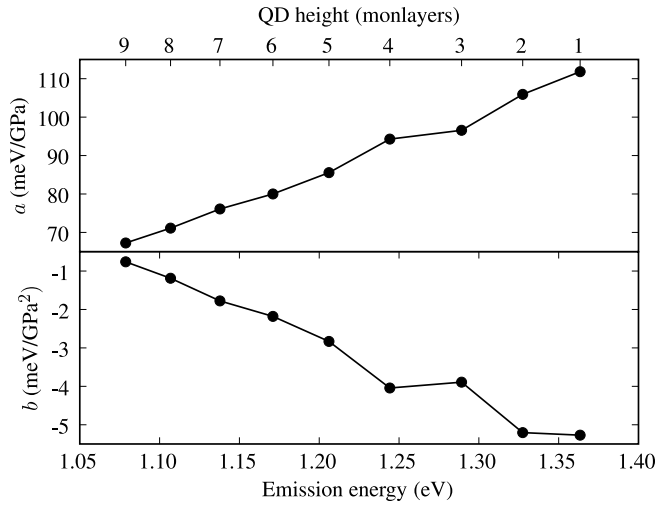

Figure 4.7: Linear (top) and quadratic (bottom) pressure coefficients a and b of the observed QD emissions as a function of the emission energy.

4.1.2. Strain simulations

The VFF presented in section 3.3.2 has been frequently used for the calculation of strained heterostructures and specially for quantum dots [51, 52, 55, 60, 61] as input for electronic or vibrational band structure calculations. As pointed out before, the extension of the VFF (in the following called XVFF) made to account for the pressure dependence of the bulk modulus

is already important when dealing with strongly strained heterostructures to correctly describe the internal strain as well as the one induced by the external pressure. It has often been suggested [58, 62, 63] that the application of the XVFF model in band structure calculations will eventually reproduce the variation of the pressure coefficients of InAs quantum dots observed experimentally. And in fact, Luo et al. [60] recently reported results from empirical pseudopotential calculations for many different dot geometries and found an almost linear dependence between the emission energy, which is a function of the dot size, and the pressure coefficients. Those are, however, extremely heavy numerical calculations, where the physical origin of the observed effects is very difficult to trace back. I will show in the following that it is possible to explain qualitatively the variation of the pressure coefficients simply by using VFF-strain calculations together with bulk deformation potentials and considering quantum confinement within the EFA. In particular, I will show that the XVFF is necessary to reproduce the low values of the pressure coefficients observed experimentally (about 60 meV/GPa).

Strain field under hydrostatic pressure

The super cell used for the VFF calculations is a cube with an edge 55 lattice constants of GaAs in size, i.e. about 310 $\AA$, thus containing more than 1.3 million atoms. The shape of the modelled quantum dots is that of a truncated pyramid to comply with the shape determined by structural analysis in Ref. [29]. Four different dot sizes have been considered, the smallest(largest) of them having a base length of about 12(17) nm and a height of 2(8) monolayers on top of the wetting layer. Since the geometry of the dots is almost cubic we have neglected the effects of [111] biaxial (shear) strain and only consider hydrostatic and [001] biaxial strain. Figure 4.8 shows the strain in a xz-plane, crossing the center of a 8 monolayer high quantum dot. The upper and lower pictures show the hydrostatic and [001] biaxial strain. The input data for the graphs is the same on the left and right side but the former has been chosen to display the magnitude of the strain in more detail, whereas in the latter the dot geometry is visible at first glance. Negative values of the hydrostatic strain correspond to hydrostatic compression, positive values of the [001] biaxial strain correspond to a compression in the xy-plane accompanied by an expansion in the z-direction and viceversa.

In order to study the strain distribution of a quantum dot and its surroundings I constructed the strain histograms of all elementary tetrahedrons in the supercell. The histograms are obtained by slicing the whole range of strain magnitudes into small units and then summing over the number of tetrahedrons of equal strain (within the width of one slice). This is shown in Fig. 4.9 for hydrostatic (top) and biaxial (bottom) strain calculated using the VFF (left) and XVFF (right) model. Only the tetrahedral elements corresponding to InAs were considered for this plot. This

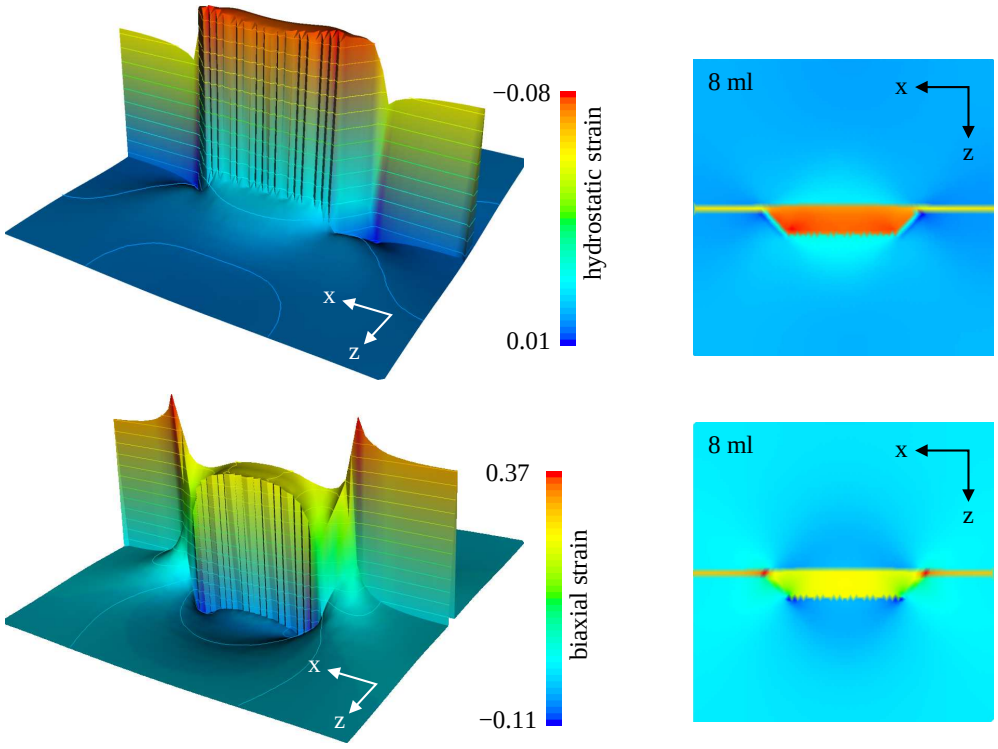

Figure 4.8: Cross sectional view of the hydrostatic (top) and biaxial (bottom) strain through the supercell positioned at the center of the quantum dot. Left and right figures show the same data, the former with a blown up strain scale, the latter as pseudo color plot seen in y-direction. The base length for a 8 monolayers large dot is about 17 nm.

is because for the barrier material (GaAs) surrounding the dot the average value of both hydrostatic and biaxial strain is found to be near zero. For InAs all histograms exhibit two maxima, which are associated with the strain in the QD and the WL. For example, for the eight MLs dot the average magnitude of the strain is about -0.08 and 0.023 for the hydrostatic and biaxial component, respectively, whereas the wetting layer (away from the dot) is strained by about -0.06 hydrostatically and 0.28 the biaxially. The reason for that kind of analysis is that what matters for a simplified strain model of the dots are the averaged strain values inside and outside the dot. Later on I will use these values for a one-dimensional strain-modified calculation of the electron and hole levels.

By comparing the *hydrostatic* strain histograms of quantum dots of different height we obtain an important information: The position of the maximum in the strain distribution corresponding to the dot is strongly dependent on dot height, whereas the average strain value in the wetting layer is almost independent of dot geometry. The shape of the latter is asymmetric showing a sharp cut-off on the high strain side. This can be understood by looking again at the strain cross

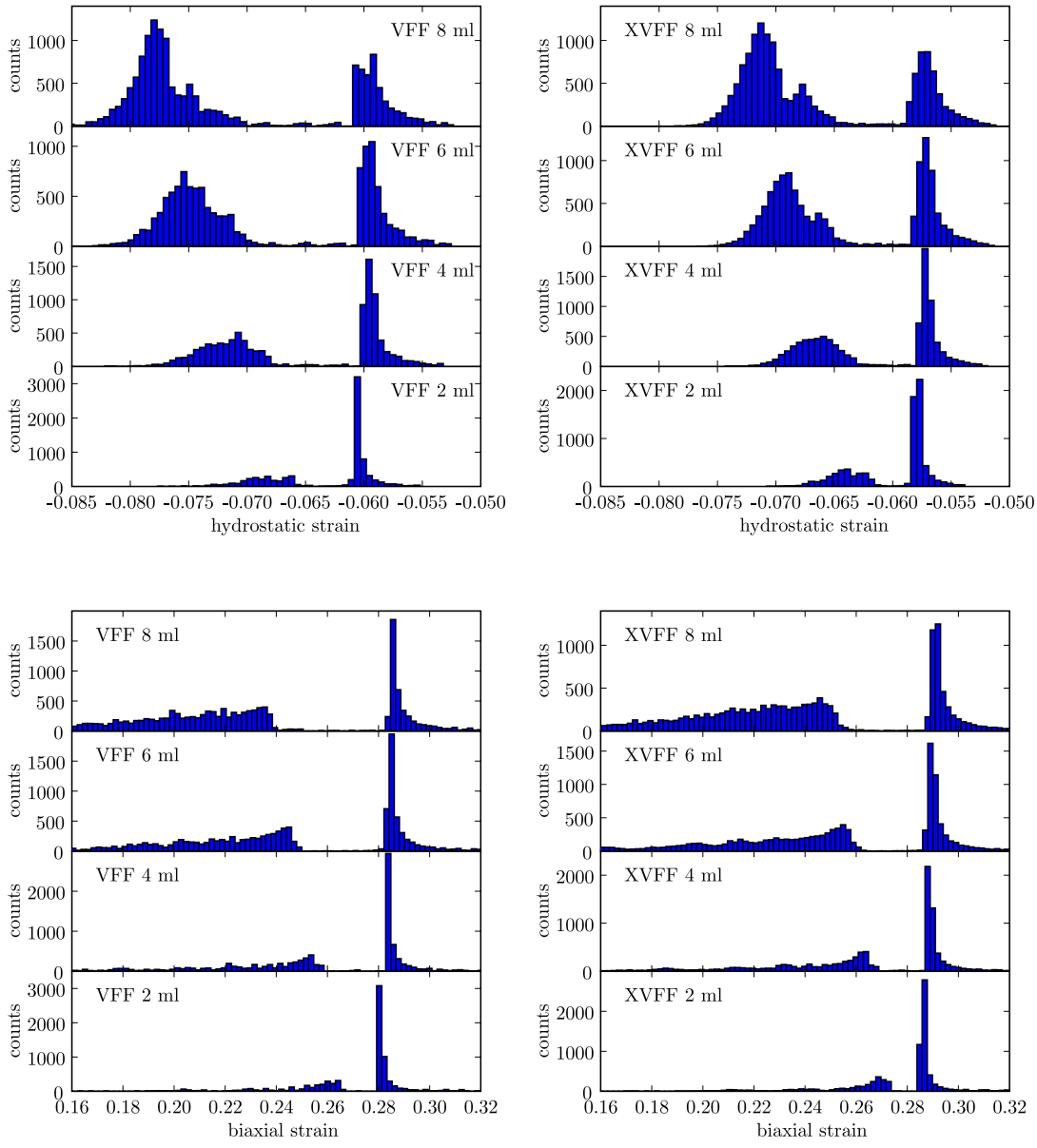

Figure 4.9: Distribution of the hydrostatic and biaxial strain components in all InAs within the supercell. The upper(lower) panels show the hydrostatic(biaxial) component of the strain. The left and right panels correspond to results obtained using the standard VFF and extended XVFF force field, respectively.

sections in Fig. 4.8. The strain in the wetting layer is smallest at the interface and approaches the value of a purely two-dimensionally strained layer given by the lattice mismatch between InAs and GaAs, as the distance from the dot increases. The other histogram maximum, which corresponds to the strain in the dot, is more symmetric and shifts to higher strain with increasing dot height.The dependence on height is a result of the three-dimensional character of the quantum dots. Since an infinitely extended xy-film, like the wetting layer is disconnecting the material below from that above, the strain in the film is equal to that of a free standing film, which is compressed in the xy-plane, and the strain in the surrounding material is zero. For a quantum dot the compressive stress of the surrounding GaAs acts as well in the z-direction, thus incresing the hydrostatic strain inside the dot. On the other hand, the biaxial strain can relax to some extent, at the cost of tensile biaxial strain in GaAs.

A comparison of the hydrostatic strain distribution calculated with the standard VFF and the extended XVFF model yields what was expected: the strain is smaller in average when treated within the XVFF model reflecting the increasing stiffness of the material when subjected to pressure. The strain in the largest dot is about 8 % smaller using the XVFF model. In the case of the biaxial strain (bottom panels), we also find a dependence of the strain on dot geometry. In contrast to the hydrostatic case, the biaxial strain is highest in the wetting layer and the same reason for the low strain cut-off as in the hydrostatic case applies.

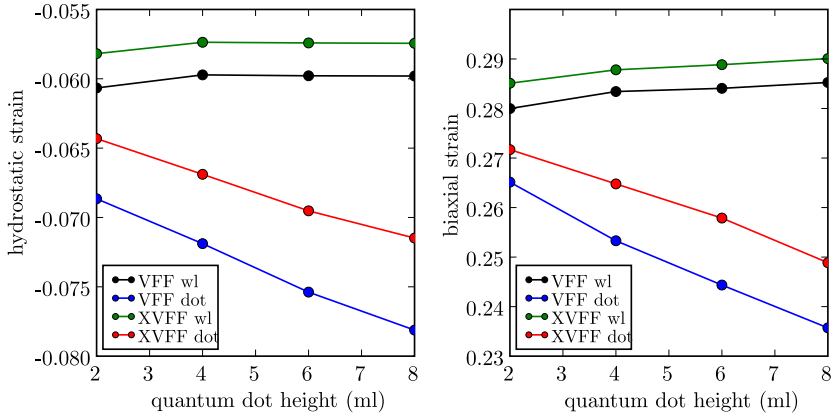

Figure 4.10: Comparison of the average strain in a InAs quantum dot and the wetting layer embedded in GaAs for four different dot sizes calculated with the standard and extended VFF. The left and right panels show the hydrostatic and biaxial strain, respectively.

The histogram peaks of hydrostatic strain have a relative FWHM of 5 %, whereas the distribution of biaxial strain is fairly broad and the description of the strain by an average value for the whole quantum dot is questionable. We should keep that shortcoming in mind, when discussing

the effects on the band structure. Figure 4.10 shows the average strain values taken from the position of the histogram maxima as a function of the quantum dot height. For both components of strain the VFF calculated strains are larger than those obtained from the XVFF model. The fact, that the wetting layer strain is not equal for all dot geometries considered, is due to a limitation of the calculations. The strain is not completely relaxed at the edges of the simulated supercell and the structure remains under some kind of small artificial strain. Therefore, the best value for the wetting layer should be that of the smallest dot but the deviation is small and will not be considered further. As expected, the strain in the QD increases less rapidly with the number of monolayer in the XVFF model.

We now turn to the simulation of the effects of an external pressure. A hydrostatic pressure applied on the facets of the supercell is achieved by decreasing the length of the periodic boundary. The corresponding pressure is calculated from the reduced volume using the definition of the bulk modulus, taking into account Murnaghan's equation for the pressure dependence of the bulk modulus.

$$\text{VFF}: \quad \text{P} = \quad -B_0 \ln\left(\frac{\Delta V}{V_0} + 1\right) \tag{4.2a}$$

$$\text{XVFF}: \quad \text{P} = \quad \frac{B_0}{B'}\left[\left(\frac{\Delta V}{V_0} + 1\right)^{-B'} - 1\right], \tag{4.2b}$$

where $\frac{\Delta V}{V_0} = \text{tr}\epsilon$, B_0 and B' are the bulk modulus and its first derivative, respectively. Figure 4.11 shows the pressure dependence of the hydrostatic strain in the quantum dots of 2-8 MLs height and the wetting layer calculated with the VFF model. On the left scale the equivalent pressure to the strain is indicated, obtained from eq. (4.2a). As a reference, the pressure dependence of the strain in bulk InAs is indicated with a dashed line. We notice that at ambient pressure one starts with a magnitude of hydrostatic strain within the embedded InAs, which is equivalent to an external pressure of about 4 GPa. The evolution of the strain in the QDs follows that of

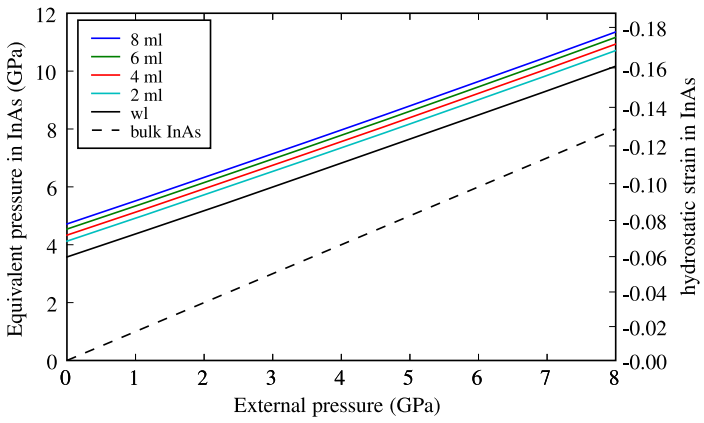

Figure 4.11: Hydrostatic strain in quantum dots of different heights (2-8 monolayers) and the wetting layer (wl) as function of external pressure calculated with the standard VFF.

the WL, as the pressure increases. The first remarkable result from the strain simulations is that the slope of the pressure dependence of the embedded InAs is much smaller than that of a bulk InAs crystal. If we assume a bulk hydrostatic band-gap deformation potential of -6.0 eV for InAs [3], we obtain a pressure coefficient of about 76 meV/GPa. Again, we compare these results to those obtained by the XVFF model, which is shown in Fig. 4.12. The strain in the

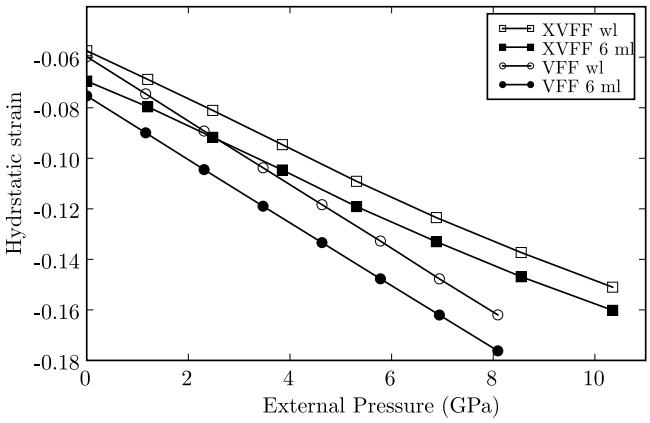

Figure 4.12: Strain in the wetting layer and a 6 monolayer high quantum dot as a function of external pressure, calculated using both the standard and the extended XVFF.

XVFF model yields a smaller pressure dependence, corresponding to a pressure coefficient of 62 meV/GPa. Furthermore, a significant sublinearity is observed, which amounts 0.8 meV/GPa^2. We can conclude that the emission from self-organized quantum dots is expected to exhibit a very low pressure coefficient, much lower than that of their constituent bulk material. I will demonstrate later that quantum confinement also has an influence on these values.

On the other hand, the biaxial strain slightly diminishes with increasing pressure. This reflects the difference in compressibility of both materials, which results in a reduction of the lattice mismatch with increasing pressure. In the pressure range of the simulation (0-10 GPa), though, the biaxial component decreases only by about 2 % and will assumed to be constant in the following. In this way we circumvent the problem of how to treat the broad biaxial strain distribution in a simple one-dimensional model, as mentioned above, since we are mainly interested in the pressure dependence of the band-edge energies rather than in their absolute values.

A large spread of the PC values has been observed experimentally. To address this issue we determine the difference in strain between the wetting layer and dot for each height of quantum dot, as shown in Fig. 4.13 as a function of external pressure. In fact, a small systematic variation is detected. The strain in the larger dots rises slower than that in the smaller ones and the wetting layer strain has the steepest slope. Unfortunately, the numerical results from the XVFF model under pressure, shown on the right side, do not behave so nicely as those obtained with the VFF model. It seems that the global minimum was not found in the relaxation process of the

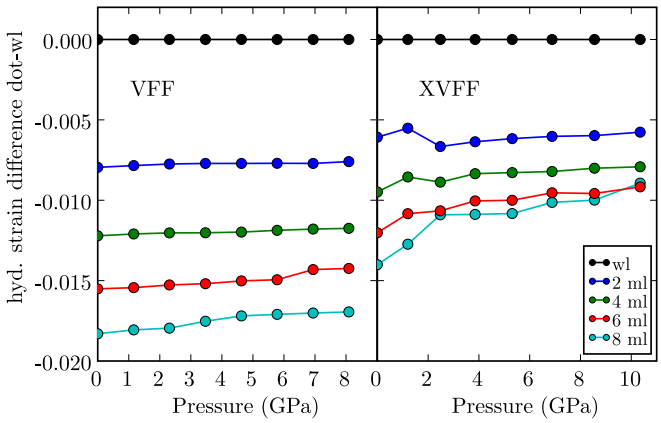

Figure 4.13: Difference in hydrostatic strain between wetting layer and dot for different dot heights obtained by applying the standard (left) and extended (right) VFF.

calculations. Compared to the zero-pressure results, a cross-sectional view of the structure looks slightly distorted. The origin of this numerical problem is not clear but it might be connected to the special shape of the bond-stretching potential. This will be discussed further in section B. If we forget the numerical problems for the moment, at least the trend is the same as that observed with the VFF model: The larger the dot, the lower the slope of the pressure dependence. However, even if we assume that this variation is larger within the XVFF model, it is not sufficient to explain the significant size dependence of the measured pressure coefficients.

Strain modified band edges

Once we know the strain field of a quantum dot, it is possible to estimate the band edges along a line across the supercell by calculating the energy shifts produced by strain using equations (3.40a-3.40c) and (3.42a,3.42b) together with the hydrostatic and shear strain deformation potentials and the spin-orbit energy listed in table 4.1. This is illustrated in Fig. 4.14 based on

	a	a_v	b	$\Xi_d + \frac{1}{3}\Xi_u$	Ξ_u	Δ_0
InAs	-6.0	-1.0	-1.8	1.5	3.2	0.38
GaAs	-8.4	-1.2	-2.0	1.5	6.5	0.341

Table 4.1: The hydrostatic and shear deformation potentials used in the simulation, taken from reference[3].

strain calculations for an eight monolayers high quantum dot using the XVFF model along the [001] direction through the center of the dot, as indicated in the inset. The valence band offset for the strained interface is adjusted to 290 meV, which is the value obtained from the experiments in section 4.1.1. The shown profiles correspond to the Γ and the strain-split X conduction bands as well as the three valence bands at Γ. We notice that the E_{v2} band, which corresponds to a heavy hole band, becomes the highest valence band in InAs. The profile of the lowest band edges has the shape of a one-dimensional square well potential in good approximation,

which is a prerequisite for the application of the envelope function approximation discussed in section 3.2.2. Furthermore, the band-gap of the embedded InAs has increased from 0.42 eV to about 0.61 eV for the largest dot and to 0.54 eV for the smallest one. The X conduction band energy in InAs is higher than in GaAs and split by about 200 meV. In the vicinity of the dot, all bands are slightly bent, resulting in a modification of the band gap in GaAs too. Specially the indirect $X-\Gamma$ band-gap in GaAs is lowered with respect to the bulk GaAs energy.

In order not to stress this simple band-structure estimation too much, I will make some simplifications to study the pressure dependence. The [001] biaxial strain is taken to be constant in the simulated pressure range, as pointed out in the last section. As the absolute valence band offsets of InAs and GaAs are comparable, I will further assume a constant valence band offset. The variation of the hydrostatic strain between different dot sizes is small and the related variation in the InAs band gap is small compared to the expected confinement energies. With the results from the previous section we are now able to estimate the variation of the conduction band offset with pressure, as shown in Fig. 4.15. These findings enable us to confirm the assumptions made in the experimental section. There we proposed that the appearance of a ninth peak in the PL spectrum at about 1 GPa, which corresponds to the transition of quantum dots of one monolayer height, is due to the confinement of an additional discrete electronic state, caused by the increasing conduction band offset. Indeed, the increase is fairly pronounced from both VFF models. It amounts 28 meV/GPa and 46 meV/GPa in the VFF and XVFF model, respectively. The other assumption made concerns the existence of a transition which is about 60 meV lower in energy than that of the indirect $X-\Gamma$ gap of GaAs and whose electronic state seems to be responsible for the $\Gamma-X$ crossover in the quantum dots. Looking again at Fig. 4.14 we can expect that this state corresponds to the X_Z one of GaAs near the heterointerface. The crossing of this state with the rising Γ-point states of InAs leads to the quenching of the emission from the quantum dots.

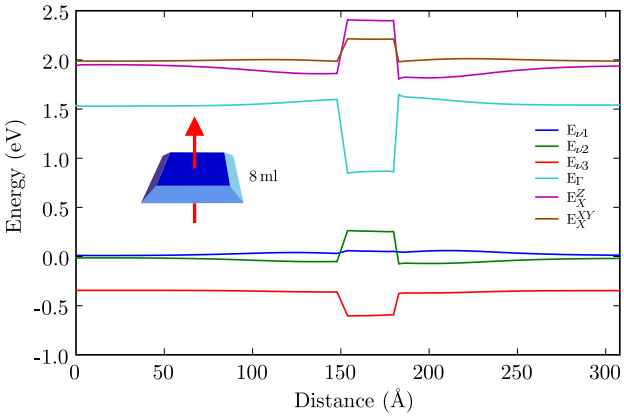

Figure 4.14: Band profiles along [001] direction through the center of a truncated pyramid shaped QD with a height of 8 MLs at ambient pressure.

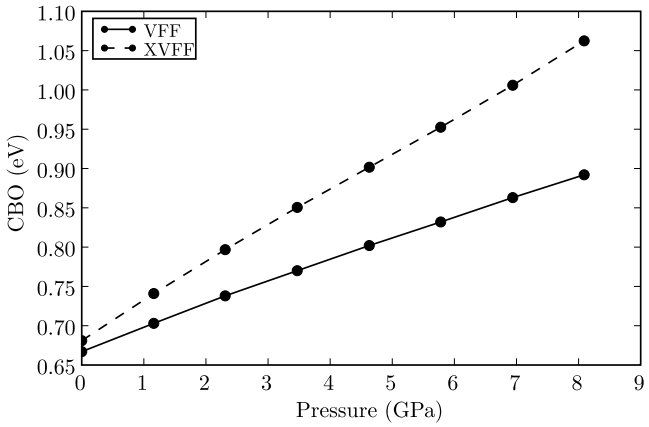

Figure 4.15: The calculated conduction band offsets as a function of pressure.

Inclusion of quantum effects

Taking into account the results obtained in the previous sections, we will now address the effects of quantum confinement on the pressure dependence of the quantum dot states. We further assumed a pressure independent valence band offset and a strongly rising conduction band offset. Thus, any variation of the pressure dependence on dot geometry should come from the pressure dependence of the electronic states. Figure 4.16 displays the electronic ground state energies for four different dot heights as a function of external pressure, calculated within the EFA and considering the non-parabolicity of the electron mass (3.26). Also indicated are the GaAs and

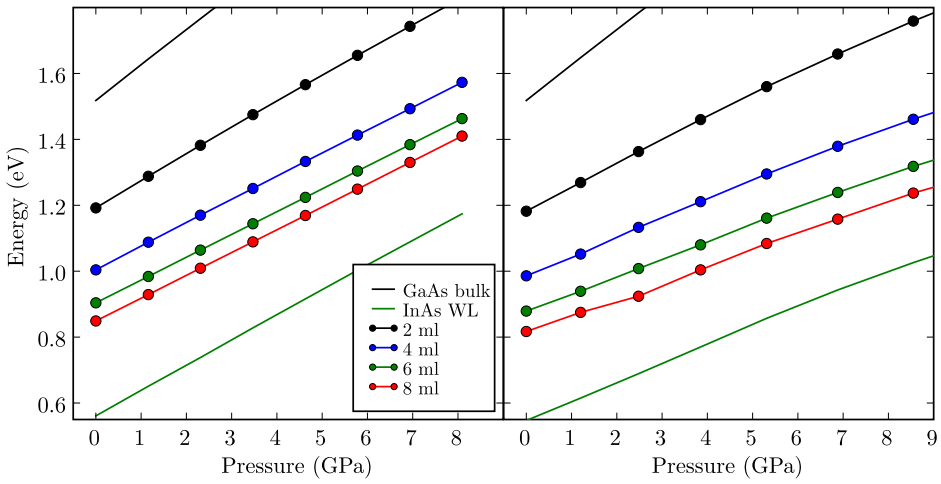

Figure 4.16: The calculated pressure dependence of the electronic ground-state energies for four different QD heights as a function of external pressure. The results in the left(right) panels are based on the VFF(XVFF) model.

InAs conduction band energies. An interesting point is that the ground-state energy in the largest dot has a significantly lower pressure coefficient than the InAs band edge. This is simply due to the energy dependence of the effective mass. As a result, the confinement energy decreases with increasing band edge energy. Thus, the slope of the band edge is not necessarily setting the lower limit of possible PCs. The smaller dots have a remarkably higher PC and follow the GaAs band gap, the higher their confinement energy is. From another point of view, the wavefunctions of the electrons in the larger dots are mostly confined to InAs and adopt its properties, whereas a large part of the electronic wavefunctions of the smaller dots penetrates into the GaAs barrier and is strongly influenced by the properties of bulk GaAs, namely its pressure coefficient. The differences in pressure coefficients are better seen when fitting the data with the usual quadratic expression (4.1) and plotting the coefficients a and b as a function of the electron energy. This has been done in Fig. 4.17. The linear coefficient ranges from 69 meV/GPa to 84 meV/GPa

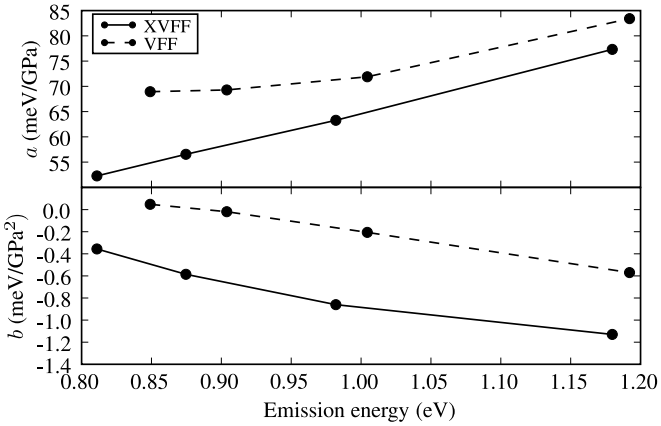

Figure 4.17: The pressure coefficients of the electronic ground states as a function of their energy, calculated within the EFA for four different QD heights.

when using the VFF and from 52 meV/GPa to 78 meV/GPa when the calculations are based on the XVFF model. The quadratic coefficients are at most -0.6 meV/GPa^2 and -1.1 meV/GPa^2 for the VFF and XVFF model, respectively. Thus, both models yield a variation of the PC depending on the dot height. The qualitative agreement with the experimental data (see Fig. 4.7), e.i. the linear dependence on emission energies is better reproduced, if the calculations are based on the XVVF, although the absolute values are lower than the experimental ones. Considering the simplicity of the model, specially its one-dimensionality, the results are very good and the origins of the different effects, which play a role to produce the PC variation with pressure can be well separated.

4.1.3. Conclusion

In this chapter results from photoluminescence experiments on self-organized InAs/GaAs quantum dots under high hydrostatic pressure were presented. Due to the multi-modal distribution of the dot size, it was possible to determine the pressure coefficients (PC) of quantum dots of different sizes under exactly the same environmental conditions. In this way, I was able to address the problem, why all measurements on InAs/GaAs quantum dots reported so far, yield different pressure coefficients ranging from 60 meV/GPa to 110 meV/GPa, which is in average much smaller than the bulk InAs value. For that purpose I have performed pressure-dependent strain simulations based on an atomistic valence force field (VFF). Four dot heights of 2–8 monolayers have been calculated, embedded in a GaAs supercell containing up to 1.3 million atoms. Two force field models have been applied, a standard Keating VFF and an extended version (XVFF), which accounts for the pressure dependence of the bulk modulus. The first result is, that the pressure coefficient of an InAs monolayer embedded in GaAs is at least 62 meV/GPa. Furthermore, a variation of the pressure coefficients depending on the dot size is obtained when considering the effects of quantum confinement within a one-dimensional envelope function approximation picture. The variation of PCs is not as pronounced as found experimentally, which is not surprising considering the simplicity of the model, however, it gives insight into the physical origin of the effects leading to this interesting behavior.

A second interesting point is, that the quenching of the quantum dot emission occurs when the confined states cross the X_Z state of the barrier material. Measuring the $X_Z - \Gamma$ transition energy of GaAs, it is possible to infer the valence band offsets of the heavy hole states. As expected, the offset increases with the size of the dot. Fitting this size dependence to the Daniel-Duke model of a square well potential we can extrapolate a value of 290 ± 10 eV for the valence band offset for the heterointerface of strained InAs/GaAs quantum dots.

4.2. InP/GaP quantum dots

Heterostructures of the InP/GaP material system present an even larger built-in strain (7.7 %) than for the InAs/GaAs system, due to the larger lattice mismatch. Because of the fact that the elastic constants in bulk InP are larger than in InAs [64], a higher strain energy is expected, which should lead to earlier strain relaxation and larger dot sizes [65]. The sample investigated in this work has a density of QDs of about $9 \times 10^7\,\mathrm{cm}^{-2}$. The base length is 25-40 nm and the height is between 4 and 5 nm. In comparison with the InAs/GaAs sample, the density is lower, whereas the size of the QDs is larger. Details on the growth sequence can be found in Ref. [65]. For structures using $In_{0.48}Ga_{52}P$ as barrier material, which is lattice matched to a GaAs substrate, intense luminescence from the InP islands has been reported at photon energies between 1.6 and 1.85 eV [66–68]. In the case of GaP as matrix, the larger built-in strain is expected to shift the energy of the fundamental optical transition close to that of the indirect Γ-X band gap. This would probably result in a less efficient radiative recombination if the optical transition is indirect in reciprocal space and/or it would even lead to a type-II carrier confinement with electrons and holes spatially separated, which seems to be the case for ultrathin InP/GaP quantum wells [69]. This is the trade off for having GaP as substrate material, which is of great advantage for optoelectronic applications due to its transparency at the wavelengths of the dot emission. In the following sections I will determine the actual band lineup across the heterostructure using results from photoluminescence experiments under high hydrostatic pressure and I will show and explain important results about the peculiar carrier dynamics in this system.

4.2.1. Band structure from high pressure experiments

Figure 4.18 displays low-temperature PL spectra of the InP/GaP sample for different pressures up to 1.2 GPa taken with 5 kW/cm^2 laser power density. The prominent peak corresponds to the emission from the quantum dot (QD), whereas the much weaker feature at around 2.2 eV is assigned to optical transitions between confined states in the wetting layer (WL). At ambient pressure the main emission of the sample peaks at 1.92 eV and its width is about 70 meV, exhibiting an asymmetric double peak structure. As I will show in the following, the strong emission at 1.92 eV at ambient pressure is due to direct optical transitions between Brillouin-zone-center states of the dots. This implies type-I band alignment, i.e. the energetically lowest point of the conduction band structure resides at the location of the InP islands. The width of the dot emission band reflects the size and probably composition distribution of the dots. At the laser powers of the experiment and for the low dot density of this sample, we expect saturation

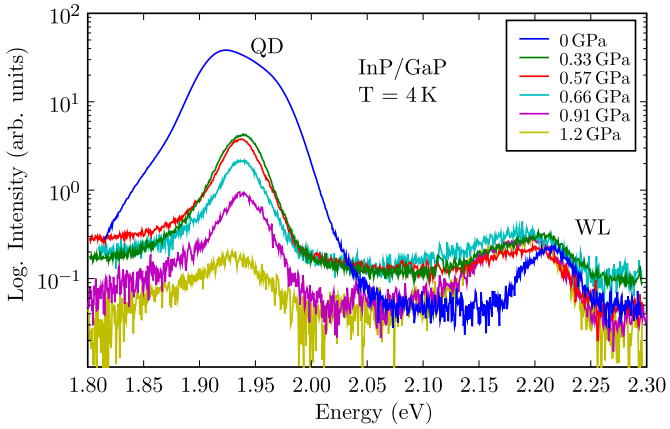

Figure 4.18: Photoluminescence spectra of a self-organized InP/GaP sample taken at at different pressures.

of the dot emission to be achieved; thus, the double peak apparent in the 0 GPa spectrum (see Fig. 4.19a) is attributed to recombination processes between the electron and hole ground states (e_0-hh_0) and the first exited ones (e_1-hh_1), respectively. In fact, the peak corresponding to the first-excited state recombination becomes more pronounced with increasing laser power density due to the saturation of the population of photoexcited carriers in the ground state.

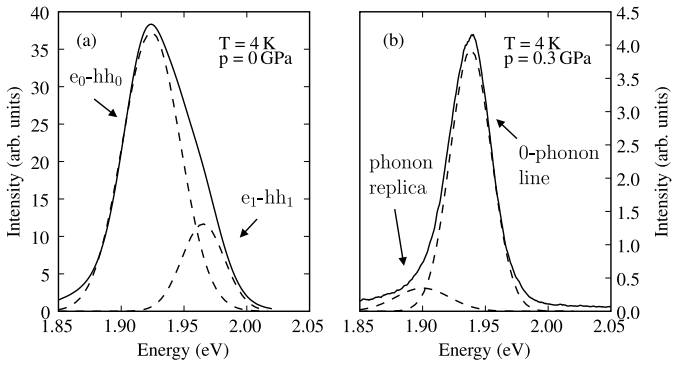

Figure 4.19: Ambient pressure (a) and 0.3 GPa (b) spectrum in the energy region of the QD emission. Dashed curves represent Gaussian line shapes fitted to the measured spectra. Their assignment is indicated.

At finite pressure a sudden blue shift of the PL maximum of about 20 meV occurs together with a reduction of the intensity by a factor 16 and the narrowing of the band width. With increasing pressure the peak energy of the QD is decreasing slowly, as it is the case for X-Γ indirect transitions [45]. Further evidence for the indirectness of the optical transition at finite pressure is obtained from a line shape analysis of the QD emission band. A representative PL spectrum recorded at 0.3 GPa and at 4 K is shown in Fig. 4.19b). The emission peak exhibits a slight asymmetry towards lower energies due to a weaker line shifted down in energy by about 40 meV, which is the energy of the zone-edge phonons in InP [3]. The main peak thus corresponds to the zero-phonon line activated in quantum dots due to the breakdown of the translational invariance and the weaker feature at lower energies is attributed to the one-phonon replica

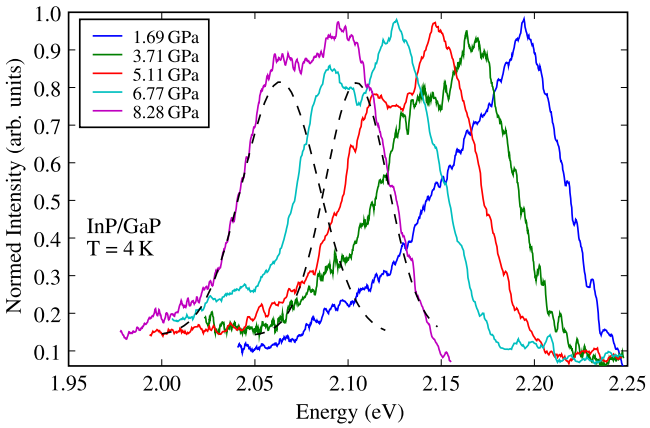

Figure 4.20: Pressure dependence of the WL emission for different pressures. The dashed lines are Gaussian line shapes fitted to the data.

of the indirect emission. The reason for the narrowing of the indirect PL peak as compared with the direct one at ambient pressure is that the energy of the conduction band X-point levels is less dependent on confinement, because of the larger effective mass.

The wetting layer luminescence also shifts to lower energies as demonstrated in Fig. 4.20 what speaks for these transitions being of $\Gamma - X$ indirect character. The emission line shape is very similar to that of a 1.5 monolayer InP/GaP sample [69], whose peak like features were interpreted as different phonon replica associated with the indirect optical transition. The line shape has been fitted with two peaks, although an exact assignment to different phonon-assisted processes is problematic. The peak separation of about 38 meV at 0 GPa increases with increasing pressure at a rate of 0.5 meV/GPa, which is about the zone-edge LO phonon energy of a III-V compound and its pressure dependence. The wetting layer represents a kind of δ-like potential well for carriers in the GaP matrix. This situation also holds for the conduction band X minima since those of the InP WL are split by the built-in strain and pushed down in energy with respect to the X valleys in the GaP barrier. High-pressure experiments on an InAs monolayer in GaAs combined with tight-binding calculations have shown the existence of a bound state for electrons lying a few meV below the X conduction-band edge of the barrier material [70]. Hence, the WL feature is attributed to optical transitions between states bound to the highly strained InP wetting layer, which are direct in space (type I) but indirect in reciprocal space. In fact, the WL emission is 120 meV lower in energy than the band gap of GaP and the luminescence of the barrier is completely absent in the spectra.

The energies of the PL peak maxima obtained from low-temperature spectra are shown in Fig. 4.21 as a function of pressure. Whereas the emission from the wetting layer shifts to lower energies at a rate of -13.9$\pm$5 meV/GPa, typical for the $\Gamma - X$ indirect gap of GaP [71], the QD line displays a much smaller pressure coefficient of -4.4$\pm$5 meV/GPa. The pressure dependence

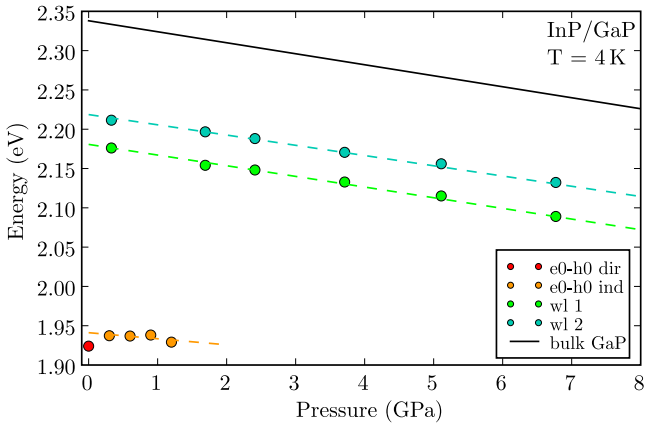

Figure 4.21: Pressure dependence of the PL peak energies of the InP/GaP sample at 2 K.

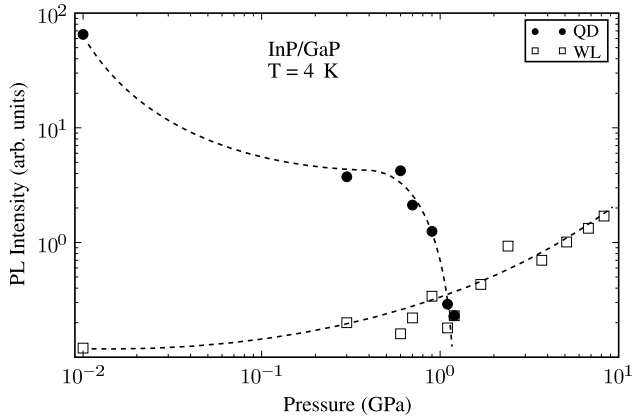

Figure 4.22: Pressure dependence of the peak intensities of the InP/GaP sample at 2 K. The dashed lines are a guide to the eye. Both axes are in logarithmic scale.

of the PL peak intensities is shown in Fig. 4.22. The initial reduction in intensity of more than one order of magnitude is also a clear indication of the occurrence of the $\Gamma - X$ conduction-band crossover in the InP dots. Moreover, the quenching of the dot luminescence above 1.2 GPa is due to a type-I/II transition, at which the conduction band X valleys in the WL or the barrier become lower in energy than that ones in the InP dots. In contrast, the WL emission increases monotonically with increasing pressure.

The small measured negative pressure coefficient of the QD emission compared to that of bulk InP of -17±3 meV/GPa [72] is at least partly due to a reduction of the biaxial strain induced X-valley splitting. As demonstrated in section 3.2.3, a biaxial [001] strain splits the sixfold degenerate X-bands into a X_z doublet and a X_{xy} quadruplet. The centroid energy is decreasing with increasing pressure and the splitting is proportional to the [001] biaxial strain. Thus, if the biaxial strain is decreasing with rising pressure, the effective pressure coefficient of the X_{xy} state will be lowered in absolute value with respect to that of the centroid energy. The reduction of the biaxial strain is the result of a difference in bulk modulus between InP (71.1 GPa) and GaP

(88.2 GPa) [3]. Since InP is more compressible than GaP, under pressure the lattice mismatch between both materials continuously reduces and so does the biaxial strain in InP. The pressure dependent lattice mismatch can be calculated by:

$$\varepsilon_{xx} = \frac{a_s}{a_f} e^{\frac{p}{3}\left(\frac{1}{B_s} - \frac{1}{B_f}\right)} - 1, \tag{4.3}$$

where p is the pressure and a and B with indices s and f are the lattice constant and bulk modulus of the substrate and the film, respectively. The average biaxial strain of an InP quantum dot at atmospheric pressure obtained from VFF calculations is about 0.24. Assuming a InP X-conduction band shear deformation potential Ξ_u of 3.3 eV as obtained by tight-binding calculations in Ref.[73], the inital X-splitting, calculated by eq. (3.43b) is about 0.4 eV. Using eq. (4.3) we can estimate, that the splitting is reducing at a rate of about 4 meV/GPa, divided into one third/two thirds contribution to the X_{xy}/X_z states respectively. As the region, where the $\boldsymbol{k}$-indirect QD *phase* exists is as narrow as 0.8 GPa, the bands involved in the type-I/II transition are initially very close to each other. Considering the typical pressure coefficient of a X-Γ indirect band gap (≈ -10 meV/GPa), this corresponds to an energy range of about 10 meV. As a consequence, it is also plausible, that band-mixing effects contribute to the small pressure coefficients of the indirect QD emission and the consecutive type-I/II quenching. This has shown to be important even for the mixing between Γ and X-bands near the crossover pressure [74, 75].

As for pressures above 1.2 GPa the WL emission is the only observed signal, we infer that the type type-I/II transition in the QDs is due to the crossing with the X-bound states in the WL. This will be further confirmed in time-resolved PL experiments by the observation that the carriers reach the quantum dot via the wetting layer. From the difference of oserved pressure coefficients we infer, that the separation between the X-states in the dot and the WL decreases at a rate of about -10 meV/GPa. Because the degeneracy of conduction band minima is achieved at about 1.2 GPa, as indicated by the quenching of the dot luminescence, we can estimate the energy position of the X_{xy} states in the QDs at ambient pressure being about 10 meV below the X level bound to the wetting layer. From these observations we can finally sketch the conduction band lineup as a function of pressure, shown in Fig. 4.23.

4.2.2. Temperature dependence

The temperature dependence of the quantum dot ground-state emission and that of the wetting layer is very different at pressures below the type-I/II crossover. Figure 4.24 shows an example for a pressure of 0.7 GPa. Whereas the quantum dot emission exhibits a clear maximum at a temperature of about 50 K, the wetting layer intensity drops continuously and vanishes at about 50 K. The quenching of the WL luminescence with rising temperature is due to the thermal es-

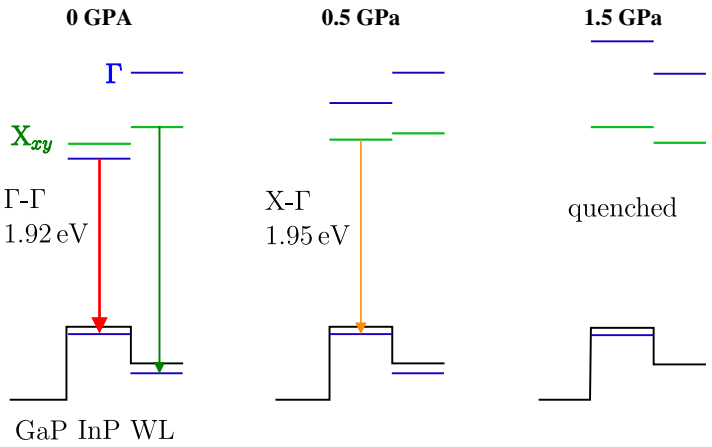

Figure 4.23: Band lineup at ambient pressure, at a pressure above the Γ-X crossover and at one above the type-I/II transition.

cape of the confined carriers into the barrier and to the activation of non-radiative recombination channels. The initial increase of the quantum dot luminescence at low temperatures speaks for an improvement of the carrier transfer from the barrier into the quantum dots with increasing temperature. Considering the low dot density in this sample (only about 10 % of the wetting

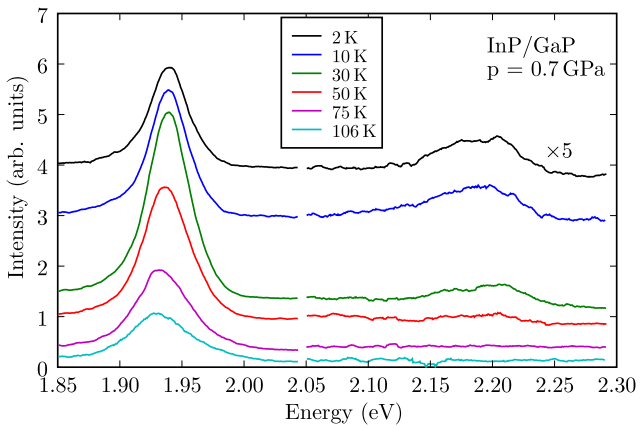

Figure 4.24: Temperature dependence of the quantum dot and wetting layer emission at 0.7 GPa.

layer area is covered with islands), we assume that most of the carriers will reach the dots via the wetting layer and only some of them take the direct path from the barrier. Width fluctuations of the wetting layer will create potential sinks where the carriers can localize at sufficient low temperatures and therefore will not reach the quantum dots. However, temperature reactivates carrier mobility and the overall capture rate of carriers in the quantum dots will increase. To confirm this, a system of rate equations considering the most important processes, as illustrated in Fig. 4.25, has been setup inspired by those of reference [76]. The carriers enter the quantum dot either directly from the barrier or through the wetting layer. Once in the WL, they have to overcome a small potential barrier, which corresponds to monolayer fluctuations in the WL, to reach the quantum dot. They could also leave the WL by radiative recombination with the holes.

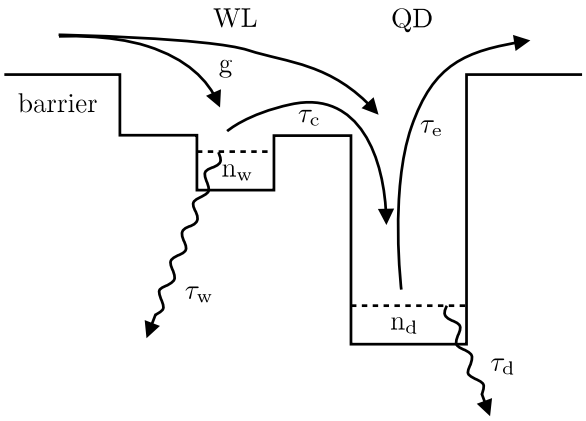

Figure 4.25: Schematic view of the conduction band edge. With increasing temperature the carriers localized in the wetting layer are activated and contribute to the quantum dot emission.

The QD has two input channels and two output channels, a radiative one and an escape channel to the barrier. This model does not account for the size distribution of the quantum dots and the resulting energy spectrum of the quantum dot ground states. Furthermore, it disregards the existence of non-radiative recombination channels but it is, as shown below, sufficient to understand the unusual temperature dependence of the QD emission. The rate equations corresponding to the above processes read

$$\begin{aligned} \frac{dn_w(t)}{dt} &= -\frac{n_w(t)}{\tau_w} - \frac{n_w(t)}{\tau_c} + a * g \\ \frac{dn_d(t)}{dt} &= \frac{n_w(t)}{\tau_c} - \frac{n_d(t)}{\tau_d} - \frac{n_d(t)}{\tau_e} + (1-a) * g, \end{aligned} \tag{4.4}$$

where $n_{w/d}(t)$ denotes the number of carriers in the localization potentials of the wetting layer or the dots, $\tau_{w/d}$ are the time constants for the radiative decay, $\tau_{c/e}$ are those for the capture and emission process into and from the QD and g is the generation rate of carriers in the barrier. Solving the stationary state of the coupled equations, i.e. setting $\frac{dn}{dt} = 0$, the integrated PL intensities from the QDs and the WL is given by

$$\begin{aligned} I_w = \frac{n_w}{\tau_w} &= \frac{a\tau_c g}{\tau_w + \tau_c} \\ I_d = \frac{n_d}{\tau_d} &= \frac{\tau_d \tau_e g \tau_w + (1-a)\,\tau_c \tau_d \tau_e g}{\tau_d\left(\left(\tau_e + \tau_d\right)\tau_w + \tau_c \tau_e + \tau_c \tau_d\right)}. \end{aligned} \tag{4.5}$$

These expressions are now used to model the temperature dependence of the luminescence of both the WL and the QD, as shown in Fig. 4.26 for a pressure of 0.7 GPa. The symbols correspond to the measured integrated peak intensities. The temperature of maximal PL intensity is determined by the interplay of the activation energy of the carriers in the wetting layer and that, which is needed by the carriers to leave the quantum dots. The radiative lifetime τ_d of the quantum dots is considered to be independent of temperature as the carriers are confined in all three dimensions. That is not true for the radiative lifetime of the wetting layer τ_d which

has been shown to rise linear with temperature [77], fact which is ignored in this consideration. Temperature dependence is introduced via the capture and emission rates of carriers to and from the quantum dot ground state

$$\frac{1}{\tau_{c,e}} \sim e^{-E_{c,e}/kT}, \tag{4.6}$$

where E is the activation energy which has to be gained in order to escape from the WL localization potentials or the QD, k is the Boltzmann constant and T is the temperature. Modifying the capture and escape time constants of Eq. (4.5) according to Eq. (4.6) we obtain the temperature dependence of the dot and wetting layer emission shown in Fig. 4.26 together with experimental data obtained at a pressure of 0.3 GPa. The solid lines are calculated by using equations (4.5) with an euristic choice for the set of parameters. That was necessary due to a lack of experimental data. Nevertheless, the aspects that are specially interesting at this point, i.e. the observation of a finite temperature for maximum dot emission as well as the monotonic decay of the wetting layer PL, are well reproduced by the solutions of the rate equations. Both aspects are mainly determined by the interplay between the activation energies E_c and E_e. If we perform this analysis

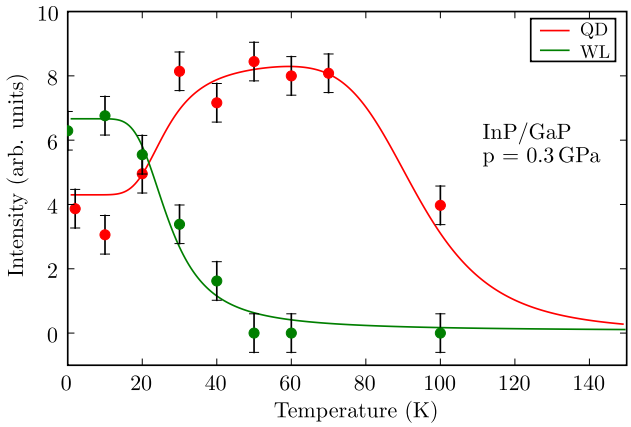

Figure 4.26: Temperature dependence of the integrated peak intensity of the PL from the dots and wetting layer at 0.3 GPa. The solid lines represent a solution of the rate equations.

at every pressure below the type-I/II crossover we obtain a linear relation between the temperature of maximum QD emission, i.e. the activation energy of the quantum dots, and the applied pressure, which is shown in Fig. 4.27. Since the dependence of the band edges on pressure is linear in good approximation, the same should hold for the activation energies. In contrast, the activation energy for the carrier capture is constant with pressure, which is an indication that localization effects in the wetting layer are independent of pressure.

4.2.3. Carrier dynamics

For the discussion of the time evolution of the PL in the InP/GaP quantum dot system it is important to compare the emission spectra obtained under continuous wave (cw) and pulsed

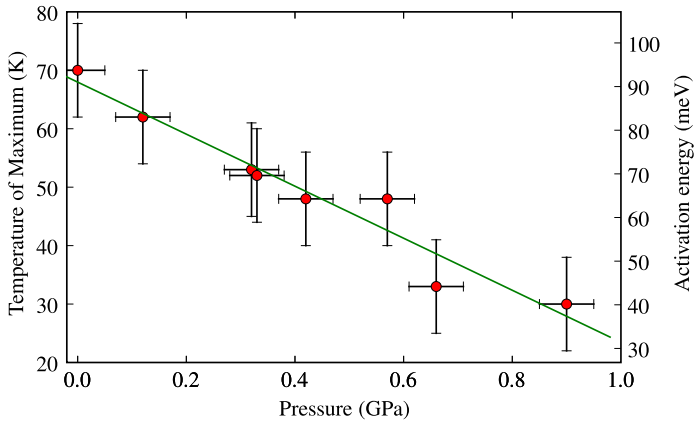

Figure 4.27: Pressure dependence of temperature of the maximum in dot luminescence and of the activation energy of the quantum dot ground state.

excitation. Figure 4.28 shows on logarithmic scale two spectra measured at low temperatures with cw excitation at ambient pressure and at 0.3 GPa, i.e. for the case where the QD emission is direct and indirect in reciprocal space, respectively. For comparison I also show a typical spectrum obtained at 0 GPa using the pulsed light source. Due to the very high power of the short pulses and to the fact that the areal dot density of the sample is rather small, the ground state recombination from the QDs is easily saturated. As a consequence, radiative recombination from excited states of the dots as well as the wetting layer (WL) luminescence become apparent in the PL spectra. Moreover, according to the electronic level structure obtained from high-pressure experiments presented in section 4.2.1, the PL spectra under pulsed excitation always contain a contribution from indirect recombination processes in the dots even at zero pressure. This explains the much larger width of the QD emission for pulsed excitation and that its lineshape does not change appreciably under pressure besides for variations in intensity.

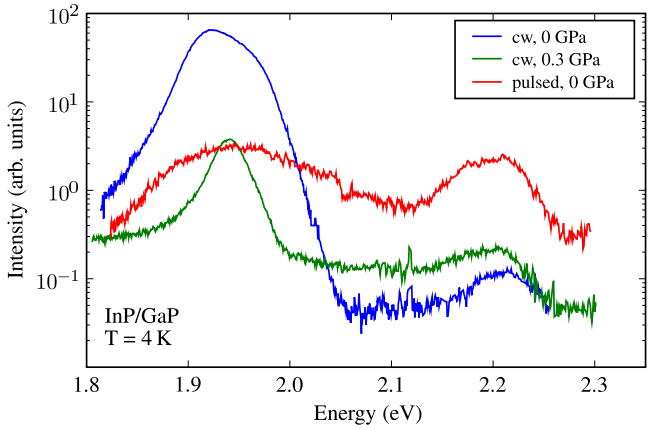

Figure 4.28: Comparison of Pl spectra of the InP/GaP QDs taken with continuous wave (cw) and pulsed excitation.

Figure 4.29 shows the spectral distribution of the luminescence decay of the InP/GaP QD structure obtained at ambient pressure and 2 K. The transients measured at three different photon

energies, as indicated by the three dashed lines in Fig. 4.29 are depicted in Fig. 4.30a) and b). The PL decay from the QDs (at 1.95 eV) is best modelled using three mono-exponential decay components, shown in Fig. 4.31. The fastest of them with about 1 ns decay time is considered a spurious component since it is found throughout the whole spectral range. The transient measured at 2.1 eV gives an example of such fast decay which possibly originates from recombination processes in the GaP substrate and will thus be no longer discussed. The remaining two components of the dot emission exhibit decay times of about 5 ns and 30 ns, which we attribute to the in reciprocal space direct and indirect radiative recombination processes, respectively, between electrons and holes confined in the InP quantum dots. At ambient pressure the main PL component as far as the intensity is concerned corresponds to the direct $\Gamma - \Gamma$ one with the decay time of 5 ns at the peak maximum. The decay time attributed to the direct optical transition is long compared to that of InAs/GaAs QDs [78–80]. Considering that the X-states of both the QDs and the WL are within an energy range of 30 meV above the Γ state in the dots, the wave function at the Γ point will probably contain an admixture of X-states, thus reducing the matrix element which couples the electrons and holes, which results in a longer decay time. As indicated by the asymmetric shape of the dot peak in the contour plots of Fig. 4.29, the decay time decreases to about 2 ns on the high-energy tail reflecting the faster relaxation of the excited states of the dots. Since at high excitation levels the ground and lowest excited states of the dots are filled with carriers, a decrease of the decay time with increasing energy at low temperatures can only be explained by invoking carrier promotion to higher excited states or even the wetting layer via electron-electron interaction (many-body effects) in the dots [81].

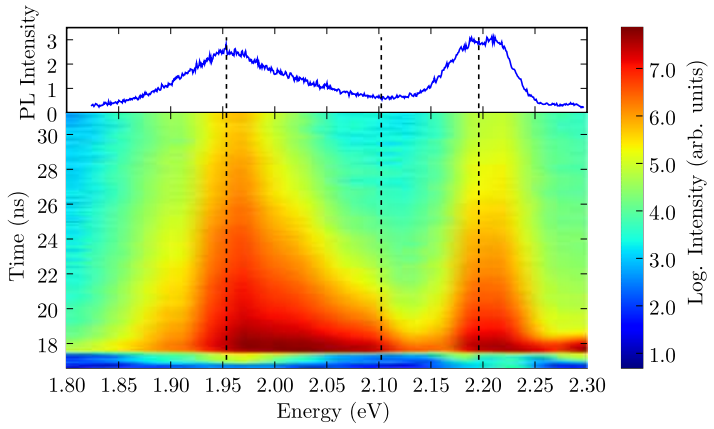

Figure 4.29: Spectral distribution of decay times of the emission from the dots and wetting layer at ambient pressure and 2 K.

The wetting layer emission, in contrast, displays a multi-exponential decay. The solid curve in Fig. 4.30b) represents the result of a fit to the transient data with a stretched exponential function

$$I(t) = I(0)e^{-(t/\tau)^{\beta}}, \tag{4.7}$$

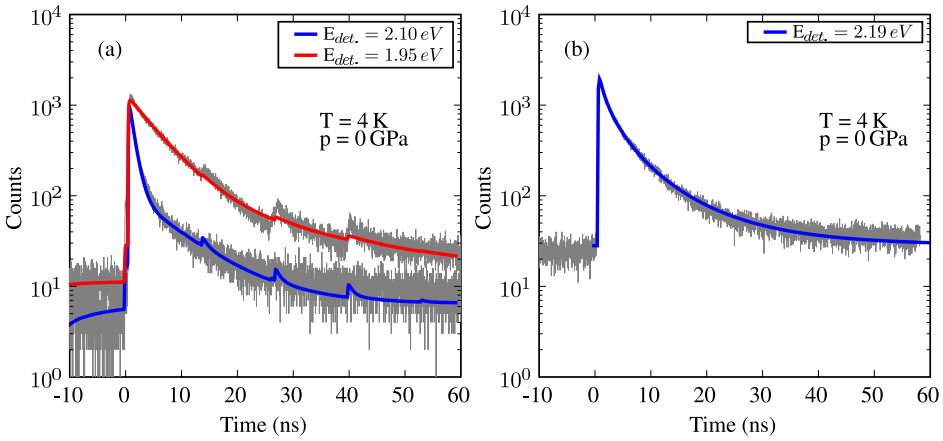

Figure 4.30: Transients measured at the energies indicated in the figure legend. Solid curves are fits to the measured transients.

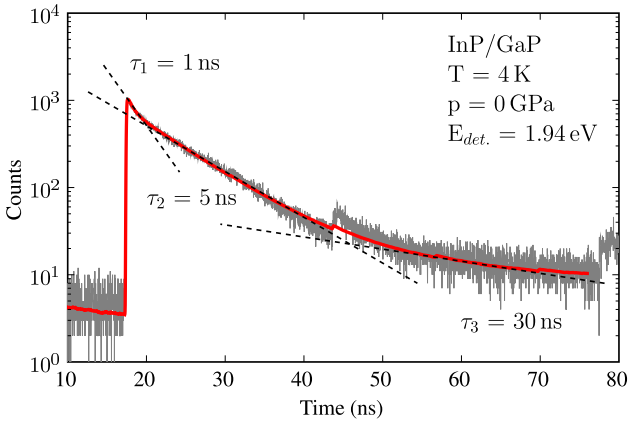

Figure 4.31: Example of the fitting procedure for the PL decay of the QD at low temperatures and ambient pressure. The dashed lines indicate the three monoexponential components used to account for the QD related decays.

where $\beta = 0.43$ and $\tau = 490\,\text{ps}$ are the exponent and time constant, respectively. This temporal behavior is usually found for the dynamics of heavily disordered systems [82]. A small value of the β parameter (less than 1) is indicative of a broad distribution of decay times, which in our case results from noticeable fluctuations in the WL thickness. Optical recombination in the wetting layer is known to be indirect in k-space taking place between the X-point conduction band minimum and the top of the valence band at the Γ-point. The experimentally observed decay time is a sum of the radiative and non-radiative decay times

$$\frac{1}{\tau_{exp.}} = \frac{1}{\tau_{rad.}} + \frac{1}{\tau_{non-rad.}}. \tag{4.8}$$

Hence, the very short decay time of the WL emission is determined by non-radiative decay channels of carriers into the InP dots.

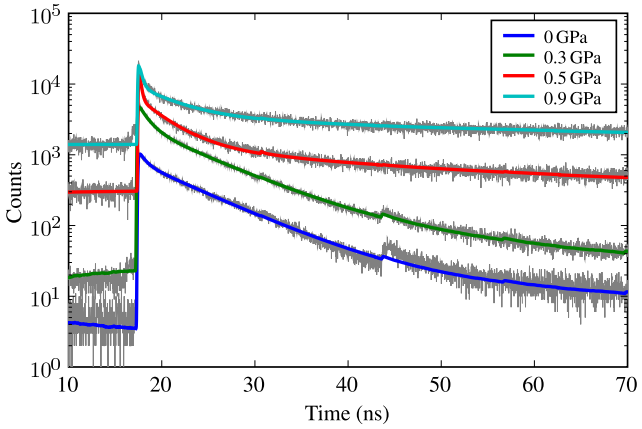

Figure 4.32: Pressure dependence of the PL decay of the QDs taken at low temperatures. Transients have been shifted by a constant offset for clarity.

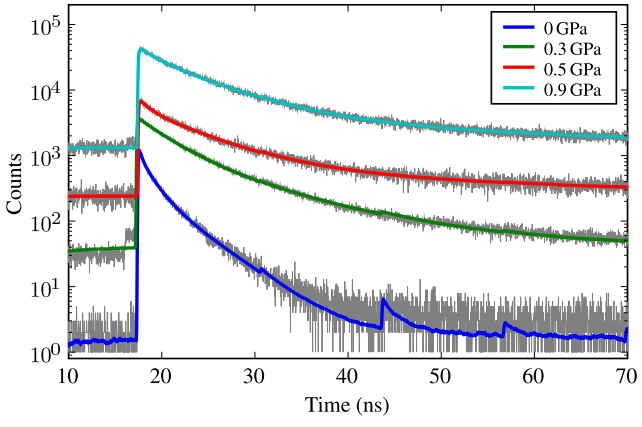

Figure 4.33: Pressure dependence of the PL decay of the WL taken at low temperatures. Transients have been shifted by a constant offset for clarity.

The dependence on hydrostatic pressure of the emission from the InP dots and the wetting layer is illustrated by the transients taken at 2 K for different pressures plotted in Figs. 4.32 and

4.33, respectively. For the QD luminescence the decay rates both of the direct $\Gamma - \Gamma$ and the indirect X-Γ optical transitions are within experimental uncertainty independent of pressure. By increasing the pressure beyond 0.5 GPa, however, the indirect-recombination component with the longer time constant of 30 ns dominates the PL decay, whereas the component of the direct recombination has disappeared. This is in nice agreement with the observation of the Γ-X crossover in cw experiments, presented in section 4.2.1, which occurs at around 0.2 GPa. The decay of the WL luminescence, on the contrary, exhibits a gradual slow down with increasing pressure, as clearly seen in the transients of Fig. 4.33. The application of a slight pressure of about 0.1 GPa causes the WL decay time at least to double and it increases further at higher pressures. This is an interesting effect which is taken as evidence of a less effective filling of the dots with increasing pressure and a confirmation of the fact that the filling of the quantum dots occurs from states in the WL.

Important information on the carrier dynamics in the InP/GaP QD system is obtained by comparing the dependence on pressure of the ratio of the PL peak intensities of the dots and wetting layer with that of the ratio between the weights of the indirect and direct components of the radiative recombination within the InP QDs, as shown in Fig. 4.34. One notices that along with the pronounced increase of the WL decay time, the intensity of the QD emission drops abruptly at extremely low pressure close to that of the Γ-X crossover in the dots. In contrast, for the QD emission the weight of the strength of the decay component from indirect transitions relative to that of the direct radiative decay channel increases monotonically with pressure. The latter suggests that the sharp drop in QD emission intensity, which might be related to the pressure-induced changes in the conduction band minima, seems to be connected to the extinction of a carrier relaxation channel for filling up the InP dots rather than with variation in oscillator strength for direct/indirect radiative recombination.

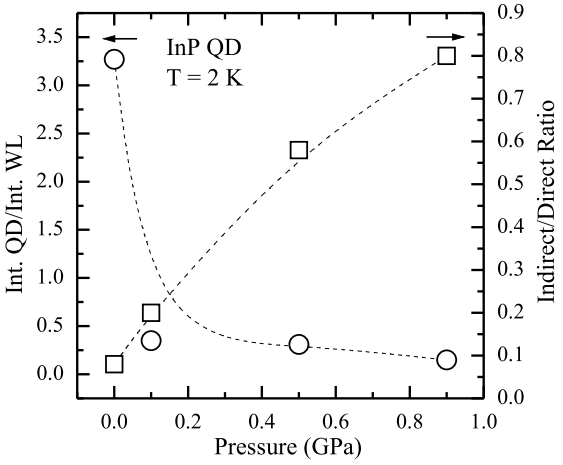

Figure 4.34: Pressure dependence of the intensity ratio between dot and wetting-layer emission (left) and of the ratio between the intensities of the indirect and direct decay components of the QD luminescence (right).

Further insight into the recombination dynamics is gained by studying the rise times of the QD luminescence signal as a function of pressure and temperature. Figure 4.35a) shows four rise transients of the dots PL measured at ambient pressure for different temperatures. As indicated in the figure, the rise times which are about two orders of magnitude shorter than the faster decay component, increase with temperature. This behavior which has been observed before [65], is

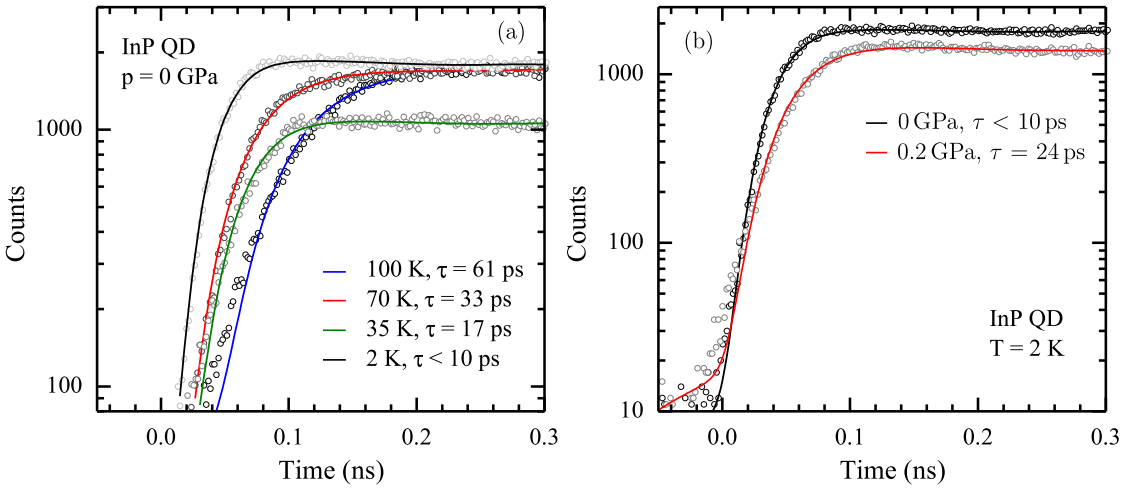

Figure 4.35: Rise times of the QD luminescence a) for different temperatures and b) at two different pressures. Solid lines are fits to the data with a single rising exponential function. Time constants are indicated.

a consequence of carrier-localization effects in the wetting layer. With increasing temperature a gradually increasing number of carriers localized by monolayer-width fluctuations in the InP WL will be able to escape and struggle to reach a quantum dot. Though, these thermally activated processes are slower, thus leading to longer effective rise times. Pressure has a similar effect on the rise time but for other reasons. In Fig. 4.35b) we compare two transients obtained at 2 K for 0 and 0.2 GPa. In this small pressure range, the rise time doubles (increases from less than 10 ps to 24 ps). Such slowing down of the carrier relaxation into the dots simply results from the variation of the relative energy position of the conduction band X minima in the wetting layer and the dots; difference which diminishes with pressure and vanishes at the type-I to type-II transition.

The pressure effects on the rise times are pronounced but not abrupt like the sudden drop in PL intensity of the QDs observed at very small pressures, as mentioned above. This points to a different origin for both effects. We give here a tentative explanation. For samples with such low QD densities as ours the carriers photoexcited in the GaP matrix can relax into the dots in two ways: either via a direct capture process or by falling first in the wetting layer before

being trapped in the QDs. The former mechanism seems to be very effective as long as the electron ground state of the InP dots corresponds to the Γ point. Electrons in the GaP barrier material reside in the X minima and due to the breakdown of translational invariance along the z direction - the growth direction of the InP/GaP heterostructure - there is a good coupling between the GaP X_z states and the Γ-point confined states of the InP dots. Above the Γ-X crossover the lowest conduction band state of the dots has X_{xy} character. The mixing of these states and the back-folded X_z ones from the GaP is negligible, leading to the switch off of one carrier capture channel into the dots and, hence, to the observed quenching of the QD emission at the crossover pressure.

4.2.4. Conclusion

The photoluminescence experiments under high pressure revealed that at ambient pressure the band alignment in the InP/GaP QD structure is of type-I and the QD emission is very intense arising from $\Gamma - \Gamma$ direct optical transitions between confined states of the dots. With increasing pressure this transition shifts up in energy at a typical rate of about 100 meV/GPa, such that at 0.2 GPa the absolute conduction-band minimum is at the X-point and the QD recombination has become indirect in reciprocal space. The X_{xy} levels of the InP dots are initially approximately 10 meV below the X-bound state of the wetting layer. With increasing pressure, however, the energy separation between them diminishes until at around 1.2 GPa they become degenerate and the quenching of the indirect QD emission is observed.

These finding are further confirmed by the results of time-resolved photoluminescence. At ambient pressure the transients corresponding to the main emission peak of the InP dots exhibit two monoexponential decay components with a time constant of 5 ns and 30 ns, which are associated with in k-space direct (Γ-Γ) and indirect (X-Γ) interband optical transitions, respectively. These decay times are within experimental uncertainty independent of pressure. What varies under pressure and pulsed excitation is the relative weight of the indirect recombination component against that of the direct one, as the Γ conduction band minimum of the dots shifts up in energy with increasing pressure with respect to their X_{xy} valleys. In contrast, the average decay time of the wetting layer luminescence increases from about 500 ps to nearly 1 ns in the pressure range up to 1 GPa. This fact and the observed pressure induced increase of the rise times of the QD emission are clear indication that the carrier transfer from the wetting layer into the dots becomes less effective as pressure increases. This is due to the combined effects of localization by monolayer-width fluctuations in the WL and the changes induced by the hydrostatic pressure in the relative position of the conduction band states of the dots and wetting layer.

5. Summary

In this work photoluminescence experiments under high hydrostatic pressure on self-assembled InAs/GaAs and InP/GaP quantum dots have been carried out. The particular growth conditions used for the fabrication of the InAs/GaAs sample lead to a multimodal distribution of the quantum dot sizes. This, in turn, gives rise to a characteristic emission profile, displaying up to nine clearly separable peaks attributed to the ground-state emission from each quantum dot subensemble of different size. In fact, structural analysis has shown that the quantum dots differ in size by entire monolayers. With increasing pressure all emission peaks shift to higher energies, which is typical for a direct Γ-Γ transition. The measured pressure coefficients for each subensemble, however, show a linear dependence on their zero pressure emission energy, which is directly related to the quantum dot size ranging from 65 meV/GPa for the largest dots to 110 meV/GPa for the smallest ones. This large variation has caused much confusion in the last years, as every experiment on similar samples yielded a different pressure coefficient. The particular sample studied here allows for the direct comparison of the pressure dependence of quantum dots of different size under exactly the same environmental conditions. In order to be able to assign the variation of pressure coefficients to a particular physical origin, pressure dependent strain field calculations using an atomistic valence-force field have been carried out. Using deformation potential theory it was found that the conduction band offset is also increasing at a rate of 46 meV/GPa. This implies that the pressure coefficient of the band gap of the embedded InAs is much smaller than that of bulk InAs. Considering the effects of quantum confinement within the envelope function approximation, such a behavior can be explained by the fact that states which are close to the bottom of the confining potential adopt the pressure dependence of the InAs band edge, whereas states which are close to the top of the potential follow the band gap of the barrier material. The calculated pressure coefficients as a function of the dot size are qualitatively in good agreement with the experimental findings considering the simplicity of the model, though the calculated variation of pressure coefficients is not as large as measured.

Further information about the electronic structure of the quantum dots is found by analyzing the energy at which the confined electron states cross the X-conduction band states of the barrier, which is identified by a sudden quenching of the emission intensity. In this way, it is possible to determine the valence band offsets for the heavy holes corresponding to different dot sizes.

By fitting these energies using the calculated confinement energies of the heavy holes, a valence band offset of 290 ± 10 meV for the strained InAs/GaAs quantum dot heterointerface was be obtained.

An open question concerning the electronic structure of InP quantum dots grown on GaP substrate was whether the observed emission has direct character in both real and reciprocal space. The large lattice mismatch of about 7.7 % is responsible for the shift of the Γ-point conduction band energy of InP close to the indirect band gap of GaP, which could possibly lead to a type-II confinement resulting in a poor luminescence intensity. I was able to show that the main emission peaked at 1.92 eV at ambient pressure is indeed due to a direct optical recombination processes in real and reciprocal space, unambiguously identified by an initial blue shift of the main emission with pressure. Besides for the QD emission, a weak luminescence band is observed which can be attributed to transitions involving bound states in the wetting layer, which exhibits a negative pressure coefficient typical for the indirect X-Γ gap. At low pressures of about 0.2 GPa, the crossover in the quantum dot with the X_{xy} state of InP occurs, leading to a sudden decrease of the luminescence intensity. This is confirmed by the long decay times of the QD emission obtained from time-resolved PL measurements. At ambient pressure the dominant decay component of 5 ns indicates a direct transition in reciprocal space, whereas above the Γ-X crossover the decay lengthens to about 30 ns, typical for an indirect transition. Further increase of pressure causes the emission peak to shift slowly to the red, as expected for an indirect X-Γ transition. finally, the QD emission quenches when the X_{xy} state in the dots crosses the X-level confined to the wetting layer at a pressure of about 1.2 GPa and the transition is becoming indirect in both reciprocal and real space. From the difference of the pressure coefficients of the quantum dots and wetting layer emission we can infer that at ambient pressure the X_{xy} states of InP are about 10 meV higher in energy than the Γ-point conduction band state.

The emission from the quantum dot bound states displays maximal intensity at a temperature of 70 K. This maximum, however, shifts to lower temperatures with increasing pressure. This behavior could be explained by setting up a system of rate equations representing the most important carrier transfer processes. Because of the low quantum dot density in the InP/GaP system, most of the photoexcited carriers reach the quantum dots through the wetting layer. At low temperatures the carriers localize due to monolayer-size fluctuations in the wetting layer, regaining mobility as the temperature rises. On the other hand, the rising temperature is promoting the thermal escape of the carriers from the quantum dots, leading to a decrease of the luminescence. With increasing pressure the confining potential of the quantum dots is decreasing and the temperature of maximal intensity is thus reducing. This carrier transfer model is further confirmed by the results of time-resolved photoluminescence, which demonstrate that the decay of

the wetting layer emission is governed by non-radiative processes at ambient pressure, which are continuously decreasing in weight as a consequence of the loss of the escape channel through the quantum dots induced by the rising pressure.

In summary, the surprising variation of the pressure coefficients observed in high pressure experiments on InAs/GaAs quantum dots samples, depending on the size of the quantum dots could be explained based on the results from pressure dependent strain-field calculations and by considering quantum confinement effects within a simple envelope function picture. Furthermore and in contrast to much more expensive full pseudopotential calculations, this approach unambiguously revealed the origin of this phenomenon being related to the interplay between strain and quantum confinement. On the other hand, it could be shown for the first time that quantum dots grown in the InP/GaP material system show luminescence which is due to direct transitions in real and reciprocal state, thus proving their relevance for applications as strong emitters for the visible red spectral range. From the present high-pressure experiments a clear picture for the electronic band structure of the InP/GaP system was obtained and explicitly used for the understanding of the peculiar carrier dynamics in such low-dimensional structures.

A. VFF calculations

The program which does the VFF calculations, written by the author, is using the *Python* language[83]. As *Python* is an interpreted language, it seems not to be suitable for doing large scale numerics. However, a package of subroutines for linear algebra, minimization, etc., called *SciPy*[84], which operate at C-level speed turns it into a versatile and simple, nevertheless powerful language for numerical calculations, like e.g. Matlab®. In addition, the possibility to write inline C-code for time critical parts, makes the speed of the resulting binaries comparable to that of pure C-programs.

The lattice structure is set up in a sparsely populated three-dimensional array, reflecting the positions of the atoms of a fcc-lattice, when represented in a cubic grid. The minimal cube that holds a unit cell of the zinc-blende therefor has a dimension of $8 \times 8 \times 8$, with group III atoms at indices [0,0,0], [0,2,2], [2,0,2], [2,2,0] and group IV atoms at [1,1,1], [1,3,3], [3,1,3], [3,3,1]. Like this, the next neighbour atoms are easily determined. A list of all first and second next neighbours for each atom is constructed once and stored, as we do not have to deal with changing bonds. The total strain energy is then calculated by looping over all atoms, evaluating eq. (3.56), which is implemented in inline C. Additionally, the first derivative of the total energy is calculated, which is needed by the minimizer. The minimizer (fmin_tnc, part of the *SciPy* package) uses a *truncated Newton* algorithm, which is a conjugate gradient method. After convergence the strain is calculated locally at the cation position from the distorted tetrahedron. The relaxation of a cubic supercell with a base length of 55 lattice constants, containig more

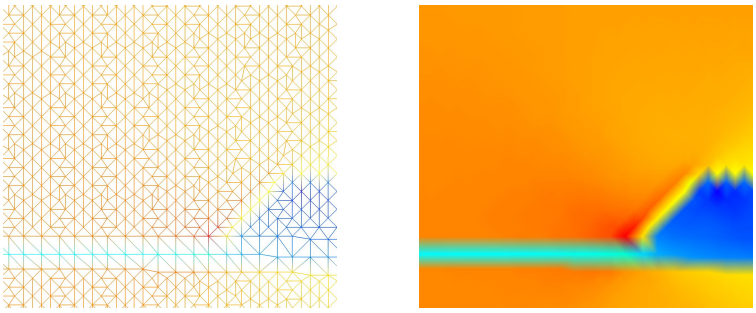

Figure A.1: Triangulation and interpolation of a crossectional layer of strain.

than 1.3 million atoms takes about 6 hours on an ordinary desktop PC at the time of this writing. The consecutive relaxation steps at each new pressure take only about 1 hour. The memory consumption for a supercell of that size is about 1.5 GB, fact which limits the maximal size of the structure more than the calculation time.

Due to the structure of the fcc-lattice, the atoms in a crosssectional $\{001\}$ (and equivalents) plane are located on a rectangular grid, which is rotated with respect to the coordinate system by 45°, rendering a matrix based visualization difficult. For that purpose the strain needs to be interpolated on a rectangular grid which is parallel to the coordinate axes. For that purpose the grid is divided into triangles by a method called Delaunay triangulation. Interpolated values can then easily be obtained in the surface of a triangle connecting three grid points (see figure A.1). This task is done by the MayaVi[85] software, which is a python wrapper around the *Visualization Tool Kit*[86]. The interpolation step is not only helpful for visualization purposes, it also allows for the extraction of smooth strain scans along a crystal direction, used in section 4.1.2 to calculate the strain modified bandstructure across the center of the quantum dot.

B. Expansion of the cubic bond-stretching potential

As pointed out earlier, the harmonic stretching potential of the standard VFF model was expanded by a cubic term. Its force constant was obtained by fitting the potential to the pressure dependence of the bulk modulus. Like this, the region of the potential, which corresponds to compression is well described. The tensile region however, cannot be chosen independently and thus lacks any physical meaning. As shown in figure B.1, the extrapolation of the potential for

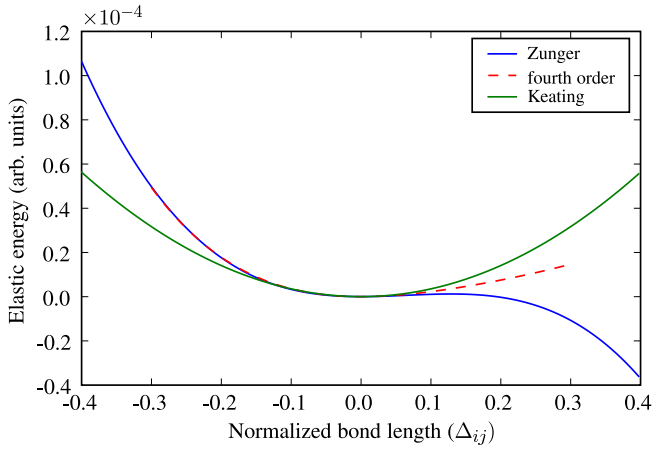

Figure B.1: Bond stretching potentials used in the VFF calculations. The cubic potential yields unphysical results for large tensile strains and has to be expanded by a fourth-order term.

the tensile region (> 0) is very bad, since it is very weak and, inivitably for a cubic polynomial, tends to $-\infty$. A fully strained, unrelaxed InAs/GaAs interface yields a deviation from the natural bond length of up to ± 0.3 in units of the normalized bond length, so that any minimzation will fail with this kind of potential. To circumvent that problem, I have expanded the potential by a fourth-order term while leaving the shape of the compressive half unaltered. To determine the fourth order coefficient, I have first fitted the compressive part up to the equilibirum position of the third order polynomial with a Morse potential

$$E(x) = a(1 - e^{-bx})^2, \tag{B.1}$$

which is an empirical intra moelcular potential often used in molecular dynamics, but which is, due to the exponential term, expensive to evaluate in terms of calculation time. Like this,

the tensile part of the potential is still not based on any physical property, but it is, incontrast to the third order polynomial, monotonically rising, approaching an upper limit at $+\infty$. This Morse potential is finally fitted by a fourth order polynominal, which is used in the minimization process. As mentioned in section 4.1.2, the minimizer ends up at a local minimum of the total strain energy more frequently, using the fourth order polynominal, than in the case of using a harmonic potential. The reason might be, that the minimizer is having problems to determine the step-length and direction in parameter space in the minimization process, when the derivative of the potential, i.e. the force, has a rather complex dependence on elongation. It turned out, that the minimization result is improved, if the energy is minimized a second time with an intermediate *shaking* of the structure, so that the atoms are randomly displaced from their relaxed position.

C. Useful information for pressure experiments

Wärmebehandlung für Gasket aus Inconel 718

Vorbereitung:

Gasket mit Isopropanol oder anderem Lösungsmittel fettfrei machen und in einer Quarzglasampulle oder Quarzglasschlenkgefäß unter ~~Vakuum~~ Argon verschließen. + Druckausgleich bei 885 °C in der Quarzampulle

Wärmebehandlung:

Von Raumtemperatur auf 885 °C in 12 Stunden aufheizen (Aufheizrate ca. 72 °C/h).
Bei 885 °C 24 Stunden halten.
Dann innerhalb 2 Stunden auf 700 °C abkühlen (Abkühlrate ca. 93 °C/h).
Bei 700 °C 20 Stunden halten.
Von 700 °C auf Raumtemperatur in ca 10 Stunden abkühlen (Abkühlrate ca. 63 °C/h).

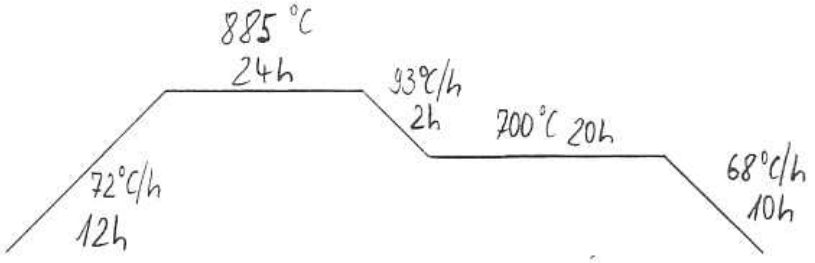

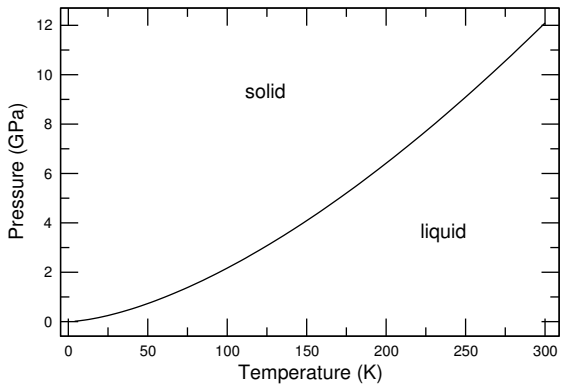

Figure C.1: Melting curve of ^{4}He after [87].

Bibliography

[1] P. H. Miller and J. H. Taylor. "Pressure coefficient of resistance in intrinsic semiconductors." Phys. Rev. **76**, 179 (149).

[2] W. Paul and D. M. Warschauer. *Solids under Pressure* (McGraw-Hill, New York, 1963).

[3] Landolt-Bornstein. *Numerical Data and Fucntional Relationships in Science and Technolgy*, volume 22 (Springer-Verlag, Berlin, 1987).

[4] S.-H. Wei and A. Zunger. "Predicted band-gap pressure coefficients of all diamond and zinc-blende semiconductors: Chemical trends." Phys. Rev. B **60**(8), 5404 (1999).

[5] A. W. Lawson and T.-Y. Tang. "A Diamond Bomb for Obtaining Powder Pictures at High Pressures." Rev. Sci. Instruments **21**, 815 (1975).

[6] W. A. Bassett, T. Takahashi and P. W. Stock. "X-Ray Diffraction and Optical Observations on Crystalline Solids up to 300 kbar." Rev. Sci. Instruments **38**, 37 (1966).

[7] R. A. Forman, G. J. Piermarini, J. D. Barnett and S. Block. "Pressure measurement made by the utilization of ruby sharp-line luminescence." Science **176**, 284 (1972).

[8] K. Syassen and W. B. Holzapfel. In K. D. Timmerhasu and M. S. Barber (editors) *Physics of Solids Under High Pressure*, volume 1, p. 223 (1979).

[9] H. K. Mao, J. Xu and P. M. Bell. "Calibration of the ruby pressure gauge to 800 kbar under quasi-hydrostatic conditions." J. Geophys. Res **91**, 4673 (1986).

[10] A. Jayaraman. "Diamond anvil cell and high-pressure physical investigations." Rev. Mod. Phys. **55**, 65 (1983).

[11] S. Sugano and Y. Tanabe. "Absorption Spectra of Cr^{3+} in Al_2O_3." Journal of the Physical Society of Japan **13**(8), 880 (1958).

[12] R. A. Noack and W. B. Holzapfel. "Calibration of the ruby pressure scale at low temperatures." In K. D. Timmerhaus and M. S. Barber (editors) *High Pressure Science and Technology*, p. 748 (Plenum Press, New York, 1979, 1979).

[13] G. J. Piermarini and S. Block. "Ultrahigh pressure diamond-anvil cell and several semiconductor phas transition pressures in relation to the fixed point pressure scale." Rev. Sci. Instruments **46**, 973 (1975).

[14] D. E. McCumber and M. D. Sturge. "Linewidth and Temperature Shift of the *R* Lines in Ruby." Journal of Applied Physics **34**(6), 1682 (1963).

[15] J. Yen and M. Nicol. "Temperature dependence of the ruby luminescence method for measuring high pressures." Journal of Applied Physics **72**(12), 5535 (1992).

[16] M. Grundmann, J. Christen, N. N. Ledentsov, J. Bohrer, D. Bimberg, S. S. Ruvimov, P. Werner, U. Gosele, J. Heydenreich, V. M. Ustinov, A. Y. Egorov, A. E. Zhukov, P. S. Kop'ev and Z. I. Alferov. "Ultranarrow Luminescence Lines from Single Quantum Dots." Phys. Rev. Lett. **74**, 4043 (1995).

[17] A. Forchel, R. Steffen, M. Michel, A. Pecher and T. L. Reinecke. "Etched single quantum dots - local probes of semiconductor properties." In D. J. Lockwood (editor) *Proc. 23nd Int. Conference on the Physics of Semiconductors (ICPS-23)* (World Scientific, Singapore, 1996).

[18] L. Goldstein, F. Glas, J. Y. Marzin, M. N. Charasse and G. L. Roux. "Growth by molecular beam epitaxy and characterization of InAs/GaAs strained-layer superlattices." Appl. Phys. Lett. **47**, 1099 (1985).

[19] K. Häusler, K. Eberl, F. Noll and A. Trampert. "Strong alignment of self-assembling InP quantum dots." Phys. Rev. B **54**, 4913 (1996).

[20] S. Fréchengues, V. Drouot, B. Lambert, D. Lemoine, S. Loualiche, A. L. Corre and H. L'Haridon. "Direct correlation of structural and optical properties of InAs self-assembled dots deposited on InP(100)." Appl. Phys. Lett. **71**, 2818 (1996).

[21] T. Utzmeier, P. A. P. J. Tamayo, R. Garcia and F. Briones. "Transition from self-organized InSb quantum-dots to quantum dashes." Appl. Phys. Lett. **69**, 2674 (1996).

[22] M. Sopanen, H. Lipsanen and J. Ahopelto. "Self-organized InP islands on (100) GaAs by metalorganic vapor phase epitaxy." Appl. Phys. Lett. **67**, 3768 (1995).

[23] A. Ponchet, A. L. Corre, H. L'Haridon, B. Lambert and S. Salaun. "Relationship between self-organization and size of InAs islands on InP(001) grown by gas-source molecular beam epitaxy." Appl. Phys. Lett. **67**, 1850 (1995).

[24] F. Hatami, N. N. Ledentsov, M. Grundmann, J. Böhrer, F. Heinrichsdorff, M. Beer, D. Bimberg, S. S. Ruvimov, P. Werner, U. Gösele, J. Heydenreich, U. Richter, S. V. Ivanov, B. Y. Meltser, P. S. Kop'ev and Z. I. Alferov. "Radiative recombination in type-II GaSb/GaAs quantum dots." Appl. Phys. Lett. **67**, 656 (1995).

[25] N. Carlsson, W. Seifert, A. Petersson, P. Castrillo, M. E. Pistol and L. Samuelson. "Study of the 2-dimensional 3-dimensional growth mode transition in metalorganic vapor-phase epitaxy of GaInP/InP quantum-sized structures." Appl. Phys. Lett. **65**, 3093 (1994).

[26] D. J. Eaglesham and M. Cerullo. "Dislocation-Free Stranski-Krastanow Growth of Ge on Si (100)." Phys. Rev. Lett. **64**(16), 1943 (1990).

[27] I. N. Stranski and L. Krastanow. "Zur Theorie der orientierten Ausscheidung von Ionenkristallen aufeinander." In *Sitzungsberichte der Akademie der Wissenschaften in Wien, Mathematisch-naturwissenschaftliche Klasse 146*, p. 797 (1937).

[28] V. A. Shchukin, N. N. Ledentsov, P. S. Kop'ev and D. Bimberg. "Spontaneous Ordering of Arrays of Coherent Strained Islands." Phys. Rev. Lett. **75**(16), 2968 (1995).

[29] F. Guffarth, R. Heitz, A. Schliwa, K. Pötschke and D. Bimberg. "Observation of monolayer-splitting for InAs/GaAs quantum dots." Physica E **21**, 326 (2004).

[30] F. Hatami, W. T. Masselink and L. Schrottke. "Radiative recombination from InP quantum dots on (100) GaP." Appl. Phys. Lett. **78**(15), 2163 (2001).

[31] I. Mukhametzhanov, R. Heitz, J. Zeng, P. Chen and A. Madhukara. "Independent manipulation of density and size of stress-driven self-assembled quantum dots." Appl. Phys. Lett. **73**(13), 1841 (1998).

[32] J. R. Chelikowsky and M. L. Cohen. "Nonlocal pseudopotential calculations for the electronic structure of eleven diamond andzinc-blende semiconductors." Phys. Rev. B **14**(2), 556 (1976).

[33] M. Cardona and F. H. Pollak. "Energy-Band Structure of Germanium and Silicon: The k·p Method." Phys. Rev. **999**(142), 530 (1966).

[34] E. O. Kane. "Band structure of indium antimonide." J. Phys. Chem. Solids **1**(4), 249 (1956).

[35] G. Bastard. *Wave mechanics applied to semiconductor heterostructures* (les éditions de physique, 1988).

[36] G. Dresselhaus, A. F. Kip and C. Kittel. "Cyclotron Resonance of Electrons and Holes in Silicon and Germanium Crystals." Phys. Rev. **98**(2), 368 (1955).

[37] A. R. Goñi, K. Syassen, Y. Zhang, K. Ploog, A. Cantarero and A. Cros. "Pressure dependence of the exciton absorption and the electronic subband structure of a $Ga_{0.47}In_{0.53}As/Al_{0.48}In_{0.52}As$ multiple-quantum-well system." Phys. Rev. B **45**, 6809 (1992).

[38] J. Bardeen and W. Shokley. "Deformation Potentials and Mobilities in Non-Polar Crystals." Phys. Rev. **80**(1), 72 (1950).

[39] G. L. Bir and G. E. Pikus. *Symmetry and Strain-Induced Effects in Semiconductors* (Wiley, New York, 1974).

[40] F. H. Pollak and M. Cardona. "Piezo-Electroreflectance in Ge, GaAs, and Si." Phys. Rev. **172**(3), 816 (1968).

[41] F. H. Pollack. "Effects of External Uniaxial Stress on the Optical Properties of Semiconductors and Simconductor Microstructures." In T. Suski and W. Paul (editors) *High Pressure in Semiconductor Physics II*, volume 54 of *Semiconductors and Semimetals* (Academic press, 1998).

[42] M. Chandrasekhar and F. H. Pollack. "Effects of uniaxial stress on the electroreflectance spectrum of Ge and GaAs." Phys. Rev. B **15**(4), 2127 (1977).

[43] C. Herring and E. Vogt. "Transport and Deformation-Potential Theory for Many-Valley Semiconductors with Anisotropic Scattering." Phys. Rev. **101**, 944 (1956).

[44] I. Balslev. "Influence of Uniaxial Stress on the Indirect Absorption Edge in Seilicon and Germanium." Phys. Rev. **143**(2), 143 (1966).

[45] A. R. Goñi and K. Syassen. "Optical Properties of Semiconductors under Pressure." In *Semiconductors and Semimetals*, volume 54 (Academic Press, 1998).

[46] E. Anastassakis and M. Cardona. "Phonons, Strain and Pressure in Semiconductors." In *Semiconductors and Semimetals*, volume 55 (Academic Press, 1998).

[47] M. Born and T. von Kármán. "Über Schwingungen in Raumgittern." Physik. Z. **13**, 297 (1912).

[48] P. N. Keating. "Effect of Invariance Requirements on the Elastic Strain Energy of Crystals with Application to the Diamond Structure." Phys. Rev. **145**, 637 (1966).

[49] R. M. Martin. "Elastic Properties of ZnS Structure Semiconductors." Phys. Rev. B **1**, 4005 (1970).

[50] J. M. Skipp and D. J. Dunstan. "Harmonic and anharmonic components of third-order elastic constants." Phys. Rev. B **69**, 054105 (2004).

[51] J. Groenen, C. Priester and R. Carles. "Strain distribution and optical phonons in InAs/InP self-assembled quantum dots." Phys. Rev. B **60**(23), 16013 (1999).

[52] C. Pryor, J. Kim, L. W. Wang, A. J. Williamson and A. Zunger. "Comparison of two methods for describing the strain profiles in quantum dots." Journal of Applied Physics **83**(5), 2548 (1998).

[53] R. Santoprete, B. Koiller, R. B. Capaz, P. Kratzer, Q. K. K. Liu and M. Scheffler. "Tight-binding study of the influence of the strain on the electronic properties of InAs/GaAs quantum dots." Phys. Rev. B **68**, 235311 (2003).

[54] F. D. Murnaghan. "The compressibility of media under extreme pressure." Proc. Natl. Acad. Sci. USA **30**, 244 (1944).

[55] A. J. Williamson, L. W. Wang and A. Zunger. "Theoretical interpretation of the experimental electronic structure of lens-shaped self-assembled InAs GaAs quantum dots." Phys. Rev. B **62**, 12963 (00).

[56] A. J. Williamson, A. Zunger and A. Canning. "Prediction of a strain-induced conduction-band minimum in embedded quantum dots." Phys. Rev. B **57**(8), R4253 (1988).

[57] I. E. Itskevich, S. G. Lyapin, I. A. Troyan, P. C. Klipsteinn, L. Eaves, P. C. Main and M. Henini. "Energy levels in self-assembled InAs/GaAs quantum dots above the pressure-induced G-X crossover." Phys. Rev. B **58**(8), R4250 (1998).

[58] B. S. Ma, X. D. Wang, F. H. Su, Z. L. Fang, K. Ding, Z. C. Niu, and G. H. Li. "Photoluminescence from self-assembled long-wavelength InAs/GaAs quantum dots under pressure." Journal of Applied Physics **95**, 933 (2004).

[59] M. D. Frogley, J. L. Sly and D. J. Dunstan. "Pressure dependence of the direct band gap in tetrahedral semiconductors." Phys. Rev. B **58**, 12579 (1998).

[60] J.-W. Luo, S.-S. Li, J.-B. Xia and L.-W. Wang. "Photoluminescence pressure coefficients of InAs/GaAs quantum dots." Phys. Rev. B **71**, 245315 (2005).

[61] O. L. Lazarenkova, P. von Allmen Seungwon Lee Fabiano Oyafuso and G. Klimeck. "The effect of the strain relaxation in InAs/GaAs stacked quantum dots and multiple quantum wells on the Raman spectrum." Ioffe Institut (2004).

[62] N. W. A. van Uden, J. R. Downes and D. J. Dunstan. "Photoluminescence of 111 InGaAs/GaAs strained-layer quantum wells under hydrostatic pressure." Phys. Rev. B **63**, 233304 (2001).

[63] M. D. Frogley, J. R. Downes and D. J. Dunstan. "Theory of the anomalously low band-gap pressure coefficients in strained-layer semiconductor alloys." Phys. Rev. B **62**(20), 13612 (2000).

[64] S. Adachi. "Material parameter of InGaAsP and related binaries." Journal of Applied Physics **53**(12), 8875 (1982).

[65] F. Hatami, W. T. Masselink, L. Schrottke, J. W. Tomm, V. Talalaev, C. Kristukat and A. R. Goñi. "InP quantum dots embedded in GaP: Optical properties and carrier dynamics." Phys. Rev. B **67**, 085306 (2003).

[66] F. Hatami, U. Muller, H. Kissel, K. Braune, R.-P. Blum, S. Rogaschewski, H. Niehus, H. Kirmse, W. Neumann, M. Schmidbauer, R. Kohler and W. T. Masselink. "Planar ordering of InP quantum dots on (100)In0.48Ga0.52P." J. Cryst. Growth **216**, 26 (2000).

[67] A. Kurtenbach, K. . Eberl and T. Shitara. "Nanoscale InP islands embedded in InGaP." Appl. Phys. Lett. **66**, 361 (1995).

[68] J. Ahopelto, A. A. Yamaguchi, K. Nishi, A. Usui and H. Sakaki. "Nanoscale InP Islands for Quantum Box Structures by Hydride Vapor Phase Epitaxy." Jpn. J. Appl. Phys **2**, L32 (1993).

[69] F. Hatami, G. Mussler, M. Schmidbauer, W. T. Masselink, L. Schrottke, H.-Y. Hao and H. T. Grahn. "Optical emission from ultrathin strained type-II InP/GaP quantum wells." Appl. Phys. Lett. **79**(18), 2886 (2001).

[70] G. H. Li, A. R. Goñi, C. Abraham, K. Syassen, P. V. Santos, A. Cantarero, O. Brandt and K. Ploog. "Photoluminescence from strained InAs monolayers in GaAs under pressure." Phys. Rev. B **50**(3), 1575 (1994).

[71] A. R. Goñi, K. Syassen, K. Strössner and E. Cardona. "Effect of pressure in the optical absorption of GaP and $Ga_xIn_{1-x}P$ (x=0.36 and 5)." Phys. Rev. B **39**(5), 3178 (1989).

[72] S. Ernst, A. R. Goñi, K. Syassen and M. Cardona. "Plasmon Raman scattering and photoluminescence of heavily doped n-type InP near the Γ-X crossover." Phys. Rev. B **53**(3), 1287 (1996).

[73] M. C. Muñoz and G. Armelles. "X-point deformation potentials of III-V semiconductors in a tight-binding approach." Phys. Rev. B **48**(4), 2839 (1993).

[74] A. F. Lin-Wang Wang and A. Zunger. "Million-Atom Pseudopotential Calculation of Γ-X Mixing in GaAs/AlAs Superlattices and Quantum Dots." Phys. Rev. Lett. **78**(14), 2819 (1997).

[75] G. H. Li, A. R. Goñi, K. Syassen, O. Brandt and K. Ploog. "State mixing in InAs/GaAs quantum dots at the pressure-induced Gamma -X crossing." Phys. Rev. B **50**, 18420 (1994).

[76] E. C. L. Ru, J. Fack and R. Murray. "Temperature and excitation dependence of the photoluminescence from annealed InAs/GaAs quantum dots." Phys. Rev. B **67**, 245318 (2003).

[77] J. Feldmann, G. Peter and E. O. Göbel. "Linewidth Dependence of Radiative Exciton Lifetimes in Quantum Wells." Phys. Rev. Lett. **59**(20), 2337 (1987).

[78] G. G. Tarasov, Y. I. Mazur, Z. Y. Zhuchenko, A. Maassdorf, D. Nickel, J. W. Tomm, H. Kissel, C. Walther and W. T. Masselink. "Carrier transfer in self-assembled coupled InAs/GaAs quantum dots." Journal of Applied Physics **88**, 7162 (2000).

[79] R. Heitz, A. Kalburge, Q. Xie, M. Grundmann, P. Chen, A. Hoffmann, A. Madhukar and D. Bimberg. "Excited states and energy relaxation in stacked InAs/GaAs quantum dots." Phys. Rev. B **57**, 9050 (1998).

[80] R. Heitz, M. Veit, N. N. Ledentsov, A. Hoffmann, D. Bimberg, V. M. Ustinov, P. S. Kop'ev and Z. I. Alferov. "Energy relaxation by multiphonon processes in InAs/GaAs quantum dots." Phys. Rev. B **56**, 10435 (1997).

[81] R. Heitz. *Nano-Optoelectronics, Concepts, Physics and Devices*, chapter Optical Properties of Self-Organized Quantum Dots (Springer, Berlin, 2002).

[82] H. Scher, M. F. Shlesinger and J. T. Bender. "Time-scale invariance in transport and relaxation." Physics Today **44** (1991).

[83] G. van Rossum. "Python tutorial." Technical Report CS-R9526, Centrum voor Wiskunde en Informatica (CWI), Amsterdam (1995).

[84] E. Jones, T. Oliphant, P. Peterson et al. "SciPy: Open source scientific tools for Python." (2001). URL `http://www.scipy.org/`.

[85] P. Ramachadaran. "MayaVi: A free tool for CFD data visualization." In *4th Annual CFD Symposium* (Aeronautical Society of India, Aug. 2001). URL `http://mayavi.sourceforge.net`.

[86] I. William Schroeder, 3rd Edition. Kitware. "The Visualization Toolkit." (2003). URL `http://www.vtk.org`.

[87] W. L. Vos, M. G. E. van Hinsberg and J. A. Schouten. "High-pressure triple point in helium: The melting line of helium up to 240 kbar." Phys. Rev. B **42**(10) (1990).

An dieser Stelle möchte ich mich bei allen Menschen bedanken, die auf die eine oder andere Weise zum Gelingen dieser Arbeit beigetragen haben. Bei Christian Thomsen für das Vertrauen und die wissenschaftliche Freiheit, die mir gewährte wurde, für das Interesse an meiner Arbeit und für die geteilte Begeisterung an Innovationen jeglicher Art. Bei Ale R. Goñi für die Einführung in die Hochdruckwelt, für die vielen lehrreichen und inspirierenden Diskussionen und gemeinsamen Konferenzreisen. Bei Thomas Möller für den Vorsitz in meiner Doktorpr üfung. Bei Harald Scheel, für die vielen Entdeckungen und Erfindungen die wir machten, als wir noch gemeinsam in der Hybridecke rumwerkelten. Bei Bernd Schöler, für das wachsende Vertrauen gegenüber meinen handwerklichen Fähigkeiten und für den Ausflug zu Ilse mit dem Luvre im Gepäck. Bei Marianne Heinold für die Unerschütterlichkeit gegenüber meiner bisweilen überkritischen Zeitplanung. Bei Heiner Perls für Hilfestellung jeglicher Art. Bei Sabine Bahrs, ob der motivierenden Wirkung ihres faszinierenden Endspurts und bei allen anderen, die mir in den letzten Jahren ans Herz gewachsen sind. Und bei Paula, für ihre erstaunliche Geduld und dass sie es am Ende geschafft hat mir doch noch eine überzeugende deadline zu setzen.

Arigato gozaimaaaaaashita.